Carnegie Mellon University
MELLON COLLEGE OF SCIENCE

THESIS

SUBMITTED IN PARTIAL FULFILLMENT OF THE REQUIREMENTS
FOR THE DEGREE OF

DOCTOR OF PHILOSOPHY IN THE FIELD OF PHYSICS

TITLE: "Two-dimensional materials: growth, characterization, and simulation."

PRESENTED BY: Jun Li

ACCEPTED BY THE DEPARTMENT OF PHYSICS

Randall Feenstra	1/4/18
RANDALL FEENSTRA, CHAIR PROFESSOR	DATE

Scott Dodelson	1/8/18
SCOTT DODELSON, DEPT HEAD	DATE

APPROVED BY THE COLLEGE COUNCIL

Rebecca Doerge	1/11/18
REBECCA DOERGE, DEAN	DATE

Two-dimensional Materials: Growth, Characterization, and Simulation

Doctoral Thesis

December 2017

Jun Li

Advisor

Prof. R. M. Feenstra

Department of Physics

Carnegie Mellon University, Pittsburgh, PA 15213

To my family and friends, for your unending inspiration and support.

Abstract

Since the discovery of graphene in 2004, there has been a great interest in two-dimensional (2D) materials from both the academic community and the semiconductor industry. In this work, we study various 2D materials and 2D heterostructures, aimed towards large-area device fabrication. Through detailed experimental work and extensive first-principle calculations, we determined the lowest energy structure for the interface of graphene formation on the C-face of SiC. The lowest energy structure contains > 1 monolayer of Si at the interface, forming an adatom-on-adlayer structure. Low-energy electron microscopy (LEEM) was employed to study properties of 2D heterostructures such as graphene–WSe_2 and graphene–MoS_2. Work function differences from the layers were extracted and band alignments were obtained, from which the nature of the contact at the interface was revealed. The electrical contact was found to be dependent on the constituent 2D layers of the heterostructures, as well as on the doping of the 2D layers. Finally, we consider simulation of devices made with 2D materials. We focus on interlayer tunneling field-effect transistors (TFETs) using 2D materials as the drain and source electrodes. By employing the first-principles density-functional-theory (DFT) wavefunctions, in the Bardeen tunneling formalism, we develop a "DFT-Bardeen" method that permits the computation of current-voltage characteristics in interlayer TFETs with reliable values for the magnitude of the currents. This method allows incorporation of differing materials into the source and drain electrodes, i.e. with different crystal structure, lattice constants, and/or band structure. Large variations in tunneling current were found, depending on the 2D materials being used. It is shown that the DFT-Bardeen method takes into account effects that are beyond simple lateral-momentum conservation, including the detailed symmetry and form of the wavefunctions. Predicted values for the tunneling current, including the subthreshold swing and the ON current, are compared with benchmark values for low-power digital applications.

Acknowledgements

First and foremost, I want to thank my parents for encouraging me to take on this journey. Without their selfless love and support all the way, I could not finish my PhD study.

I am greatly indebted to my thesis advisor, Randy Feenstra. Randy has been extremely patient and helpful in guiding me through this course of thesis research. Although being a word-renowned scientist, he is very approachable and always there when I need help. I have learned from him tremendously, knowledge not only about research, but also more generally about life. The more I know him, the more I admire his brilliance and determination. His exemplary work-ethic and care for other people will be a lifetime inspiration for me.

I also want to thank my group partners, for hands-on training on operating lab equipments as well as many insightful discussions. In particular, Guowei He showed me how to use the graphene growth and characterization system. Patrick Mende and Sergio de la Barrera taught me how to operate LEEM. Over years of working together with him, I benefited a lot from discussions with Sergio; and I am very grateful for his always amicable demeanor. I also thank Dacen Waters for voluntarily helping with fixing LEEM problems.

This journey would have been much less interesting and enjoyable had it not been for many of my friends I met here at Carnegie Mellon: Will McGinley, Sanxi Yao, Zach McDargh, Deva Gopalan, Hongyu Zhu, Xianglin Liu, to name a few. We often hang out together for dinner and play some board or video games after that. We shared our happiness as well as distress. I will always remember those good old days.

I would like to thank my outstanding thesis committee members, Mike Widom, Ben Hunt, and Brian D'Urso. Each of them has provided critical guidance and feedbacks over the years. Mike himself was heavily involved in a project presented in Chapter 3 of this thesis. Finally, I want to extend my thanks to many nice staff members in the Department of Physics. I thank Hilary Homer, Amanda Bodnar, Heather Corcoran for helping with paperwork issues and conference room scheduling; Al Brunk for helping with computer-related problems; and Chuck Gitzen for taking care of equipment orders.

Contents

Table of Figures

1 Introduction

Two-dimensional (2D) materials are defined as layered materials that consist of one (or a few) monolayers of atoms. Prior to the isolation of graphene, a single-layer of graphite, in 2004,[1] 2D materials were considered for a long time as a class of purely academic materials that could not exist in a freestanding, atomically thin form.[2,3,4] For example, Mermin argued that materials in two-dimensional form would be unstable in reality, due to thermal fluctuations that prevent long-range crystalline order at finite temperature.[4] Within this context, the first demonstration of a stable, freestanding 2D material, graphene, was a monumental discovery.

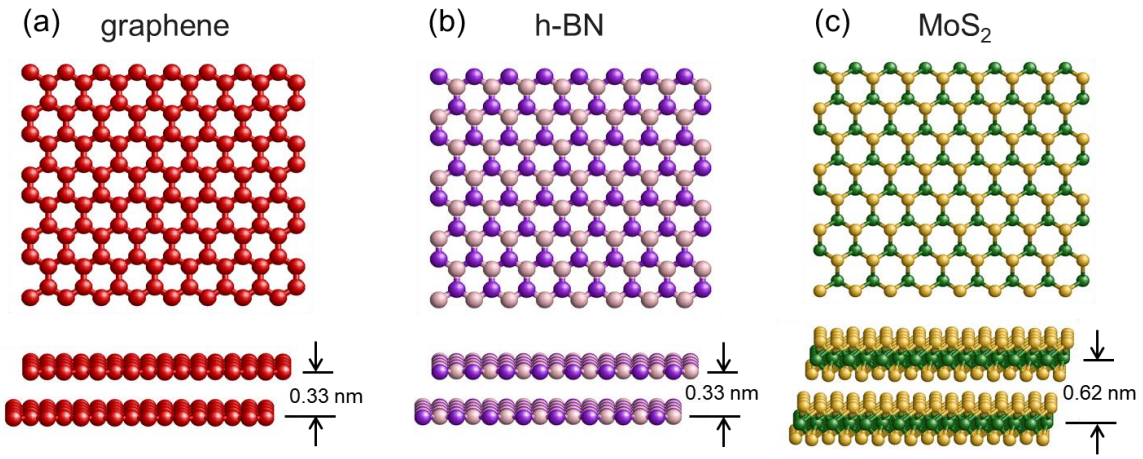

Figure 1.1 Representative 2D materials

Some representative 2D materials: (a) semi-metallic graphene; (b) insulating h-BN; (c) semi-conducting MoS_2. A 2D material is a material consists of one or a few such atomic monolayers. Generally these materials have a strong bonding in the plane but a weak (van der Waals) bonding between planes.

Since the discovery of graphene, many other 2D materials have been discovered and studied. Extensive research has been done to study the physical, chemical, and electrical properties of these materials. While graphene is semi-metallic, other 2D materials have been found to be insulating (e.g. hexagonal boron nitride, h-BN), or

semiconducting (e.g. molybdenum disulfide, MoS_2), or metallic (e.g. tungsten ditelluride, WTe_2), or superconducting (e.g. niobium diselenide, $NbSe_2$). Research efforts world-wide in 2D materials have been wide ranging, including topics such as (i) studying basic properties such as electron mobility, (ii) exploring novel quantum phenomena such as anomalous quantum Hall effect, (iii) isolating single or few layers from the bulk through mechanical exfoliation for researching their physics, (iv) synthesizing the 2D material directly on a desired substrate via various growth methods, for intended device application. While there are limitations in the properties that an individual 2D material can provide, combining various 2D materials into heterostructures, so called van der Waals heterostructures (Figure 1.2), offers a wealth of possibilities, leading to new physics and interesting phenomena, with potential device applications.[5]

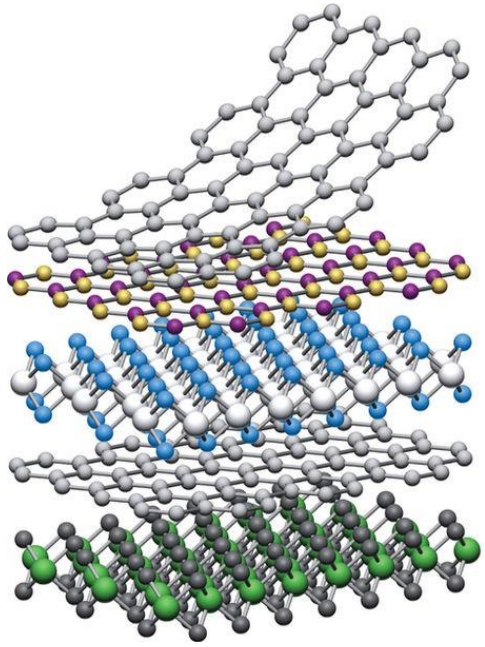

Figure 1.2 van der Waals heterostructures

Illustration of constructing a van der Waals heterostructure, using diverse 2D materials as building blocks. From Ref. 5.

In this thesis, I focus on growth and characterization of 2D materials and heterostructures. I also study performance, specifically tunneling characteristics, of devices based on these materials. The thesis consists of a mix of experimental work and

theoretical computations and simulations. This first Chapter provides a general introduction to representative 2D materials that are the theme of my research. Chapter 2 covers a few of the major experimental techniques that are routinely employed in our experiments. Chapter 3 studies graphene formation on the C-face of SiC, with new and significant experimental and theoretical results. Here I want to thank Prof. Mike Widom again for his immense work in this project. Prof. Widom did all the first-principles computations using the Vienna Ab initio Simulation Package (VASP) for results presented in Chapter 3 (and also including many more results not shown in this thesis). Chapter 4 presents a few examples of experimental studies of 2D materials and heterostructures using the methods covered in Chapter 2. The results there show that our measurements provide valuable information regarding crystallinity and interface properties of synthesized 2D materials, which is critical for device fabrication and application. Chapter 5 covers theoretical treatment and computations of tunneling characteristics in 2D heterostructures. There we discuss limitations in the past theoretical treatment of the problem and present our own approach to it. By direct comparison with experimental results, recent work demonstrates that our method provide a more reliable estimate of the magnitude of current in 2D tunneling devices. To this point, portions of the thesis have appeared in Refs. 6–13. , as noted in each relevant section.

1.1 Graphene

Graphene is the name given to one (or a few) monolayers of hexagonally-arranged carbon atoms, as pictured in Figure 1.3(a). A carbon atom has four valence electrons with a ground-state electronic shell configuration of $2s^2 2p^2$. When carbon atoms form solids, the total energy decreases due to overlap of the electron wavefunctions and formation of energy bands. In graphene, the 2s, $2p_x$, $2p_y$ orbitals of a C atom hybridize and form three sp^2 hybrid orbitals in a plane, each containing an unpaired electron. With these hybrids, each C atom forms energetically stable and localized σ–bonds with its three nearest-neighbor C atoms, in a honeycomb lattice. The remaining $2p_z$ orbital, which contains a single electron, then extends out of the plane. Overlapping $2p_z$ orbitals form the π band of electronic states, and the energy reduction associated with that band is then said to produce π-bonding in the material.

This overlap of $2p_z$ orbital states between neighboring C atoms plays a dominant role in the electronic properties of graphene near the Fermi energy. For this reason, the electronic band structure of graphene can be well described by the nearest-neighbors tight binding approximation.[14,15]

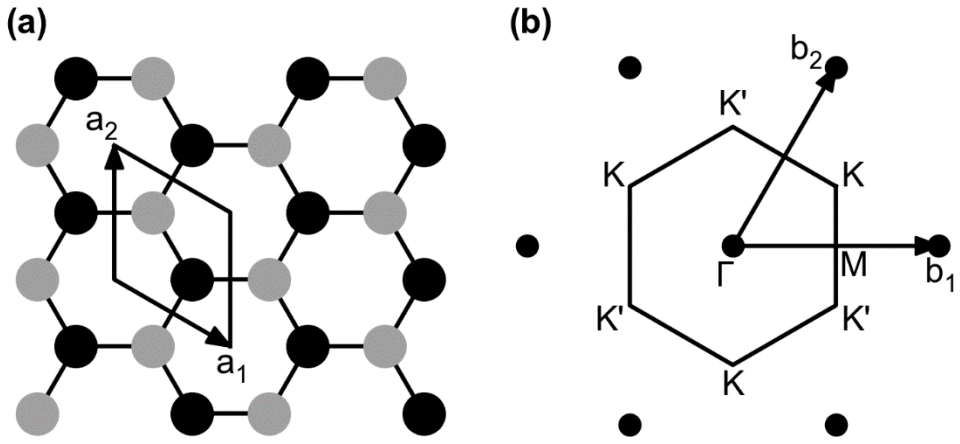

Figure 1.3 Graphene and its reciprocal lattice

(a) Atomic structure of a graphene monolayer viewed from the out-of-plane direction. Carbon atoms are represented by solid circles (black and gray). The unit cell of graphene is indicated, and it contains two carbon atoms, each belonging to a sublattice (black or gray). (a) Reciprocal lattice of graphene, showing the first Brillouin zone (BZ) and reciprocal basis vectors. High-symmetry points are labeled: center of the BZ by Γ, midpoint of the BZ edge by M, corner of the BZ by K (K'). Neighboring BZ corners, K and K', are not equivalent as they are *not* connected by a reciprocal lattice vector.

The unit cell of graphene contains two C atoms, as pictured in Figure 1.3(a). Each of them belongs to a separate triangular sublattice (black or gray). Figure 1.3(b) shows the reciprocal lattice and first Brillouin zone (BZ) of graphene. High-symmetry points of the BZ are labeled. Of particular importance is the six corners of the BZ (K or K'), also known as Dirac points. Electronic bands close to these points demonstrate a linear dispersion, as pictured in Figure 1.4(b).

Figure 1.4 shows the computed band structure of graphene using the tight binding approximation.[15] For any C atom, interactions with neighboring C atoms up to second-nearest neighbor are considered: the three nearest neighboring C atoms of a different

sublattice and the three second-nearest neighboring C atoms of the same lattice (see Figure 1.3). From the results shown in Figure 1.4 we see that the conduction and valence bands of graphene touch at the six Dirac points (and only at these points). Since the Fermi surface of graphene is composed of a finite set of six points on its BZ, graphene is usually termed a zero overlap semimetal, or a zero-gap semiconductor.[16]

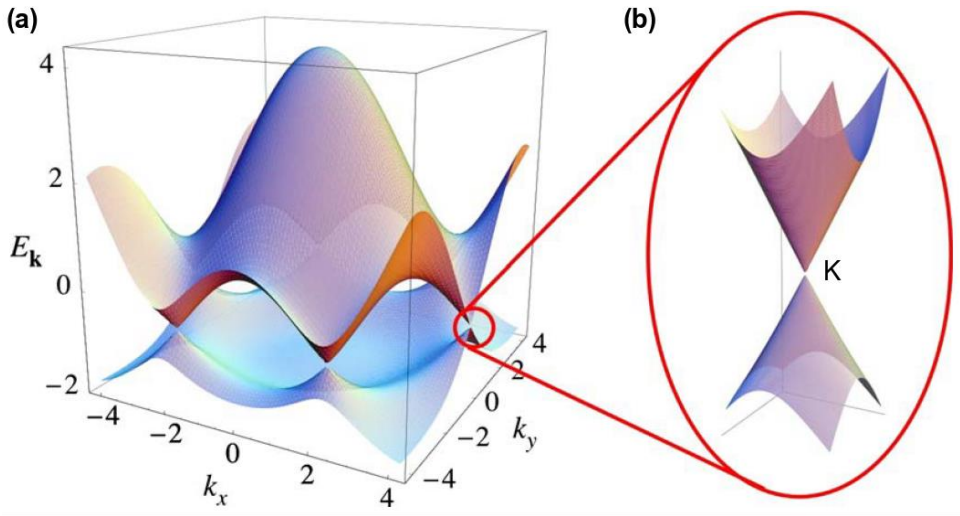

Figure 1.4 Band structure of graphene

(a) Band structure of monolayer graphene computed by the tight-binding method. The conduction and valence bands touch at the six corners of the first Brillouin zone (BZ), leading to semi-metallic behavior. (b) Zoom in of the energy bands close to a corner of the BZ (K or K'), demonstrating a linear dispersion relation. From Ref. 15.

The band structure close to the Dirac points (K and K') can be described by the Dirac-like Hamiltonian. For electronic bands close to K and K',

$$\begin{aligned} \widehat{H}_{\mathrm{K}}(\mathbf{q}) &= \hbar v_{\mathrm{F}} \begin{pmatrix} 0 & q_x - iq_y \\ q_x + iq_y & 0 \end{pmatrix} = \hbar v_{\mathrm{F}} \boldsymbol{\sigma} \cdot \mathbf{q}, \\ \widehat{H}_{\mathrm{K'}}(\mathbf{q}) &= \hbar v_{\mathrm{F}} \begin{pmatrix} 0 & q_x + iq_y \\ q_x - iq_y & 0 \end{pmatrix} = \hbar v_{\mathrm{F}} \boldsymbol{\sigma}^* \cdot \mathbf{q} \end{aligned} \tag{1}$$

where $\boldsymbol{\sigma} = (\sigma_x, \sigma_y)$ and $\boldsymbol{\sigma}^* = (\sigma_x, -\sigma_y)$ are the Pauli matrices, $\mathbf{q} = \mathbf{k} - \mathbf{K}$ is wavevector close to the Dirac points, and $v_{\mathrm{F}} \approx c/300$ (c is the speed of light) is the wavevector-independent Fermi velocity.

Solving the eigenvalue problem of (1) gives (for both K and K')

$$E = \pm \hbar v_{\mathrm{F}} q \,. \tag{2}$$

where $q = \|\mathbf{q}\| = \|\mathbf{k} - \mathbf{K}\|$.

A consequence of this linear dispersion is that the effective mass of the electrons is zero near the Fermi level ($E_{\mathbf{k}} = 0$ in Figure 1.4). From (2) we can deduce the density of state of graphene, $\rho(E)$:

$$\rho(E) = \left|\frac{dn}{dE}\right| = \frac{2|E|}{\pi(\hbar v_{\mathrm{F}})^2} \,, \tag{3}$$

a fact that will be used when we discuss the charge transfer in 2D heterostructures Section 4.2.

The linear spectrum (2) is not the only essential feature of the band structure near the Dirac points. The Dirac-like Hamiltonian (1) suggests that, by analogy with quantum electrodynamics (QED), we can introduce a quantity called chirality that is a projection of the pseudospin **σ** on the direction of wavevector **q** and is positive (negative) for electrons (holes).[17] This chirality means an electron hopping from K to K' is not allowed since the pseudospin is not conserved. This conservation rule explains many electronic processes observed in graphene such as the ballistic transport.[18]

1.2 Hexagonal Boron Nitride

Hexagonal boron nitride (h-BN) is one of the three crystalline forms of boron nitride. Due to strong, in-plane covalent bonds and weak van der Waals interlayer interactions, h-BN is a layered material, similar to graphite, and highly stable in thickness down to a single layer. Monolayer h-BN has the same hexagonal lattice structure as graphene (Figure 1.1), but with two atoms of different species (boron and nitrogen) in a unit cell. Unlike the semi-metallic graphene, h-BN is a wide-band-gap insulator, with a band gap energy near 6 eV.

H-BN has been used as a substrate to other 2D materials, due to its atomically smooth surface that is free of dangling bonds and charge traps.[19] STM studies of

graphene supported on h-BN show electron-hole fluctuations are significantly reduced compared to graphene supported by more conventional substrate silicon oxide.[20] Due to its flatness and inertness, h-BN has also been used as an encapsulation layer for either improving electronic properties of the encapsulated material or protecting other less-stable 2D materials. In the scope of this analysis, h-BN will be primarily viewed as a convenient insulating material. Specifically, we consider h-BN as tunneling barrier for devices made of 2D heterostructures, a point that will be discussed in Chapter 5.

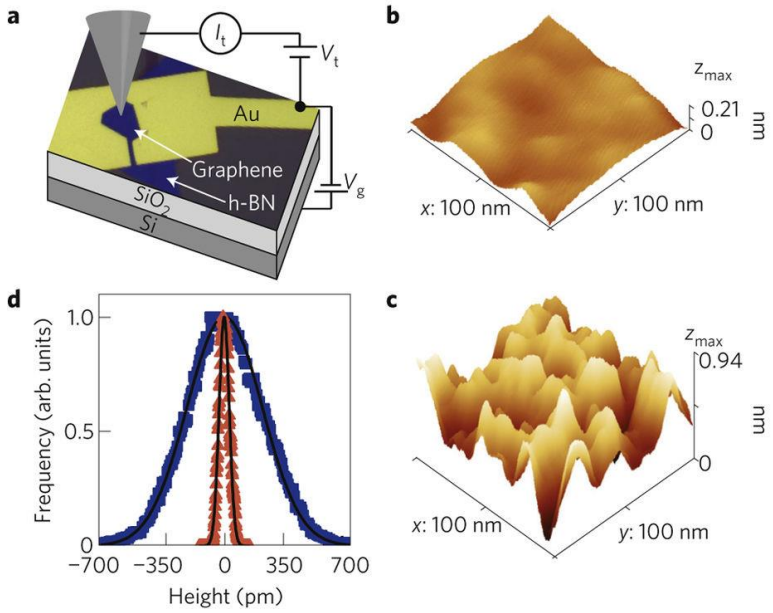

Figure 1.5 Using h-BN as atomically smooth substrate

An example of using h-BN as atomically smooth substrate. (a) Schematic of a device that has exfoliated monolayer graphene on an h-BN substrate, with gold electrodes as contacts. The wiring of the STM tip is indicated. (b) STM topographic image of monolayer graphene on h-BN showing surface corrugations. (c) STM image of monolayer graphene on SiO_2 showing significantly increased corrugations. (d) Histograms of the height distributions for graphene on SiO_2 (blue) and graphene on h-BN (red) along with Gaussian fits. From Ref. 20.

1.3 Transition Metal Dichalcogenides

Transition metal dichalcogenides (TMDs) are a family of materials of type MX_2, where M is a transition metal element (Mo, W, Zr, Nb, etc.) and X is a chalcogen (S, Se, or Te). Similar to graphene and h-BN, TMD is a layered material with strong in-plane bonding and weak (van der Waals) out-of-plane interactions. A TMD monolayer has a sandwich-like structure (see Figure 1.1(c)), with the chalcogen atoms in two hexagonal planes separated by a plane of transition metal atoms. Although TMDs have been studied for decades, there is at present a resurgence of scientific and engineering interest in their atomic thin 2D forms because of recent advances in sample preparation, optical detection, transfer and manipulation of 2D materials, and physical understanding of 2D materials learned from graphene.[21]

TMDs show a wide range of electronic, optical, mechanical, and thermal properties, partly due to the multiple options of transition metal atoms and chalcogen atoms for composition. For example, MoS_2 and WSe_2 are semiconducting, while NbS_2 and $TaSe_2$ are metallic, and $NbSe_2$ and TaS_2 have demonstrated superconducting behavior. What is more interesting is that many semiconducting TMDs show band gaps that are dependent on the number of atomic layers the TMDs consist of. For instance, the bulk MoS_2 has an indirect band gap of 1.3 eV.[22] As the MoS_2 crystal become atomically thin, its band gap energy increases.[23] In its single-layer form, the MoS_2 has a *direct* band gap of 1.9 eV.[24] The direct band gap results in photoluminescence from monolayer MoS_2, opening the possibility of optoelectronic applications.

The sizeable band gap of semiconducting TMDs with band gap energy in the range of 1 – 2 eV makes them particularly appealing for device applications. Extensive research efforts have been undergoing to utilize these atomically thin semiconductors to make high performance, low power field effect transistors (FETs). For FETs, desirable properties include high carrier mobilities for fast operation, a high on/off ratio for effective switching, high on-state current for high performance, and low off-state current for low power consumption.[21] While graphene has demonstrated exceptionally high carrier mobilities, the lack of band gap means it cannot achieve a low off-state current. In comparison, the 1 – 2 eV band gap in TMD monolayers can result in high on/off ratios.

Compared with classical 3D electronic materials, the extreme thinness of these 2D semiconductors allows more efficient control over switching[25] and can help to reduce short-channel effects and power dissipation, the main limiting factor of current transistors.[26]

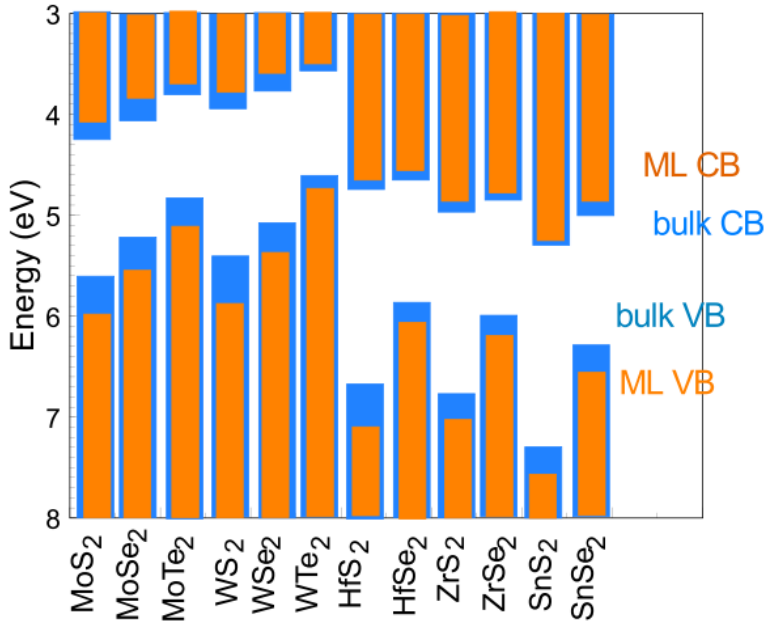

Figure 1.6 Band gaps of various TMDs

Band alignment diagram of TMDs in bulk form and monolayer (ML) form, showing conduction band (CB) and valence band (VB) of each material. The energy gap between the CB and the VB is the band gap of each material. From Ref. 27.

1.4 Tunneling field-effect transistors

A very appealing perspective of 2D materials is to use them to make high speed, low power tunneling field-effect transistors (TFETs).[6,28–33,126–138] TFET devices can switch between "ON" and "OFF" states by modulation of a current that tunnels through a barrier.[30] This is fundamentally different from metal-oxide-semiconductor field-effect transistors (MOSFETs), which switch by modulating thermionic injection of electrons over a barrier.[34,35] As a result, TEFTs are not limited by the thermal Maxwell-Boltzmann tail of carriers, which limits MOSFET current subthreshold swing to about 60 mV/decade

at room temperature.[36] The subthreshold swing (SS) is defined as the inverse of subthreshold slope, and is a measure of the steepness of the turn on slope in the drain current (I_D) versus gate voltage (V_G) characteristics,

$$SS = \left| \frac{d V_G}{d (\log_{10} I_D)} \right| \tag{4}$$

i.e. the gate voltage required to change the drain current by one order of magnitude when the transistor is operated in the subthreshold region (Figure 1.7(c)).

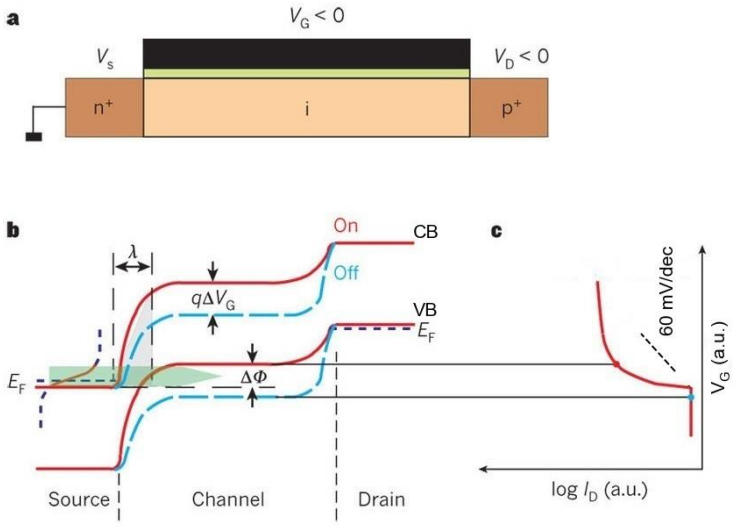

Figure 1.7 Principle of operation of a conventional TFET

(a) Schematic cross-section of p-type TFET with applied source (V_S), gate (V_G) and drain (V_D) voltages. (b) Energy band profile for the ON state (red lines) and the OFF state (dashed blue lines) of the TFET. In the OFF state, the conduction band (CB) of source is aligned with the band gap of the channel and no empty states are available for the electrons to tunnel to, so the current is very low. In the ON state, the valence band (VB) of the channel is moved above the CB of the source through applied V_G so that band-to-band tunneling can occur. The grey triangular shade approximates the tunneling barrier. (c) Schematic of the drain current – gate voltage characteristics on a logarithmic scale. The black dashed line denotes a subthreshold swing (SS) of 60 mV/decade. Adapted from Ref. 29.

For TFETs, SS can be much lower than 60 mV/decade since tunnel current flows only once the valence band edge of one electrode rises above conduction band edge of

the other (band-to-band tunneling). The low SS (i.e. sharp turn-on) allows TFETs to be operated at reduced voltages, hence yielding digital devices that require relatively low amounts of energy to switch between ON and OFF states. Although there have been many TFETs fabricated in different material systems, none has been adopted for mainstream applications.[29,30] The major challenge is to obtain a sufficiently large ON current while maintaining a low SS.

More recently, the interest in the TFETs has intensified due to the development of 2D materials.[8,126–138] Compared to usual three-dimensional (3D) materials, 2D materials offer more possibilities due to their unique properties. For example, instead of using the conventional TFET design as in Figure 1.7(a), we can stack atomically thin 2D layers to form a vertical tunneling device,[8,126,127] as shown in Figure 1.8.

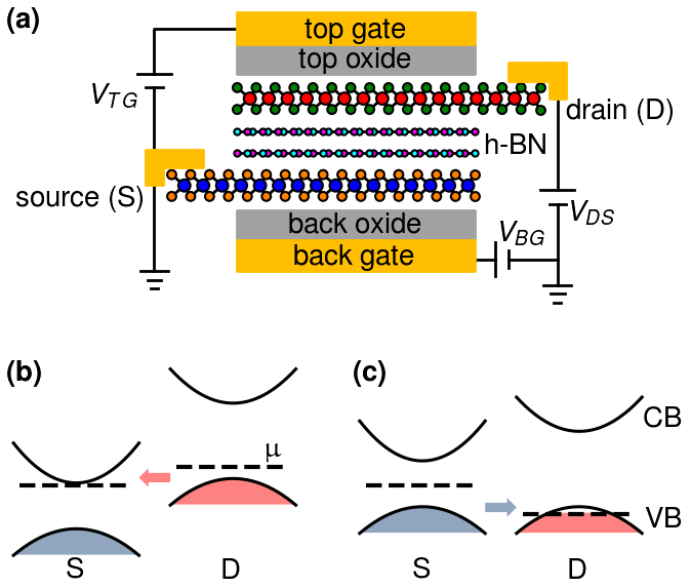

Figure 1.8 Interlayer TFET made with 2D heterostructure

Schematic of a 2D interlayer TFET and its operation modes. (a) Schematic cross-section of 2D interlayer TFET. Source and drain electrodes are TMD monolayers, with zero, one, or few layers of h-BN as tunneling barrier. (b) Tunneling between *unlike bands*, similar to the band-to-band tunneling in 3D TFETs in Figure 1.7: electrons tunnel between valence band (VB) of one electrode and conduction band (CB) of the other. (c) Tunneling between *like bands*; electrons tunnel between VB of one electrode and VB of the other, or between CB of one electrode and CB of the other.

The 2D interlayer TFET in Figure 1.8(a) has two operation modes: electrons tunneling between valence band (VB) of one electrode and conduction band (CB) of the other (unlike-band tunneling); electrons tunneling between VB of one electrode and VB of the other, or CB of one electrode and CB of the other (like-band tunneling). The unlike-band tunneling is similar to the band-to-band tunneling in conventional 3D TFETs, giving rise to a steep turn on (low SS) when the VB edge of one electrode rises above the CB edge of the other. However, instead of tunneling across the bandgap of a semiconductor depletion region (Figure 1.7(b) shaded area), electrons in 2D interlayer TFETs tunnel across a thin insulating layer. The depletion region in 3D TEFT is characterized by the screen tunneling length λ which is typically a few nanometers thick, and requires substantial doping and/or electrical gating.[30] In contrast, due to weak out-of-plane interactions, the tunneling barrier in 2D interlayer TFET can be made sub-nanometer thin, by using one or zero (also known as a vdW gap in this case) layer of h-BN.[6,126,127] This is important because the magnitude of tunneling current depends strongly on the barrier thickness and potentially large ON current may be achieved with 2D interlayer TFET. Additionally, the doping requirement can be avoided or relaxed by choosing the appropriate 2D materials for the device.[6,126,127]

In addition to the steep turn-on in the unlike-band tunneling mode, another intriguing property of 2D tunneling device is the *resonant tunneling* in the like-band tunneling mode,[132–138] as shown in Figure 1.9. The resonant tunneling behavior has been observed for graphene-hBN-graphene tunneling devices.[133,136] This phenomenon can be explained by the lateral momentum (or wavevector) conservation. For 2D materials, the eigenstates are confined to the 2D plane, causing them to have well-defined momentum in the lateral directions, but decaying character in the out-of-plane direction. At some particular applied voltage, the source and drain 2D layers have their VBs (and/or CBs) in complete alignment with each other in the momentum space (Figure 1.9, band alignment corresponding the peak current), and resonant tunneling occurs.[132] At other voltages, either there are no empty states for electrons to tunnel to, or the tunneling is constrained by the lateral wavevector conservation, leading to reduced currents.

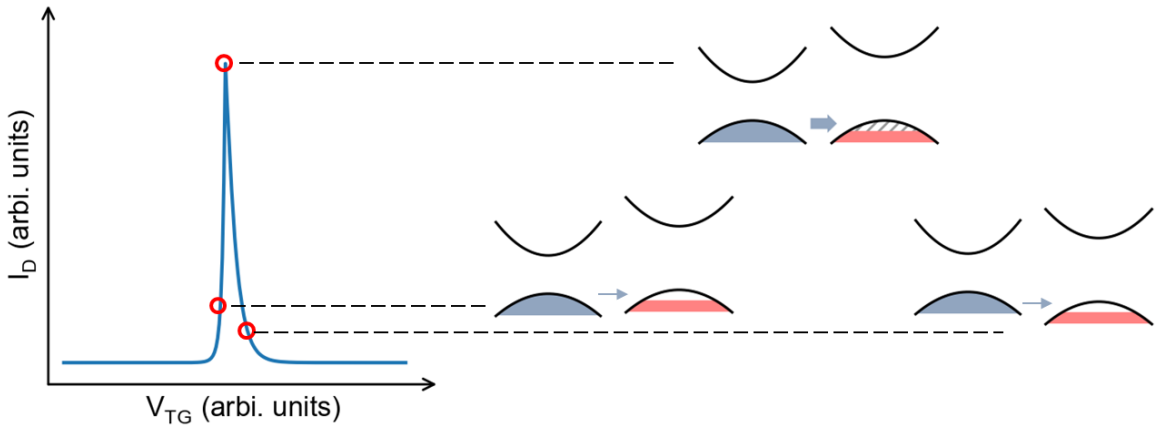

Figure 1.9 Resonant tunneling and lateral momentum conservation

Resonant tunneling in like-band tunneling mode of 2D interlayer TFET. Left: schematic of drain current – gate voltage characteristics, showing the resonant tunneling peak. Right: band alignment in the momentum space, horizontal axis is the lateral wavevector and vertical axis is the energy. The band alignments for selected points on the current characteristics show resonant tunneling (both energy and lateral wavevector are aligned, so a large current occurs) and off-resonant tunneling (unequal lateral wavevectors, resulting in a small current).

1.5 Theme

To this point, I have briefly described the 2D materials that are the main topic of my research. Although my work has focused on different aspects (growth, characterization, and simulation) of various 2D materials (e.g. graphene, TMDs), the studies all serve one goal — *scalable* device fabrication (for tunneling devices in particular), meaning that our emphasis is on materials prepared over large areas by epitaxial deposition.

Many of the 2D materials discussed above can be and have been produced through mechanical exfoliation, inspired by the first isolation of graphene.[1] While many interesting properties and phenomena have been discovered through studying such exfoliated materials, producing 2D materials via exfoliation is not suitable for device application due to major issues such as scalability and reproducibility.[18] For this reason, we focus our studies on epitaxially grown 2D materials. For example, in Chapter 3, we study the interface structure of graphene formation on silicon carbide (SiC) in order to

better improve the quality (e.g. grain size and uniformity) of grown graphene on the surface.[7] This direct formation graphene on SiC has the additional advantage of being directly compatible with established scalable device fabrication techniques as SiC is a monocrystalline semiconducting substrate (which can be produced with high resistivity, i.e. semi-insulating).[37,38] In Chapter 4, we characterize epitaxially grown 2D materials and 2D heterostructures with our experimental tools, obtaining information such as work function differences and band alignments that are critical for device design.[9,10,11]

Finally, in Chapter 5 we study tunneling characteristics in devices made with 2D materials. We focus on 2D interlayers TFETs introduced in the previous section. The primary motivation for this work is the large discrepancy between the previous simulated current magnitudes and the experimental results.[133,135,138] Since a major challenge of using TFETs for mainstream application is to obtain sufficiently high ON current,[29,30] a reliable estimate of the current magnitude is important in deciding what materials and electrostatic parameters may be used for fabricating the device. By employing wavefunctions obtained by first-principles density-functional-theory (DFT), in the Bardeen tunneling formalism, we develop a "DFT-Bardeen" method that permits computation of current-voltage characteristics in interlayer TFETs with reliable values for the magnitude of the current.[6] This method has been shown to include effects that are beyond those included in the previous simulation, and hence produce current magnitudes that are in much better agreement with the experiment.[8] Tunneling currents for interlayer TFETs made from various 2D materials are computed using this method.[6] The results should be useful in choosing appropriate materials from which to fabricate device.

2 Experimental Methods

2.1 Graphene Preparation and Characterization

We prepare epitaxial graphene by annealing SiC at high temperatures (>1000 ℃) under different environments, such as vacuum, 1 atm argon, 1 atom neon, or 5×10^{-5} Torr of disilane. Graphene samples are produced in a custom-built ultra-high-vacuum (UHV) system. Figure 2.1 shows a picture of the system. It consists of two parts: a preparation chamber on the right that is used for annealing SiC samples to form graphene; and a connected, low-energy electron diffraction (LEED) characterization chamber on the left. There is a valve between the preparation chamber and the LEED chamber. The valve is open when transferring a sample between the two chambers (using transfer rods) and closed otherwise. The preparation chamber is pumped by a scroll pump, two levels of turbomolecular pumps and has a base pressure of 1×10^{-9} Torr. The LEED chamber is pumped by a scroll pump, two levels of turbomolecular pumps, and an ion pump, and is normally kept at a pressure of 1×10^{-10} Torr.

The major advantage of this system is that is allows *in-situ* LEED measurements. With this capability, we can study surface reconstructions at every stage of graphitization. Each time we do an annealing of a sample in the preparation chamber, we transfer it to the LEED chamber to perform LEED measurements, and then transport it back for further annealing if desired. Since all the steps are carried out inside the vacuum system, contamination from air is avoided. Another advantage of the system is that, since the preparation chamber is a double walled chamber, we can flow liquid N_2 between the walls to cryogenically purify inert gas such neon filled into the chamber. This system has been extensively used in our group by past and current students (including the author, JL). All the LEED results presented in this thesis, most of them in Chapter 3, were obtained using this system.

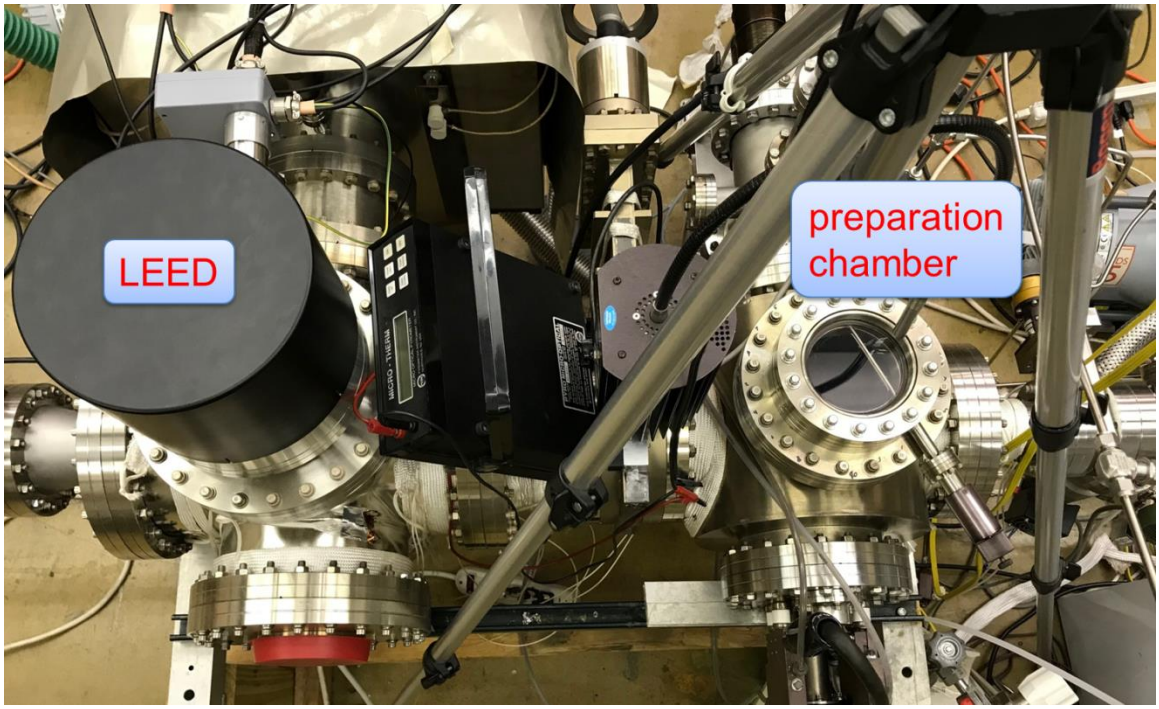

Figure 2.1 Graphene formation system

Photograph of graphene preparation and LEED measurement system.

Annealing of samples is accomplished by using a bow-tie shaped graphite strip heater, as pictured in Figure 2.2. The sample is placed in the center of the graphite heater by a dedicated XYZ-manipulator. No measurable contamination of the sample surface from the heater is found when annealing SiC to form graphene. The strip heater is mounted on two large copper clamps and two thick water-cooled copper feedthroughs are used to transmit current. The current is supplied by a transformer that at it maximum can generate a current of about 270 A. This allows a sample to be annealed at temperatures up to 1900 ℃.

Most of our experiments are performed using nominally on-axis 6H SiC or 4H SiC wafers, with no apparent differences between results for the two types of wafers. The wafers are polished on either the (0001) surface or the $(000\bar{1})$ surface. After receiving the wafers from a supplier, they are cut into 1×1 cm^2 pieces that we normally work with. To prepare graphene, we first etch the sample surface by annealing in hydrogen or disilane to remove polishing damage. Hydrogen etching is performed by flowing 99.9995% pure hydrogen in the preparation chamber at a rate of 105 lpm and heating the sample at

1600 ℃ for 3 min.[39] Etching by disilane is performed by heating the sample in 5×10^{-5} Torr disilane at 850 ℃ for 5 min. The disilane is flowed into the preparation chamber through a leak-valve that can be used to accurately control the pressure of disilane in the chamber. The sample is then annealed either in vacuum or in 1 atm argon or in 5×10^{-5} Torr disilane to form graphene. The temperature of the sample during the annealing is monitored by a disappearing filament pyrometer. We note that for making graphene in vacuum, the preparation chamber is constantly being pumped during annealing. This is also true for preparing graphene in the disilane environment, except that we control the supply of disilane through the leak-valve to maintain a pressure of 5×10^{-5} Torr in the chamber. For graphitization in argon, we first close all the valves connected to the preparation chamber to isolate the chamber, immediately after which we fill the chamber with argon. When the pressure of argon in the chamber is slightly higher than 1 atm, we open a vent valve and keep the flow rate of argon at 45 lpm by adjusting the regulator on argon gas cylinder. The sample is then annealed to form graphene. It is clear that during this process the preparation chamber is not being pumped.

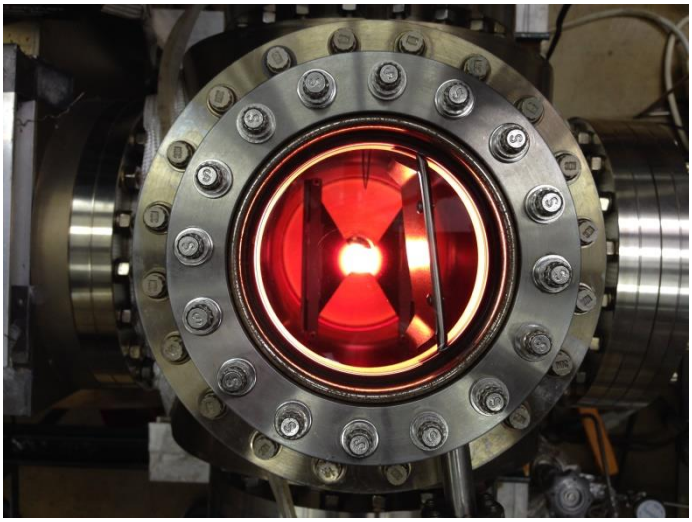

Figure 2.2 Bow-tie shaped graphite strip heater

Top view of preparation chamber. A bow-tie shaped strip heater is fixed in the middle of the chamber. The sample is placed on the center of the heater.

2.2 Low-energy Electron Diffraction

Low-energy electron diffraction (LEED) is a technique to study symmetry and structure of the surface of a crystalline sample or thin film.[40] In LEED measurements, a beam of low-energy electrons in the range of 20 eV – 500 eV is incident on the sample surface. The elastically backscattered electrons give rise to diffraction spots on a fluorescent screen.

Figure 2.3 is a diagram of a LEED apparatus. In the electron gun, monochromatic electrons are emitted by a cathode filament (e.g. LaB6 crystal) which is at a negative potential, typically 100 – 600 V. After leaving the filament, the electrons are accelerated by the large voltage difference between the filament and the screen which is typically held at a voltage between 5 and 6 kV. During this process, the electrons then are focused into a beam of about 0.2 – 0.5 mm wide, by a series of electrodes serving as electron lens. After interacting with the first few layers of atoms on the surface, the electrons are diffracted, both elastically and inelastically. Some energy-filtering grids are placed in front of the phosphor screen to screen out the inelastically scattered electrons. The elastically backscattered electrons are accelerated and hit the phosphor screen which emits photons that can be detected by a camera.

The LEED measurements are performed in ultra-high vacuum (UHV) to keep the sample surface clean. To be able to observe distinguishable spots in the diffraction pattern, sufficient structural order must exist on the surface. This typically requires a region of single crystal surface as wide as the electron beam.

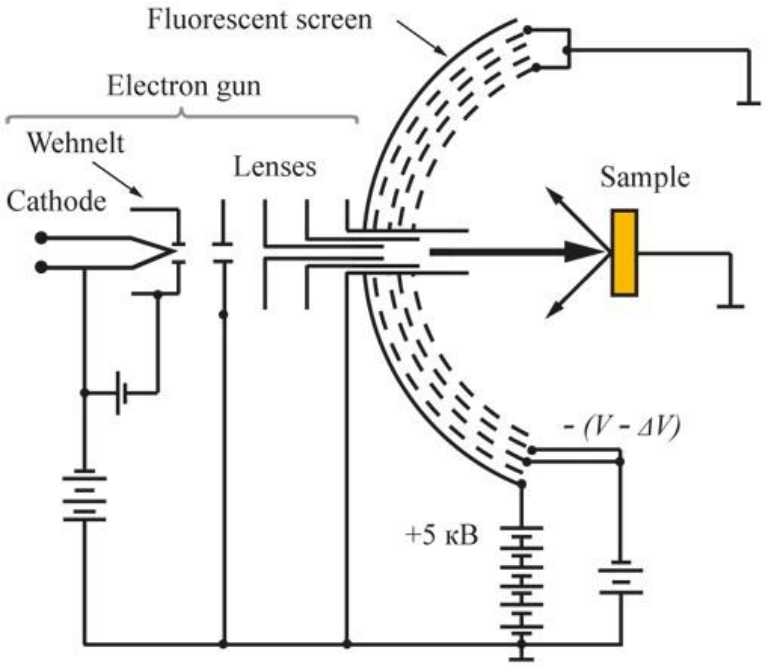

Figure 2.3 Diagram of a LEED apparatus

Diagram of a low-energy electron diffraction (LEED) apparatus, from Ref. 40. The apparatus is kept in vacuum to keep the sample surface clean. Electrons are emitted from an electron gun and then accelerated and focused into a beam by a series of electrodes. After interacting with the sample, some electrons are diffracted back. The grids in front of the florescent screen filter out inelastically scattered electrons so that only elastically backscattered electrons will reach the screen and form diffraction patterns.

The LEED may be used in one of two ways:

(1) Qualitatively, where the diffraction pattern is recorded and analysis of the spot positions (e.g. distance and angle) gives information on the symmetry of the surface. In the presence of a superlattice (e.g. due to adsorbates and/or surface reconstruction), the qualitative analysis may reveal information about the size and rotational alignment of the unit cell of the superlattice with respect to the substrate unit cell.

(2) Quantitatively, where the intensities of diffracted beams are recorded as a function of incident electron beam energy to generate the so-called I-V curves. By comparison with theoretical curves, quantitative LEED I-V may be used for structure determination and/or providing accurate information on atomic positions on the surface at hand.

2.2.1 LEED patterns: size, shape, and symmetry

Due to the low-energy scale of electrons used in LEED (20 – 500 eV), the electrons generally penetrate only a few Angstroms into the sample and interact "strongly" with atoms and electrons close to the surface. Upon penetrating a crystal, the intensity of the primary beam decays exponentially. This effective attenuation means that only the top few atomic layers are sampled by the electron beam and as a result the contribution of deeper atoms to the diffraction progressively decreases.[41]

In general, multiple scattering-events must be taken into account for theoretical description of the LEED. Nevertheless, a simple treatment of the surface scattering process within the framework of single scattering events can yield insights into important features of scattering on the surface.[42] This approach is called the kinematic theory. It is frequently used for qualitative explanation of the LEED patterns and may provide information such as size, shape, and symmetry of the unit cell of the surface structure.

For an incident beam of electrons with wave vector $\mathbf{k}$ and elastically scattered electrons with wave vector $\mathbf{k}'$ ($|\mathbf{k}'| = |\mathbf{k}| = 2\pi/\lambda$), the conditions for constructive inference are given by the Laue equations,

$$\mathbf{k}' - \mathbf{k} = \mathbf{G}, \tag{5}$$

where $\mathbf{G}$ is a reciprocal lattice vector.

Since only the first few atomic layers contribute to the diffraction, the problem can be approximated as 2D diffraction, in which case the Laue equations may be written as

$$\mathbf{K}_{\parallel} = \mathbf{k}'_{\parallel} - \mathbf{k}_{\parallel} = \mathbf{G}_{\parallel}, \tag{6}$$

i.e. the scattering vector component parallel to the surface must equal a vector of the 2D surface reciprocal lattice.

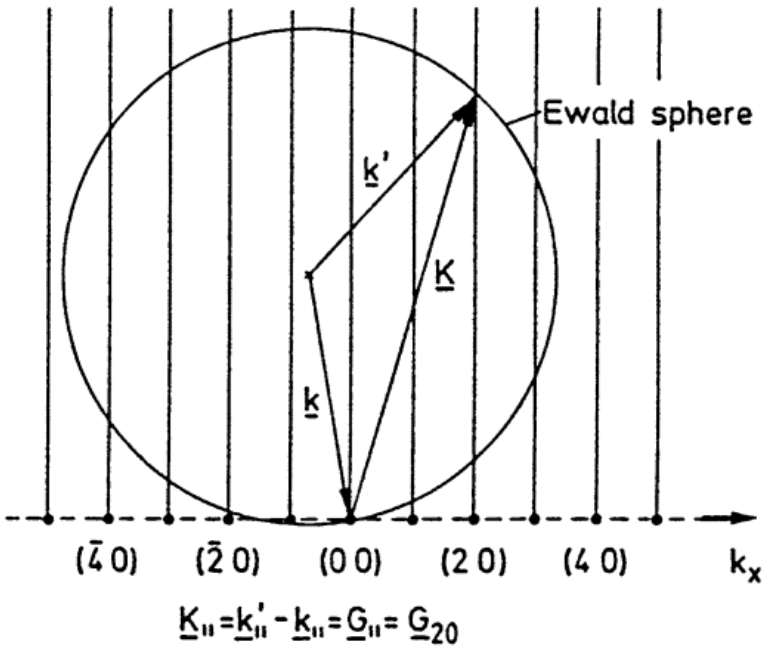

Figure 2.4 Ewald construction for 2D scattering

Ewald construction for elastic scattering on a 2D surface lattice, from Ref. 42. The 2D reciprocal lattice points (hk) are plotted on a cut along kx. The Laue equations in 2D are satisfied by points that are intersections of the rod and the Ewald sphere

In order to extend the Ewald construction for the 3D diffraction to the 2D problem, we must relax the restriction of the third Laue equation (perpendicular to the surface).[42] This is done by attributing to every 2D reciprocal lattice point (h,k) a rod normal to surface (Figure 2.4). This is because for a 2D lattice, the periodicity along the perpendicular direction is infinity. Correspondingly, the periodicity the reciprocal lattice in the *z* direction is zero, i.e. infinitely-densely packed. In the 3D problem we have discrete reciprocal lattice points in the third dimension instead of rods.

As shown in Figure 2.4, the possible elastically scattered beams $\mathbf{k}'$ can be obtained by the following construction. The wave vector $\mathbf{k}$ of the primary beam is positioned with its end at the (0, 0) reciprocal lattice point and its orientation is determined by the experimental geometry. The Ewald's sphere with radius $|\mathbf{k}|$ is then drawn with its center at the beginning of the incident wave vector $\mathbf{k}$. The condition

$\mathbf{k}'_{||} - \mathbf{k}_{||} = \mathbf{G}_{||}$ is fulfilled for every point at which the sphere crosses a reciprocal-lattice rod. By constructing every wave vector beginning at the center of the sphere and ending at the intersection of a rod and sphere, we obtain the diffraction pattern for the surface.

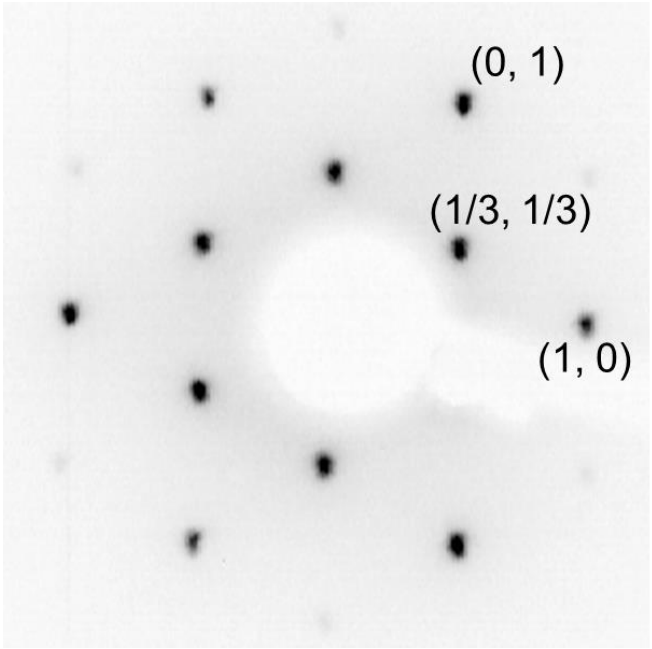

Figure 2.5 A LEED pattern example

LEED pattern for SiC (0001) surface after hydrogen etching at 1600 ℃ for 3 min, taken at beam energy 100 eV. The labeled (1, 0) and (0, 1) are the primary SiC spots. Fractional order spot (1/3, 1/3) indicates a superlattice. The orientation of the fractional order spot indicates that the unit cell of the super lattice is rotated 30 °relative to the primitive cell of the substrate. The standard notation for the superlattice is $\sqrt{3} \times \sqrt{3} - \mathrm{R}30^{\circ}$.

Figure 2.5 shows an example of a LEED pattern taken for a sample. The sample is a 6H SiC sample with the (0001) face as the surface. After hydrogen etching at 1600 ℃ for 3 min, the surface was studied with an in-situ LEED. The LEED pattern shows the primary spots of SiC (labeled as (1, 0) and (0, 1) in the figure) as well as fractional ordered spots (e.g. (1/3, 1/3) in the figure). The fractional order spots are due to a superlattice on the surface. Based on the distance of spot to the pattern center and

orientation with respect to the primary spots, we can determine the unit cell of the superlattice to be $\sqrt{3} \times \sqrt{3} - \mathrm{R30}^\circ$, where $\sqrt{3} \times \sqrt{3}$ denote size of the unit cell in terms of the primitive cell of the substrate and $\mathrm{R30}^\circ$ indicates that it is rotated 30° relative to the primitive cell.

2.2.2 LEED I-V

Let us first revisit the Ewald construction in Figure 2.4 of the previous section. Now we gradually increase the energy of the incident electron beam. The radius of the Ewald's sphere will vary correspondingly. As a consequence, more (higher order) rods intersect the sphere. In this process, one would expect the intensity of a diffraction spot will depend weakly on the incident beam energy, i.e. constant before a new rod intersect the sphere and decreases when it starts to intersect. However, experimentally this is barely the case. While it is observed that higher order spots emerge as incident beam energy increases, the intensity of a certain diffraction spot often varies drastically and non-monotonically. This is because the Ewald construction in Figure 2.4 is exact only in the limit of scattering from a true 2D layer of atoms. In a real LEED experiment, however, the primary electrons penetrate a few atomic layers into the solid. The deeper they penetrate, the more scattering events in the *z* direction perpendicular to surface contribute to the final LEED pattern.[42]

To take into account scattering from a few additional layers of atoms, we can modify the simple rod representation of the z direction of the 2D reciprocal lattice to rods with non-uniform weights, as shown in Figure 2.6. The "thicker" regions of the rods arise from the Laue equation in the third dimension, which cannot be completely neglected as in the pure 2D case. If the Ewald sphere intersects a rod at a thick region, a diffraction spot of strong intensity is expected, while if it intersects at a thin region, weak diffraction will occur.

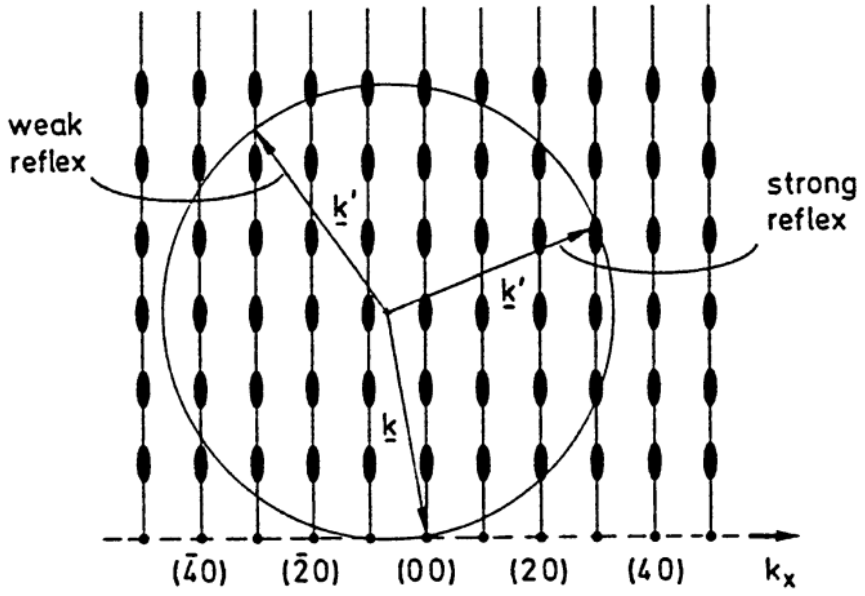

Figure 2.6 Ewald construction for scattering in quasi-2D lattice

Ewald construction for elastic scattering in a quasi-2D lattice, as in Figure 2.4, but now not only the topmost layer, but also a few underlying layers are considered. The "thicker" regions of the rods arise from the third Laue condition, which cannot be completely neglected as in the pure 2D case. From Ref. 42.

If we gradually increase the energy of the incident electron beam, the Ewald sphere will intersect thick and thin regions of a rod alternately, and the intensity of the corresponding diffraction spot will be oscillatory. The measurement of the intensity of a particular diffraction spot in dependence on the beam energy of incident electrons is known as LEED *I-V* measurement where *I* refers to intensity and *V* acceleration voltage of electrons. The oscillatory behavior of a LEED *I-V* curve is indeed observed in many experiments.[41,42,43] However, there are many additional features in the *I-V* curves that cannot be explained by the simple picture developed so far. These are beyond the single scattering approximation and multiple scattering processes must be taken into account.

On the other hand, the rich features of the *I-V* curves can provide detailed crystallographic information about a given surface.[44] Since multiple scattering effects in LEED are strong, general methods to extract the desired structural information directly from the *I-V* curves do not exist.[41,44] Instead, the structure and atomic configurations of

the surface are determined by a trial and error procedure, where theoretical *I-V* spectra are computed for many plausible models of the surface and then compared to experimental *I-V* curves to find the best match. From an initial reference structure, a set of trial structures can be created by vary the model parameters such as geometry, stoichiometry and thermal vibrations. The parameters are changed routinely and the comparisons keep going until an optimal agreement between the computed and the experimental *I-V* curves is achieved.

The agreement between the computed and the experimental *I-V* curves is characterized by a reliability factor (*R*-factor). A commonly used reliability factor is the one proposed by Pendry.[45] It is expressed in terms of the logarithmic derivative of the intensity,

$$L(E) = \frac{1}{I(E)} \frac{dI(E)}{dE}, \tag{7}$$

where intensity I is expressed a sum of a series of Lorentzian peaks,

$$I = \sum \frac{a_j}{(E - E_j)^2 + V_{\mathrm{oi}}^2}, \tag{8}$$

where V_{oi} is the imaginary part of the electron self-energy.[45]

The Pendry *R*-factor is then calculated as

$$R = \left(\sum_g \int (Y_{gth} - Y_{gexpt})^2 dE \right) / \left(\sum_g \int (Y_{gth}^2 + Y_{gexpt}^2) dE \right), \tag{9}$$

where $Y(E) = L^{-1} / (L^{-2} + V_{\mathrm{oi}}^2)$. In general, $R \leq 0.2$ indicates a good fit between computed and experimental *I-V*, $R \approx 0.35$ is considered mediocre and $R > 0.5$ is considered as a poor agreement.

I-V curves are typically computed by dynamical LEED calculations, with a muffin tin potential model.[41] The time to compute the electron wave diffracted from a surface by dynamical LEED scales essentially as N^3 with N the number of independent scattering centers in the unit cell.[44] Hence the computational effort to calculate a single LEED spectrum rises rapidly with growing complexity of the surface under consideration. For a

complex surface model, the number of parameters is large so is the number of trial structures. It is computationally impractical to do a full dynamical LEED calculation for every trial structure.

To resolve this complexity, the Tensor LEED approximation was proposed. Tensor LEED is a perturbative approach to the calculation of LEED *I*-*V* spectra.[46,47,48] It is based on the idea that while low-energy electron diffraction from a surface is governed by multiple scattering, a small distortion of a given reference structure will only cause a small change in the diffracted wave field and may be treated by the perturbation method. Once the full dynamic scattering from the reference surface is known, the wave functions of structurally similar surfaces can be deduced with computing time scaling only linearly with the number of atoms involved.

The procedure of LEED *I*-*V* calculations for surface crystallography can be summarized in the following steps:

(1) Perform LEED measurements on the desired surface and record intensity of diffraction spots as a function of the beam voltage, i.e. experimental *I*-*V*.
(2) Select an appropriate reference model using all available information (e.g. symmetry of the surface based on LEED patterns in (1)) and do a full dynamic LEED calculation for the reference model.
(3) Generate a set of trial structures by varying parameters such as atomic displacements and thermal vibrations on the reference model and obtain LEED *I*-*V* for each trial structure.
(4) Compute Pendry *R*-factor between the experimental *I*-*V* spectra and the computed ones for each trial structure.

Steps (2) – (4) are repeated until a satisfactory *R*-factor, i.e. a good fit between experimental and computed *I*-*V*, is obtained. In our work, we use the Erlangen Tensor LEED package[44] to perform the LEED *I*-*V* calculations.

2.3 Low-energy Electron Microscopy

Our lab utilizes a Low-energy Electron Microscope (LEEM) to study two-dimensional (2D) materials including graphene, hexagonal boron nitride (h-BN), transition metal dichalcogenides (TMDs) such as MoS_2 and others. The LEEM uses elastically backscattered electrons to image atomically clean surfaces and thin films. It is a true imaging technique imaging technique as opposed to scanning techniques, and has a resolution down to 10 nm. Our LEEM is a commercial LEEM III apparatus designed and built by Elmitec. Figure 2.7 is a diagram of the instrument.

Electrons are generated from a thermionic LaB6 filament in an electron gun (top right of Figure 2.7). The electron gun is biased typically at −20 kV. Once the electrons have left the filament, they are accelerated to high energy by a grounded extractor into the illumination column. The illumination column contains sets of electromagnetic focusing lens and deflectors that make the electrons into a thin, collimated beam and deflect it towards the magnetic beam separator. The beam is then curved through the magnetic beam and directed at the surface of a sample. Passing through the grounded objective lens, the beam is rapidly decelerated to low energy due to the large potential difference between the objective lens and the sample, which is also held at close to −20 kV. A potential difference (known as start voltage or sample voltage) can be applied between the sample surface and the gun filament, to alter the incident electron energy. Typically incident energies of 0 – 50 eV are employed. The electrons are then reflected or diffracted from the sample surface. These electrons pass back through the objective lens and are curved away from the incident beam by the magnetic beam separator before entering the imaging column. The imaging column used another set of lenses and deflectors to image the electrons on the micro-channel plate. Depending on the currents applied to the lenses, the image can either be a diffraction pattern or a real-space image. Due to low energies relative to the sample surface, the incident electrons only interact with the top few atomic layers of the sample. Hence LEEM is a very surface sensitive technique. In the following section, we describe commonly used operation modes in LEEM.

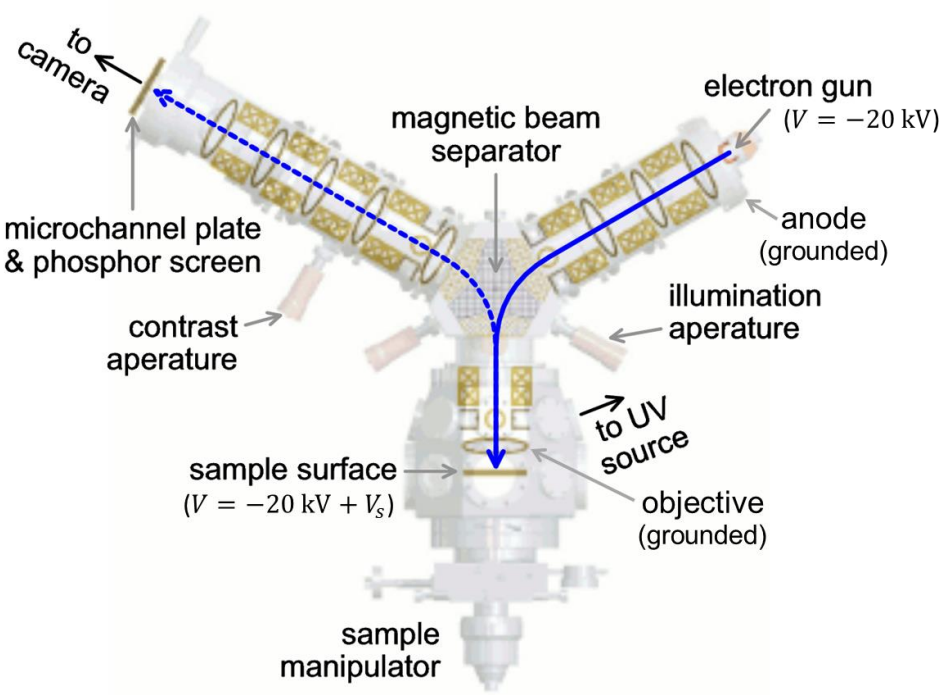

Figure 2.7 Diagram of the LEEM instrument

Diagram of the low-energy electron microscope (LEEM). Electrons are generated from an electron gun (top right) and accelerated by a large potential difference (20 kV) before being focused into a collimated beam by a set of electromagnetic lenses. The electron beam is then deflected towards the sample surface by a magnetic beam separator and decelerated by a large potential difference between the sample and objective lens (−20 kV + V_s), where V_s is a small, variable voltage (sample voltage) that controls the energy of electrons incident on the sample. After interacting with the sample, some of the incident electrons are scattered back. These electrons pass back through the objective lens and are curved away from the illumination beam by the magnetic beam separator into image column. The image column contains another set of electromagnetic lenses that focus the reflected electrons into a magnified image on a phosphor screen.

2.3.1 Imaging

For crystalline samples, in addition to being 180 °backscattered to the opposite direction, some of the incident electrons are diffracted to off-normal directions, meaning that they pick up some finite in-plane momentum component through interacting with the periodic

potential of the crystal. In imaging mode, only the normally-reflected (i.e. (0,0) diffraction) electrons are used to form final images. This is achieved by centering the contrast aperture (Figure 2.7) on the (0,0) diffraction spot formed on the back focal plane of the objective lens. The aperture blocks electrons with in-plane momentum, allowing images to be formed using only the normally-reflected electrons.

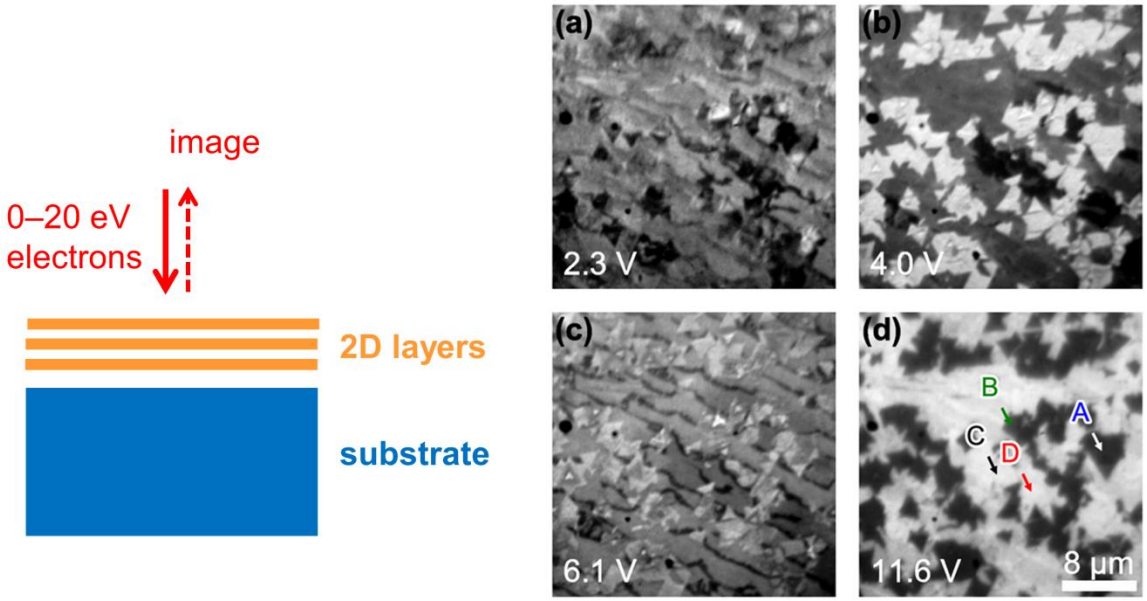

Figure 2.8 LEEM imaging mode

Left: Schematic of LEEM imaging. The normally reflected electrons are used to form images. Right: example LEEM images for the same surface taken at different sample voltages, from Ref. 49, showing clear contrast between different domains on the surface and dependence on the sample voltage.

Figure 2.8 shows schematic of the imaging mode and a few examples of LEEM images. The images are taken for the same surface taken at different sample voltages. The contrasts arise from different domains on the surface and thus reveal straightforwardly morphological information of the surface. We can pick any point on the surface (e.g. A (or B, C, D) on image (d)) and look in detail at how its imaged intensity varies with the start voltage and obtain spectroscopic information (more in Section 2.3.3).

2.3.2 Diffraction

The principle of diffraction mode in LEEM is the same as the standalone LEED system discussed in Section 2.2, but with some unique advantages. The primary advantage of the diffraction in LEEM is that we can select an area (of micrometer size) of the sample surface to be illuminated by the electron beam by inserting an aperture (illumination aperture in Figure 2.7) and obtain diffraction patterns exclusively for that area. This is known as selected-area LEED or μLEED as it allows examination of crystallinity on the micrometer scale. The selected-area LEED (μLEED) has been frequently used to study the quality of grown 2D materials such as crystallinity, grain size, and alignment in presence of vertical 2D heterostructures.

The crystallinity and grain size are often checked by examining the corresponding diffraction spots in the pattern. A bright, sharp diffraction spot is an indication of good crystallinity with a grain size comparable to the size of the illumination aperture inserted. In our LEEM, illumination apertures of three different sizes (8 μm, 5 μm, and 2 μm) are available. Faint, broadened diffraction spots or diffraction streaks or rings are indications of mediocre crystallinity with a grain size often considerably smaller than size of the aperture. The streaks or rings are a result of diffraction from rotationally disordered domains on the illuminated area. Diffraction patterns that only show a diffused bright background suggest bad crystallinity. Figure 2.9 shows an example of μLEED patterns for molybdenum disulfide – epitaxial graphene (MoS_2−EG) heterostructures synthesized by two different methods. The MoS_2 in (b) is grown via powder vaporization (PV), while it is synthesized via by metal oxide chemical vapor deposition (MOCVD) in (c). The diffraction patterns in Figure 2.9 give a direct measure of the quality of the grown MoS_2 crystals by the two methods.

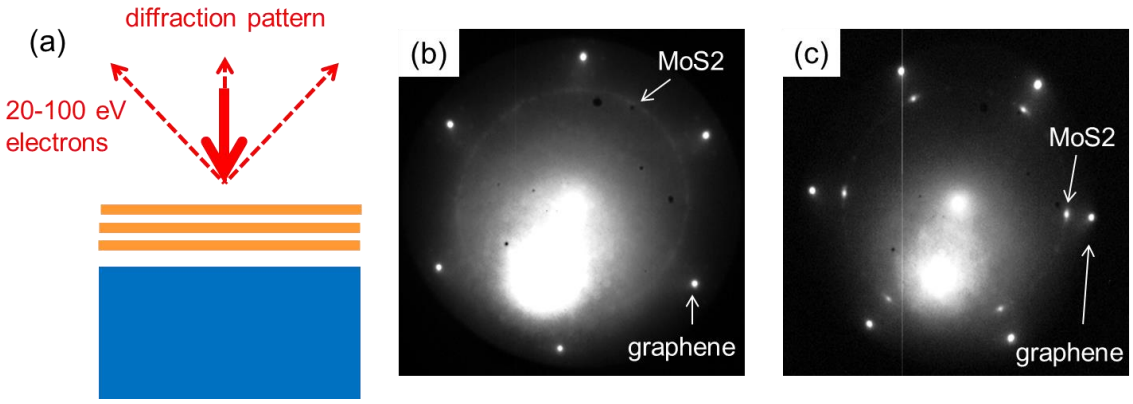

Figure 2.9 LEEM diffraction mode (μLEED)

Illustration of diffraction mode (a), a sample voltage in 20 – 100 V is typically employed, and diffracted beams in all directions (defined by the Ewald sphere construction discussed in Section 2.2) are used to produce the diffraction pattern. Selected-area LEED (μLEED) patterns (b) and (c) for molybdenum disulfide (MoS_2) − graphene heterostructures synthesized with two different methods. (b) MoS_2 is synthesized on epitaxial graphene (EG) by powder vaporization (PV). (c) MoS_2 is synthesized on EG via metal organic chemical vapor deposition (MOCVD). The EG in both samples are prepared by preferential sublimation of Si from Si-face 6H SiC. The ring feature of MoS_2 in (a) arises from randomly-ordered MoS_2 domains with grain size considerably smaller than the aperture size used (5 μm). The dominant spot feature of MoS_2 in (b) indicates a MoS_2 grain size comparable to the aperture size and the grown MoS_2 is epitaxial aligned with the underlying graphene. Both μLEED patterns are acquired at 45 eV.

2.3.3 Reflectivity

Let us re-examine the LEEM images in Figure 2.8. Not only do we see that different locations (domains) on the surface show different contrast at a given sample voltage, the contrast (intensity) at a fixed location also varies with the sample voltage. Spectroscopic information for a point on the surface may be obtained by recording the intensity, i.e. pixel values, at that point when sweeping the sample voltage. Such spectroscopic information is called low-energy electron reflectivity (LEER), or reflectivity for brevity, as the intensity corresponds to the amount of reflected electrons.

In our experiment, we record LEEM images for the whole field of view (FOV, selected from 2 – 150 μm) at a sequence of sample voltages in fine steps. A computer program is employed to automate this process and LEEM images are taken typically at each sample voltage from -5 V to 15 V or 20 V in increments of 0.1 V. The small negative sample voltages are used to obtain full reflectivity ($r = 1$), known as "mirror mode", and is important for determining local vacuum levels of domains on the sample surface (more in the next section 2.3.4). The acquired sequential LEEM images are all saved as a single video file. LEER for a location on the surface is then obtained by processing this video file, i.e. extracting intensity value at that location as a function of the sample voltage.

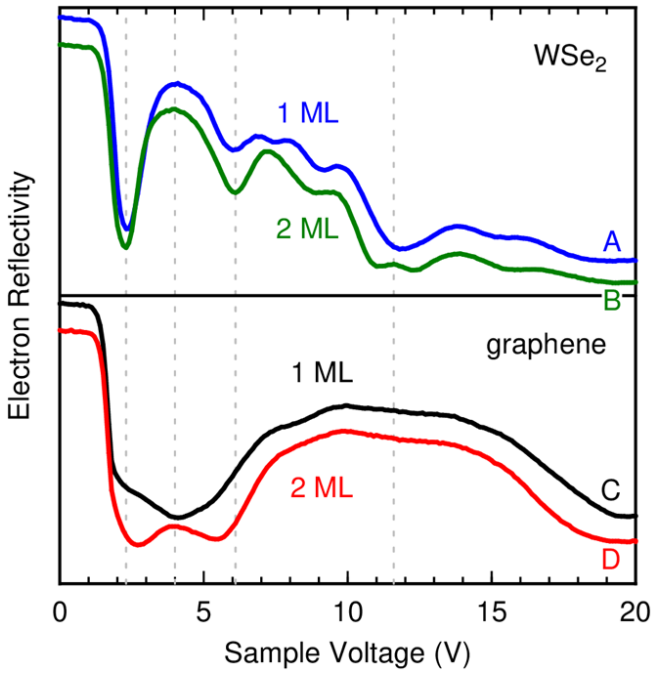

Figure 2.10 LEER example

An example of LEER, for points labeled in Figure 2.8(d), where only data in the positive voltage range is shown here. From Ref. 49.

Figure 2.10 shows an example of LEER for locations labeled Figure 2.8(d). The LEER spectra of a point on the surface are characteristic of the electronic structure at that point. As in Figure 2.10, not only the spectra vary drastically from material to material, e.g. WSe_2 and graphene, but detailed oscillations in the spectra for the same material are

dependent on the number of atomic layers. Reflectivity minima, e.g. located by grey dashed lines in Figure 2.10, in the oscillations originate from states that are localized between the monolayers of the 2D material, known as *interlayer states*. These characteristics have been studied both experimentally and theoretically,[50,51,49] and they provide an unambiguous way to identify the 2D material on the surface and count the number of 2D layers.

2.3.4 Work Function Difference

In addition to characterizing the material and thickness (e.g. number of atomic layers) of domains on the surface, the LEER spectra can also be used to extract information regarding the electrostatic potential variations across the surface, allowing comparison of work functions between different domains. The development of this method is published in *J. Mater. Res.* (2016).[12]

From Figure 2.7 and the description, we can see that the sample voltage, V_S is equal to the potential difference between the sample and the electron gun (cathode, which is an emitter made of LaB_6 crystal),

$$\begin{aligned} eV_S &= E_F^C - E_F^S, \\ &= (E_{VAC}^S - E_F^S) - (E_{VAC}^C - E_F^C) + E_{VAC}^C - E_{VAC}^S, \\ &= \Delta W + E_{VAC}^C - E_{VAC}^S, \end{aligned} \tag{10}$$

where E_F^S and E_F^C are Fermi levels of the sample and the emitter, respectively, E_{VAC}^S and E_{VAC}^C are their vacuum levels, and $W \equiv E_{VAC} - E_F$ is the definition of work function.

For a relatively ideal LEER spectrum such as in Figure 2.11(a), we see, as a function of decreasing voltage, a sharp onset (near 1.5 V) at with the reflectivity rises to unity. This signifies the transition to "mirror mode" of the LEEM;[52,53] as pictured in Figure 2.12(a), for sample voltage lower than this onset, the incident electrons do not have sufficient energy to reach the surface. Rather, they are reflected back by the electric

field (typically 10^4 V/mm) between the sample surface and the objective lens. For a sample voltage equal to the onset voltage, the vacuum levels of the sample and the emitter are aligned. Denoting the onset voltage by V_0, we have

$$eV_0 = \Delta W \,. \tag{11}$$

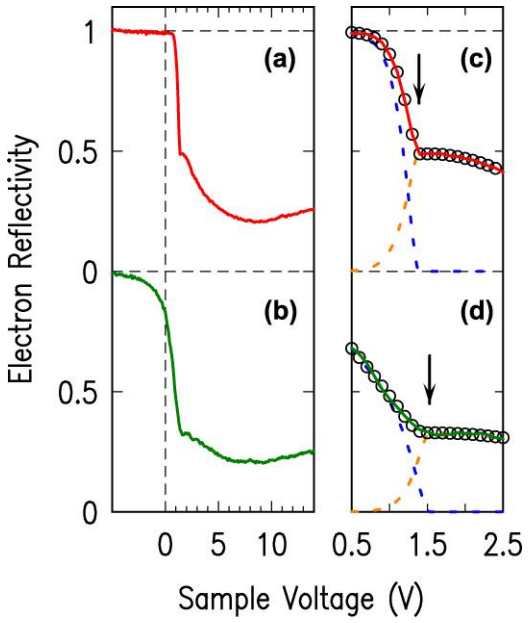

Figure 2.11 Typical LEER spectra with illustration of obtaining onset voltage through fit

Typical LEER spectra, with (a) displaying a sharp transition to unit reflectivity (near 1.5 V sample voltage) and (b) showing more gradual transition. (c) and (d) Expanded views of the transition regions form (a) and (b), respectively. Black circles show a fit function, with the arrows indicating the onset voltage derived from the onset. The two components of the fits, for each spectrum, are indicated by the dashed lines. From Ref. 12.

For voltages greater than the onset, all electrons are reflected from the sample surface or absorbed into the sample, as pictured in Figure 2.12(b). Note that in Figure 2.12, we have plotted the density of states of thermionically emitted electrons using the well-known energy distribution[54]

$$N(\epsilon) = \varepsilon \exp(-\varepsilon / \sigma_c) / \sigma_c^2, \tag{12}$$

with $\sigma_c = kT_c$ where k is the Boltzmann constant and T_c temperature of the emitter (cathode), wand with ε being the electron energy relative to E_{VAC}^c. This distribution is peaked at $\varepsilon = \sigma_c$, so that the incident electrons have peak energy of $\sigma_c + E_{VAC}^c$.

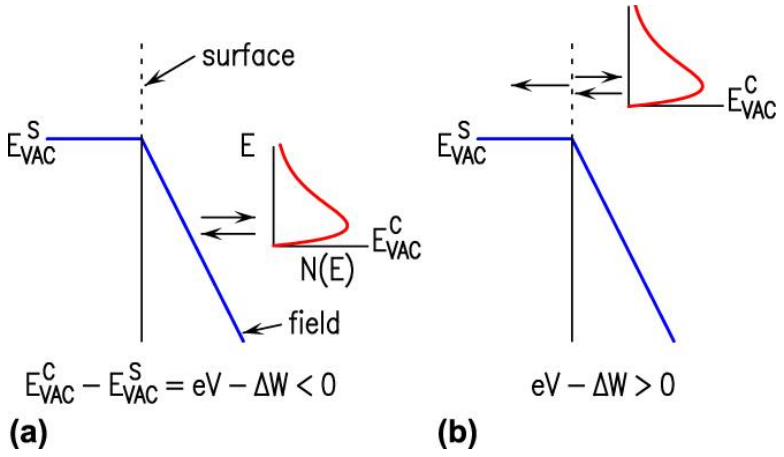

Figure 2.12 Energy diagrams of electrons incident on the surface of a sample

Energy diagrams of the distribution N(E) of electrons incident on the surface of a sample. In (a), the majority of electrons are reflected by the field extending out from the surface, whereas in (b) the electrons have sufficient energy to reach the surface, where they are partially reflected and partially absorbed.

Let us now consider find the onset voltage by fitting the LEER spectra in the transition region. In the transition region, the reflected electrons are composed of two parts: those do not have enough energy ($eV < \Delta W$, or equivalently $V < V_0$) to reach the sample surface and are reflected by the field; those have enough energy ($V > V_0$) and are partially reflected from the sample surface. For field-reflected (or mirror-reflected) electrons, we employ a fit function of the form[12]

$$g_m = \begin{cases} a_0\{1-[1-(V-V_0)/\sigma]\exp[(V-V_0)/\sigma]\}, & V \le V_0 \\ 0, & V > V_0 \end{cases} \tag{13}$$

where a_0 is a fit parameter. For the electrons reflected from the sample surface, we must assume some form for the reflectivity. We expand it as a 2nd degree polynomial about an energy of $e(V-V_0)$, yielding the fit function

$$g_s = \begin{cases} G_s\{1-[1-(V-V_0)/\sigma]\exp[(V-V_0)/\sigma]\}, & V \le V_0 \\ G_s, & V > V_0 \end{cases} \quad (14)$$

where $G_s = b_0 + b_1(V-V_0) + b_2(V-V_0)^2$, with b_0, b_1, and b_2 all being fit parameters.

Figure 2.11(c) shows results of fitting the transition region of the LEER spectra in Figure 2.11(a), with the blue dashed line representing the mirror-reflected component (13) and the orange dashed line the sample-reflected component (14).

In experiment, we also frequently obtain reflectivity spectra such as that of Figure 2.11(b), which displays a much slower approach of the reflectivity to unity as the voltage is decreased. This type of behavior is a signature of *lateral fields* on the surface of the sample, arising from a work function difference between neighboring surface areas.[53] A fit to the spectra in this situation can be made similarly as the above, although with a larger uncertainty error.[12,55]

3 Graphene Formation on C-face of SiC

In this chapter, we study structure of the interface that forms between graphene and SiC when the graphene is formed on the C-face of SiC. In particular, we focus on determining the structure of the $\sqrt{43}\times\sqrt{43}$-R7.6° surface observed for graphene formed in an environment of 5×10^{-5} Torr disilane. The graphene formed in disilane has been shown to be of better quality, i.e. larger grain size and better uniformity, than graphene formed in vacuum.[66,76] Therefore, studying the $\sqrt{43}\times\sqrt{43}$-R7.6° structure is not only scientifically interesting, but also helps us better understand the growth mechanism so that further improvement of the graphene quality may be attainable. The work presented in this chapter is under preparation for publication.[7] For these results, a prior graduate student, Guowei He, and the author (JL) did the experiments of annealing (i.e. heating) the C-face SiC to form graphene. The samples were annealed at varying temperatures in different pressures of disilane, and the surface phases both before and after graphene formation were studied with low-energy electron diffraction (LEED). The author also performed the quantitative LEED I-V analysis. Qingxiao Wang from the Moon group at University of Texas, Dallas did the scanning transmission electron microscopy (STEM) measurements. Prof. Michael Widom did first-principles calculations (using the Vienna Ab-initio Simulation Package, VASP) for surface structures without graphene coverage. Lydia Nemec from the Fritz-Haber-Institut der Max-Planck-Gesellschaft in Germany did first-principles calculations (using the FHI-aims all-electron code) for surface structures with graphene coverage. Prof. Randall Feenstra, Prof. Michael Widom and the author worked together in developing structural models of the surface and analyzing the computational results.

3.1 Introduction

Formation of graphene on SiC, by heating the SiC and producing preferential sublimation of Si compared to C, has been studied extensively for the past ten years.[18] The (0001)

surface, known as the *Si-face* of the two types of {0001} surfaces, has been employed in most of those studies; graphene with good structural and electronic properties can be produced on that surface.[56,57,58] It is known that between the graphene and the SiC there is an intermediate layer, a so-called buffer layer (Figure 3.1), consisting of a graphene-like structure but with some bonding to the underlying SiC, forming a $6\sqrt{3}\times6\sqrt{3}$-R30° unit cell.[59] As additional Si is sublimated from the SiC, this buffer layer eventually converts to pristine graphene and a new buffer layer forms below it.[60,61,62] Additionally, the buffer layer can be decoupled from the SiC by introduction of hydrogen or oxygen.[57,63,64]

For graphene formation on the $(000\bar{1})$ surface of SiC, known as the *C-face*, the situation is found to be more complex than for the Si-face (Figure 3.1), for several reasons: (i) there exists more than one way to form graphene on the surface, i.e. more than one interface structure has been observed between the graphene and the SiC,[65,66] (ii) the structural quality of the graphene on the C-face is generally much worse than for the Si-face,[67] and (iii) employing an inert gas or a Si-rich environment to improve the quality of the graphene, as works well for the Si-face,[56,68,69] is more problematic on the C-face. (One reason for the latter issue was found to be unintentional oxygen contamination of the inert gas,[67] which led to the formation on the C-face of a very stable *silicate structure*, Si_2O_3,[70] which *inhibits* graphene formation). However, despite these complexities, several research groups have actually achieved very good quality graphene on the C-face, better in certain respects than on the Si-face.[71,72,73,74] Those growths are performed with the SiC sample in a confined space, so that a background Si pressure is formed near the surface (although the precise value of that pressure, as well as the possible presence of other elements, is not accurately known).

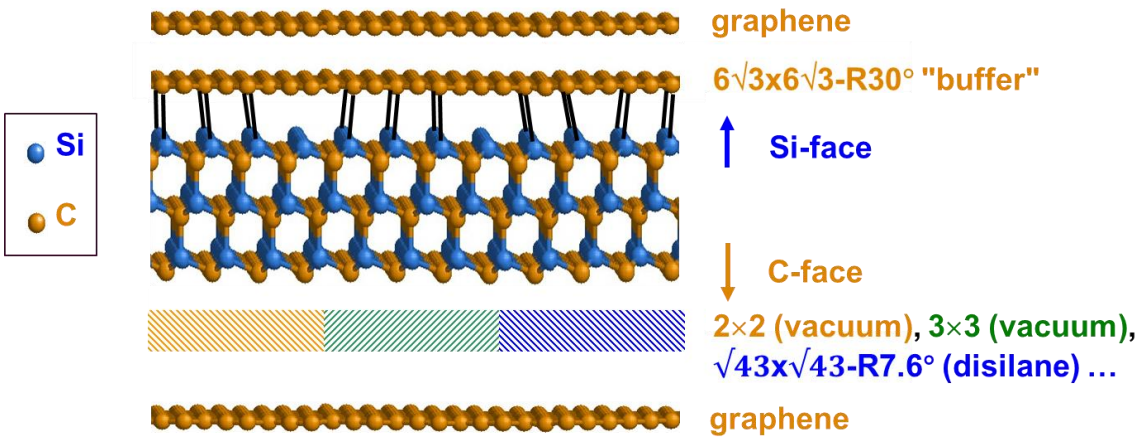

Figure 3.1 Graphene formation on {0001} surfaces of SiC

Schematic of graphene formation on Si-face and C-face of SiC. The interface on the Si-face is the $6\sqrt{3}\times6\sqrt{3}$-R30° buffer layer and its structure is well understood. For the C-face, multiple interfaces have been reported and their structures are less well understood.

The goal of the present work is to understand what interface structures form between graphene and C-face SiC, in an effort to understand and optimize the C-face graphene quality. In a prior work, we have reported on the formation of graphene on the C-face under conditions of a surrounding disilane (Si_2H_6) pressure of $P_d \approx 10^{-5}$ Torr. We observed the first layer graphene to form with a new structure associated with it, a $\sqrt{43}\times\sqrt{43}$-R7.6° reconstruction as observed by low-energy electron diffraction (LEED).[66] This graphene layer was found to form with a considerably larger grain size than for graphene typically formed on the C-face surface (5 μm vs. 50 nm grains).[66,75,76]

Our work is focused on the graphene formation on the C-face of SiC in the disilane environment. Specifically, we perform experimental and theoretical studies of surfaces both before and after graphene formation on the C-face. In experiment, LEED patterns and intensity profiles of diffraction spots are obtained for diverse surfaces at different heating temperatures and disilane pressures. Cross-sectional scanning transmission electron microscopy (STEM) along with energy dispersive spectroscopy (EDS) and electron energy loss spectroscopy (EELS) is carried out for the graphitized sample after air exposure. In theory, we do an extensive structure search and first-

principles computations, along with quantitative LEED I-V analysis of the diffraction patterns, to identify the surface before and after graphene formation.

The most important conclusion of this work is an "adatom-on-adlayer" model that is found to describe surface structures both before and after graphene formation. In more detail, we conclude that the surfaces prior to graphene formation consist of Si adatoms on top of a Si adlayer structure, and this adatom on adlayer structure persists even after the graphene has been formed. The formation of such a Si-rich surface in a C-rich environment may at first appear surprising. However, similar situations have been previously known for the N-face of GaN.[77] Essentially, in a compound semiconductor, when atoms of different types have different sizes and most importantly, the smaller atom is relatively stable in its elemental form, then the adatom-on-adlayer structure can be energetically stable. In the case of N-face of GaN, N_2 is a stable molecule, and the surface is terminated by Ga even in N-rich conditions. In our case of C-face of SiC, graphite is relatively stable, and it makes sense that the surface is terminated by Si (aside from possible graphite formation) even in C-rich conditions.

3.2 Background

Figure 3.2 shows LEED patterns for graphene formation on Si face and C face of SiC respectively. The LEED pattern for Si face (Figure 3.2(a)) indicates a $6\sqrt{3} \times 6\sqrt{3}$-R30° superstructure. This superstructure is understood as a corrugated, graphene-like buffer layer that is partially bonded to the Si atoms of the SiC substrate.[59,78] For the graphene formation on C face, a $\sqrt{43}\times\sqrt{43}$-R$\pm$7.6° diffraction pattern is observed (Figure 3.2(b)). Unlike the $6\sqrt{3}\times6\sqrt{3}$-R30° on the Si face, much less is understood for the $\sqrt{43}\times\sqrt{43}$-R$\pm$7.6° on the C face. Previous work based on LEEM[76] has shown that the graphene formed in this case has a grain size much larger than graphene formed in vacuum which typically shows a LEED pattern with graphene streaks and no spots. It was found that the $\sqrt{43}\times\sqrt{43}$-R$\pm$7.6° surface converts to an oxidized $\sqrt{3}\times\sqrt{3}$-R30° surface after air exposure.[66] Prior work by He et al [43] showed, on the basis of LEED *I-V* analysis, the $\sqrt{3}\times\sqrt{3}$-R30° pattern arises from a Si_2O_3 "silicate" interface structure. This structure is Si-rich, containing two-thirds of a monolayer of Si atoms terminating the

surface so the presence of this silicate (below the graphene) is broadly consistent with the conclusions of the present work. However, the conclusions of this prior study are somewhat uncertain due to a degassing procedure used in the LEEM observation (after the surface/interface structures were formed), during which the samples were heated to 1000 ℃ for a minute or longer;[43] in principle this procedure can cause significant structural changes to the surface or interface. In contrast, for the results reported here, no such post-formation annealing steps were performed.

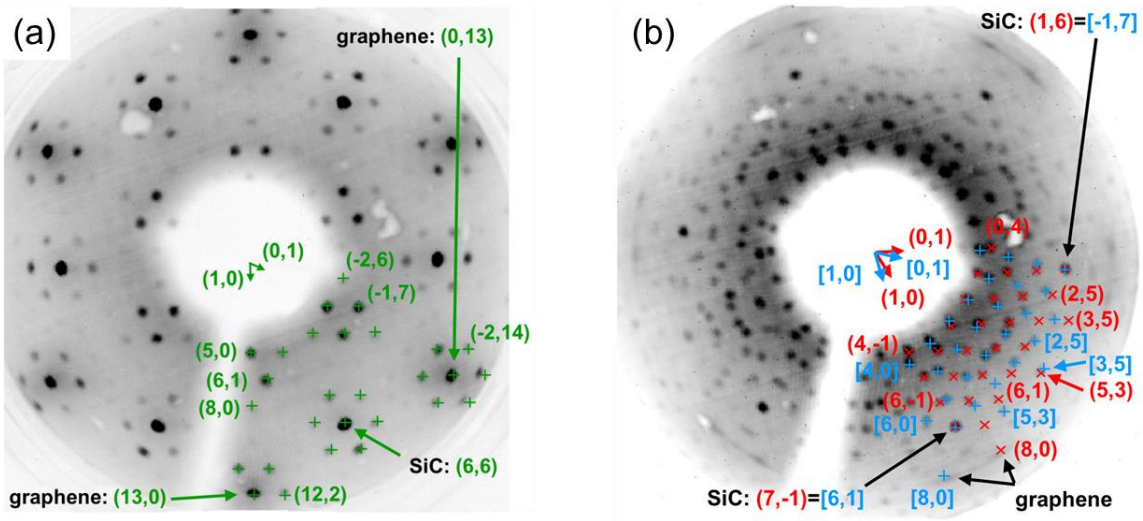

Figure 3.2 LEED patterns for graphene formation on {0001} surfaces of SiC

LEED patterns for graphene formation on the Si face of SiC (a), showing diffraction spots corresponding to a superlattice of $6\sqrt{3}\times6\sqrt{3}$-R30°, sample prepared by heating SiC in 1 atm of argon at 1470 ℃ for 15 min; for graphene formation on the C face of SiC (b), showing diffraction spots corresponding to a superlattice of $\sqrt{43}\times\sqrt{43}$-R $\pm$ 7.6°, sample prepared by heating SiC in 5×10^{-5} Torr of disilane at 1270 ℃ for 15 min. Adapted from Refs. 66,76.

In this work, we study the surface structure both before and after the graphene forms on the C-face of SiC in a disilane environment, both experimentally and theoretically. We summarize our results as the following:

1) the surface prior to graphene formation on the C-face (in disilane) consists of a Si-rich adatom-on-adlayer structure.
2) previously reported 2×2 and 3×3 structures for graphene formation on the C-face in vacuum are kinetically limited, i.e. not equilibrium surface structures.
3) the Si-rich adatom-on-adlayer structure persists (albeit with rearrangement of the adatoms) after the graphene forms. The $\sqrt{43}\times\sqrt{43}$-R$\pm$7.6° diffraction spots are primarily from this adatom-on-adlayer interface, rather than from the graphene.
4) the graphene layer itself probably follows a different periodicity, namely 6×6 SiC unit cells (which fits to $\sqrt{57}\times\sqrt{57}$-R$\pm$6.5° graphene unit cells).

3.3 Experimental and Theoretical Methods

The experiments are performed on nominally on-axis 6H-SiC or 4H-SiC wafers, with no apparent differences found between results for the two types of wafers. The wafers are cut into 1×1 cm^2 samples and the samples are chemically cleaned in acetone and methanol before putting them into our custom-built preparation chamber (base pressure ~1×10^{-9} Torr) which uses a graphite strip heater for heating the samples and a leak valve for introducing disilane.[79] To remove polishing damage, the samples are heated in either 1 atm of hydrogen at ~1600 ℃ for 3 min or 5×10^{-5} Torr of disilane (Si_2H_6) at 850 ℃ for 5 min, after which the gas supply and sample heating is shut off. We then increase the sample temperature to some specific value between 1150 and 1350 ℃, and we introduce disilane up to a pressure between 10^{-6} and 10^{-4} Torr (with most studies performed at 5×10^{-5} Torr). Characterization by LEED is performed *in situ* in a connected ultra-high vacuum (UHV) chamber. LEED patterns from semiconducting 6H-SiC samples are recorded in steps of 2 eV in an energy range of 80 – 380 eV. Quantitative LEED intensity analysis of that data is used to provide auxiliary evidence of particular surface structures discussed below.

Ex situ cross-sectional STEM measurements were performed to study the interface structure of C-face SiC after graphene coverage, with a JEOL ARM200F microscope. Both high-angle annular dark-field (HAADF) imaging mode and annular bright-field (ABF) imaging mode are used to obtain cross-sectional views of the sample.

Energy dispersive spectroscopy (EDS) and electron energy loss spectroscopy (EELS) have been performed to analyze the chemical composition of the surface.

For first-principles density functional theory (DFT) calculations, we have used both the Vienna Ab-initio Simulation Package (VASP)[80,81] with the projector augmented wave method and the FHI-aims all-electron code.[82,83,84] Both types of computations employ the van der Waals (vdW) corrected [85] Perdew-Burke-Enzerhof (PBE) [86] generalized gradient approximation (GGA) for a density functional, and dipole corrections are included according to the method of Neugebauer and Scheffler.[87] Both computational methods utilize slabs consisting of six 3C-SiC bilayers with cubic lattice constant of 4.364 Å, and a graphene lattice constant of 2.463 Å[84] We find in our computations that results from the two methods generally agree within a few meV. The bottom Si atoms in the slab are hydrogen terminated, and all the atoms in each structure considered are fully relaxed. The relative surface energy γ of a structure is given as

$$\gamma = \frac{1}{A}(E_{\text{tot}} - E_{\text{slab}} - N_{\text{Si}}\mu_{\text{Si}} - N_{\text{C}}\mu_{\text{C}} - N_{\text{H}}\mu_{\text{H}}) \qquad (15)$$

where E_{slab} is energy of the bare SiC slab, and E_{tot} is total energy of the structure after relaxation. N_{Si}, N_{C} and N_{H} denote the number of Si, C and H *adatoms* on the surface, respectively, and μ_{Si}, μ_{C} and μ_{H} refer to chemical potentials of Si, C and H. In thermal equilibrium we have $\mu_{\text{Si}} + \mu_{\text{C}} = E_{\text{SiC}}^{\text{bulk}}$, from which we eliminate μ_{Si} in Eq. (1). Limits on μ_{C} are determined by bulk phases, $E_{\text{SiC}}^{\text{bulk}} - E_{\text{Si}}^{\text{bulk}} \le \mu_{\text{C}} \le E_{\text{C}}^{\text{bulk}}$. We use graphite as the carbon bulk phase, cubic (diamond) silicon as the silicon bulk, and cubic (zincblende) SiC as the silicon carbide bulk. As a reference point for μ_{H} we take $E_{\text{H}} \equiv E_{\text{H}_2}^{\text{DFT}}/2$, where $E_{\text{H}_2}^{\text{DFT}}$ is the DFT-computed energy of the H_2 molecule.[88]

3.4 Results

3.4.1 LEED study of surface reconstructions before and after graphene formation

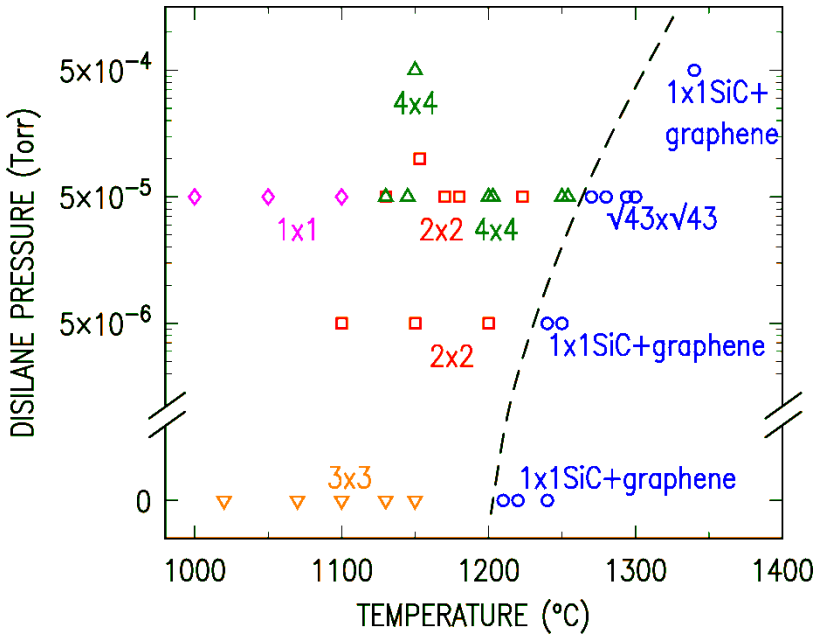

Figure 3.3 Overview of experimental results

Overview of experimental results, showing the symmetry of observed LEED patterns. Each data point represents a surface prepared by 5 minutes of heating at the temperatures and disilane pressures indicated. LEED patterns to the right of the dashed line contain graphene spots (indicating the presence of graphene on the surface), while those to the left of the dashed line do not contain graphene spots.

Figure 3.3 is an overview of our experimental results, showing the symmetry of observed LEED patterns on the C-face surface as a function of temperature and disilane pressure. Let us first consider the situation in the absence of any disilane, in which case we always observe the formation of a 3×3 pattern on our SiC surface after heating in UHV to a temperature of 1020 °C. At higher temperatures, graphene forms on the C-face surface by the well-known mechanism of preferential sublimation of Si atoms.[89] The 3×3 pattern

persists on the surface even when the graphene spots in the diffraction pattern are observed to start forming. We emphasize that this 3×3 pattern is by far the dominant one that we observe on our surface just prior to the formation of the graphene; this observation applies not only for the vacuum system used in the present studies but also for another set of studies that we performed in a separate chamber that has 1×10^{-10} Torr base pressure and includes a getter pump to reduce background levels of H. (This predominance of the 3×3 structure is consistent with most prior reports, although some authors also report substantial amounts of a 2×2 structure, a point that we discuss in Section 3.4.3).[65,66,67,76,90]

As seen in Figure 3.3, when disilane is introduced at pressure of about 5×10^{-6} Torr or higher, the situation changes dramatically. We now reproducibly observe only 2×2 or 4×4 surface reconstructions at temperature below where the graphene forms (this graphene formation temperature also increases substantially as the disilane pressure increases, as expected). Samples showing 2×2 patterns and those with 4×4 patterns were prepared using nominally the same procedures. At disilane pressure near 5×10^{-5} Torr, there appears to be some subtle (not well understood) difference in surface conditions that determines whether one or the other of these structures is obtained, while for lower pressures we uniformly observe the 2×2 patterns and at higher pressure ones we mainly observe 4×4. As we further increase the temperature to form graphene, we reproducibly observe the $\sqrt{43}$ reconstruction for disilane pressures near 5×10^{-5} Torr. In contrast, for disilane pressures of 5×10^{-6} Torr or 5×10^{-4} Torr, we obtain a "1×1SiC+graphene" pattern, which contains streaks at the graphene spot locations (located typically at 10-15 ° relative to the SiC (1,0) spots), along with the underlying SiC spots.

Figure 3.4 shows typical LEED patterns of some surfaces displayed in Figure 3.3. In Figs. 2(a) and 2(b) we show examples of the 2×2 and 4×4 LEED patterns, i.e. as observed for heating temperatures below that for which graphene forms. Again, these are the patterns that we generally observe in our experiments. However, in a single experiment (using nominally the same conditions) we observed a different pattern, shown in Fig. 2(c). This pattern has its main superstructure spots concentrated around the $\sqrt{3}\times\sqrt{3}$-R30 ° positions, and it has a multiplicity of spots indicative of a disordered

surface arrangement, i.e. reminiscent of the LEED pattern of Ge(111)*c*(2×8) observed by Vitali et al.[91] Hence, we refer to it as a disordered $\sqrt{3}\times\sqrt{3}$-R30° arrangement. The LEED pattern of Fig. 2(c) was obtained with nominally the same surface preparation treatment (heating in 5×10^{-5} Torr disilane at 1180 ℃ for 5 min) as those of Figs. 2(a) and 2(b). Subsequent additional heating was performed on the surface of Fig. 2(c): two cycles of heating under nominally the same conditions as before (5×10^{-5} Torr disilane, 1180 ℃, 5 min). Following the first cycle the LEED pattern changed to a pattern showing both 4×4 peaks and disordered $\sqrt{3}\times\sqrt{3}$-R30° features, and following the second it changed to an almost purely 4×4 pattern (i.e. like Fig. 2(b)). We measured LEED *I-V* characteristics of the surface following each cycle of heating, and we have compared those to *I-V* data from surfaces displaying 2×2 (Fig. 2(a)) or 4×4 (Fig. 2(b)). It turns out that the *I-V* curves of integer-order spots from all these surfaces closely resemble each other. We therefore conclude that all of these surfaces have related structures. Hence, it appears that the structure of the 4×4 surface is *not* some monolithic one that cannot be broken down into smaller subunits, but rather, it contains subunits which, when differently arranged (and/or slightly modified), constitute the 2×2 surface of Fig. 2(a) and/or the disordered surface of Fig. 2(c). For comparison to these the 2×2, 4×4, and related LEED patterns, in Fig. 2(d) we show a typical 3×3 pattern obtained in the absence of any disilane, emphasizing the dramatic change that occurs on the surface when the disilane is present during the heating. Further heating leads to graphene formation. Depending on the pressure of disilane used, either the $\sqrt{43}\times\sqrt{43}$-R±7.6° pattern or the 1×1SiC+graphene is observed.

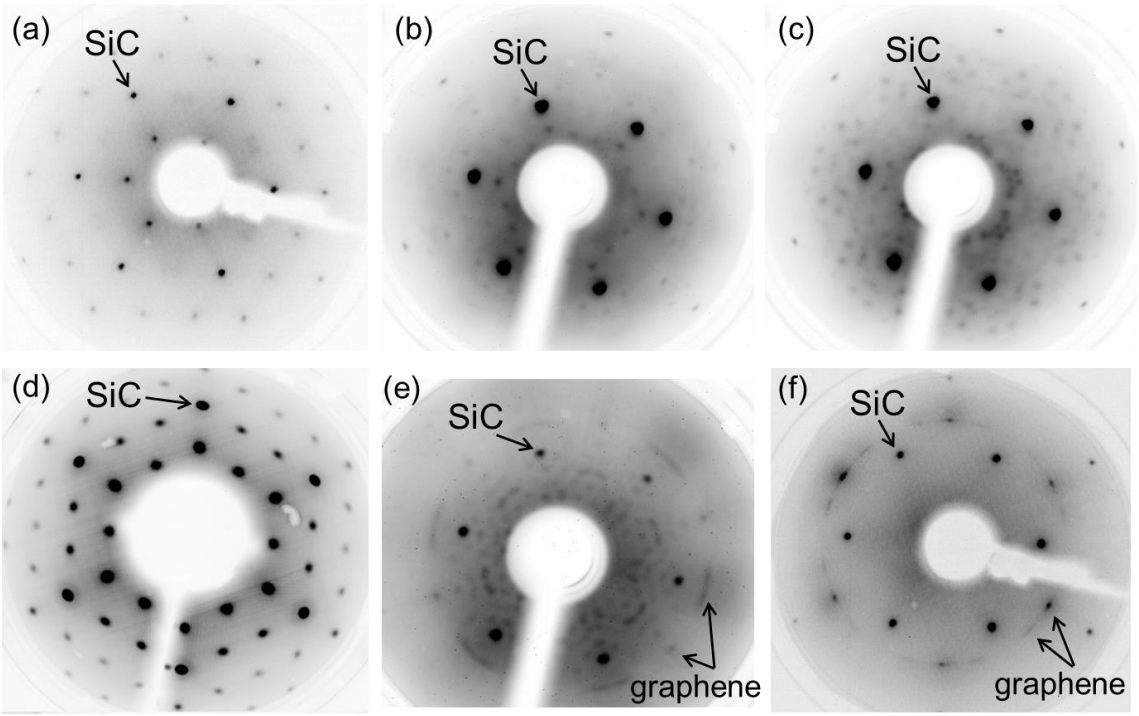

Figure 3.4 LEED patterns of surfaces in Figure 3.3

LEED patterns of (a) 2×2, (b) 4×4, (c) disordered $\sqrt{3}\times\sqrt{3}$-R30°, (d) 3×3, (e) $\sqrt{43}\times\sqrt{43}$-R±7.6°, (f) 1×1SiC+graphene, all acquired at 100 eV. Patterns (a) – (c) were obtained from samples prepared under nominally identical conditions: heating in 5×10^{-5} Torr disilane at 1180 ℃ for 5 min. Pattern (d) was obtained from a sample heated at 1070 ℃ for 10 min in vacuum (without any disilane).

3.4.2 STEM study of the surface reconstructions after graphene formation

Cross-sectional STEM measurements are performed by our collaborators, Prof. Moon Kim's group in UT Dallas, on our graphitized C-face samples. The sample has been exposed to air before sending it to Dallas. The results show that the graphene coverage on these samples is typically 2 – 4 layers. Figure 3.5 shows HAADF imaging and ABF imaging of an area where there are four layers of graphene on the surface, for one of the samples. What is the most interesting about the result is the fact that there is a "thick" amorphous layer between the first layer of graphene and the top layer of the SiC. The

amorphous layer has a thickness of 1.0 nm. For comparison, the interlayer distance between graphene monolayers in few layer epitaxial graphene is 0.33 nm[59,92] and the interlayer distance between SiC bilayers is 0.24 nm.[92] The thickness of the amorphous layer is much greater than the distance (0.6 nm[59,92]) between the first layer of graphene and the top layer of the SiC on the Si face. This 0.6 nm distance include a graphene-like buffer layer between the SiC and the graphene.[59,92] Therefore, the interfacial structure on the C-face appears to consist of more than a monolayer of atoms. This is consistent with the adatom-on-adlayer structure we will discuss below. The spectroscopic measurements in Figure 3.6 indicate the amorphous interfacial layer is a SiO_x layer. The oxidization is not surprising as the sample has been exposed to air for a few months before being measured by the cross-sectional STEM.

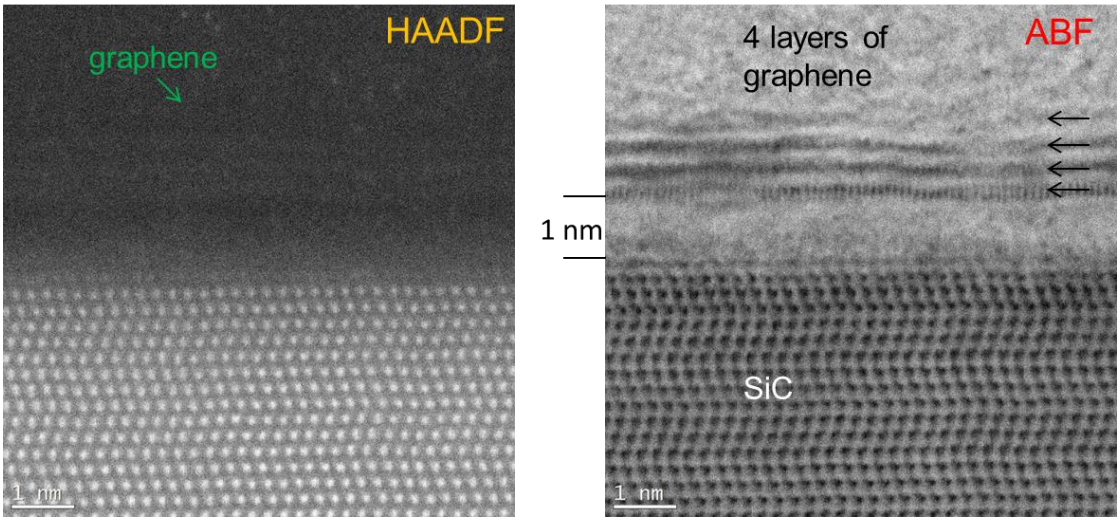

Figure 3.5 Cross-sectional STEM imaging of graphitized C-face SiC

Cross-sectional scanning transmission electron microscopy (STEM) measurements of graphitized C-face SiC sample in (a) High-angular annular dark-field (HAADF) imaging mode, (b) Annular bright-field (ABF) imaging mode. Four layers of graphene are observed for this region of the sample surface.

Figure 3.6 shows results of EDS and EELS measurements along direction perpendicular to the surface. In this example, we used the same sample as in Figure 3.5 but performed the measurements on a different region of the sample where there are three

layers of graphene on the surface. The HAADF image on the left again shows a thick interfacial layer between graphene and SiC. The EDS measurements in Figure 3.6(b) indicates the interfacial layer is silicon oxide since increases in the Si spectrum and in the O spectrum are observed as the scan enters the layer while the C signal decreases. Similar results are obtained by the EELS measurements as shown in Figure 3.6(c) (O spectrum not shown). The EELS line scan is more sensitive to graphene layers. The labeled three peaks in Figure 3.6(c) correspond to three graphene layers on the surface.

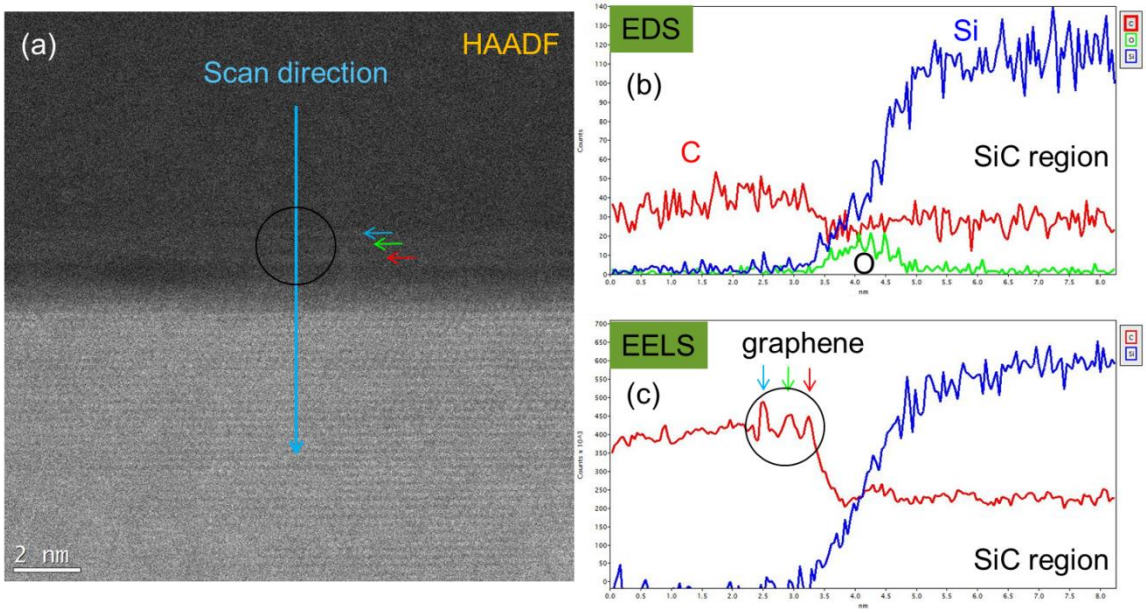

Figure 3.6 EDS and EELS measurements of graphitized C-face SiC

Energy dispersive spectroscopy (EDS) and electron energy loss spectroscopy (EELS) line scan measurement along direction perpendicular to the surface of graphitized C-face SiC. (a) HAADF cross-sectional image showing a region where there are three layers of graphene, with scan direction indicated. (b) EDS line scan results, showing composition of the interfacial layer. (c) EELS line scan results, showing signals corresponding graphene.

3.4.3 First-principles theory, without graphene coverage

Before going into details, we briefly introduce notations used in the following discussion. We refer to atoms on the bulk SiC surface as *adatoms*. The adatoms can be bonded to

different sites on the surface. For example, h3 refers bonding on a hollow site, and t4 denotes bonding atop the second layer of the top SiC bulk layer. Three adatoms that form a tetramer is abbreviated as tetra. We define ml (monolayer) = adlayer = 1 adatom per (1×1) SiC unit cell.

To understand the structure of the 2×2 and 4×4 surface found in the presence of disilane, we have performed an extensive set of first-principles calculations of surface energies. We have considered structures with adatoms of different species (C/Si/H or a mix of them), quantity and arrangements, with full or partial adlayers, with adatoms on adlayers. For all the structures considered, we compute their energies as a function of C chemical potential and H chemical potential. The structures with the lowest energy are then identified and displayed in Figure 3.7.

We see from the Figure 3.7(a) that when the chemical potential of H in the system is low (bottom), the lowest energy structures at the Si rich limit (leftmost) and at the C rich limit (rightmost) are the (3×3)-13Si(ml, tetra) structure and the (3×3)-5Si structure, reproducing the results in vacuum[84,93]. Our notation here refers to the fact that the (3×3)-13Si(ml, tetra) consists a monolayer of Si and a tetramer of Si adatoms on top of the monolayer (Figure 3.7(d)).[84] The (3×3)-5Si contains 5 Si adatoms arranged in such a way that they form a net of equilateral hexagons on the surface.[93] Close to the C-rich limit, the (2×2)-5Si, becomes the lowest energy structure. This surface model consists of a Si monolayer and a Si adatom on top (at a t4 site relative to the top bilayer of the bulk SiC; see Figure 3.7(g) for a side view and Figure 3.8(a) for a top view).[93] Interestingly, this model, after fully relaxing the surface to its energy minimum, has its Si adatoms arranged in positions slightly deviates away from high-symmetry sites. A new structure found by us, (4×2)-11Si(ml, h3, 2t4), containing a Si monolayer with additional three Si adatoms on top (one at a h3 site and two at t4 sites, Figure 3.8(b)), turns out be of the lowest energy, over a fairly wide range of C chemical potential in the intermediate region (from slightly Si rich to modestly C rich). Figure 3.7(h) shows a side view of this model.

As we move upwards along the H chemical potential in Figure 3.7(a), when $-2.41\ \text{eV} \le \mu_H - E_H \le -2.15\ \text{eV}$, we see that while (3×3)-13Si(ml, tetra), (4×2)-11Si(ml, h3, 2t4), (2×2)-5Si remain as the lowest energy structure in their corresponding C

chemical potential range, the (3×3)-5Si is replaced by (3×3)-5Si-H_C as the lowest energy structure. The (3×3)-5Si-H_C structure also gradually cut into the region represented by (2×2)-5Si and completely dominates when $\mu_H - E_H > -2.15$ eV . The (3×3)-5Si-H_C surface model is structurally similar to the (3×3)-5Si, but with an H adatom terminating the surface C atom that is not bonded to any Si adatoms. As the H chemical potential continue to increase, the (3×3)-5Si-H_C gradually overcomes (4×4)-11Si(ml, h3, 2t4) in some modestly C-rich region. When the H chemical potential is even higher (> -1.60 eV), the (1×1)-H structure, which simply has all the dangling bonds of the C-face terminated by H atoms, starts to dominate aforementioned structures and become the lowest energy structure.

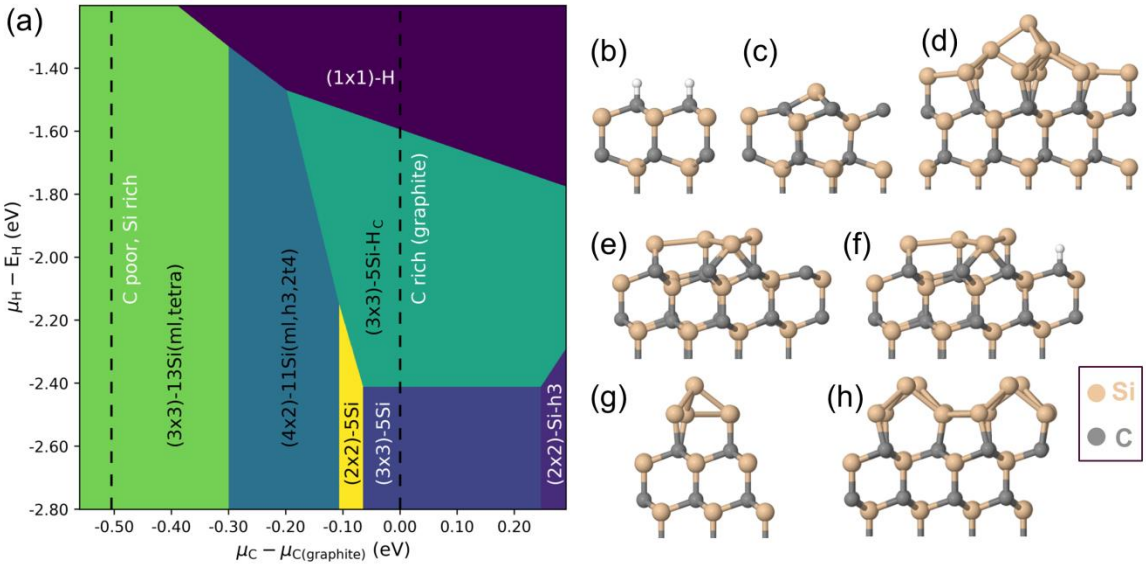

Figure 3.7 Phase diagram of lowest energy structures without graphene coverage

Lowest energy structures at different domains of C and H chemical potential. (a) Phase diagram for the lowest energy structures on the SiC$(000\bar{1})$ surface as a function of both the C and H chemical potential, among all structures considered. Two black dashed lines denote the C chemical potential at bulk Si rich limit (bulk Si) and C rich limit (graphite) respectively. (b) – (h) side views of the lowest energy structures shown in (a): (b) (1×1)-H, (c) (2×2)-Si-h3, (d) (3×3)-13Si(ml,tetra), (e) (3×3)-5Si, (f) (3×3)-5Si-H_C, (g) (2×2)-5Si, (h) (4×4)-11Si(ml,h3,2t4).

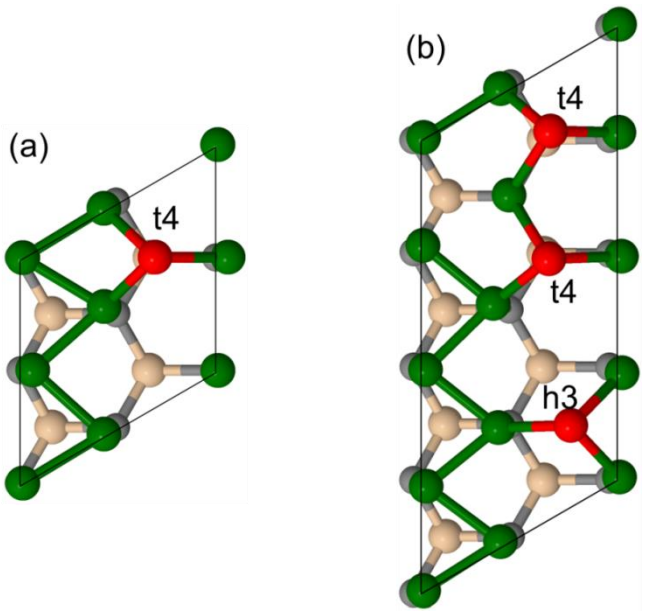

Figure 3.8 Top views of 2×2-5Si and 4×2-11Si

Top views of 2×2-5Si (a) and 4×2-11Si (b). For clarity, we only include one SiC substrate bilayer rather than the six used in the computation. Additionally, we color atoms in the Si adlayer by green and the top Si adatom by red for ease of viewing. Symmetry sites (h3, t4) of the adatoms are labeled. The black lines denote the unit cells of the two structures. Hence, the 2×2-5Si has a Si adlayer and one Si adatom at a t4 site. The 4×2-11Si has a Si adlayer and three Si adatoms on top of the adlayer. Two of the adatoms are at t4 sites and the other one is at a h3 site.

From an experimental point of view, although we have always observed the 3×3 diffraction pattern for graphene formation in vacuum, we never see such a pattern in presence of disilane. Nor do we see a 1×1 pattern right before graphene forms for the amount (pressure) of disilane we normally use (Figure 3.3). Instead, what is dominantly observed is the 2×2 and 4×4 patterns shown in Figure 3.4(a) and (b), under similar experimental conditions (Figure 3.3). Combing these facts with the theoretical results in Figure 3.7, we conclude that the (2×2)-5Si and (4×2)-11Si(ml, h3, 2t4) surface models are responsible for the LEED patterns obtained in presence of disilane. In other words, they are the surfaces we obtain prior to graphene formation in disilane. Specifically, the 2×2 pattern originates from the (2×2)-5Si structure, while the 4×4 pattern arises from different domains of (4×2)-11Si(ml,h3,2t4). These different domains can give rise to

missing fractional spots along lines passing through the primary SiC spots[41], consistent with the experimental pattern (the missing spots are seen for all LEED patterns acquired at a range of energies, 90 – 114 eV, not only for the one at 100 eV shown in Figure 3.4(b)).

Due to their particular importance, we show top views of the 2×2-5Si and 4×2-11Si in Figure 3.8. We note that both of these models consist of a Si monolayer and additional Si adatoms on top of the monolayer. This adatom-on-adlayer structure is not a fundamentally new class of structures since, as mentioned in the Introduction, such structures have been previously known for the N-face of GaN.[76] Nevertheless, these structures with a full adlayer of the "minority" species (e.g. Si for the SiC surface under C-rich conditions, or Ga for the GaN surface under N-rich conditions) are still quite noteworthy. The quantitative LEED I-V analysis in the next section further confirms the importance of the Si adlayer in these SiC surface structures.

We distinguish the 2×2 pattern in our experiment (with disilane) from another 2×2 pattern observed by many other research groups for graphene formation on C-face of SiC in vacuum.[18,65,94,95] The latter one is generally ascribed to the $(2\times2)_C$ structure, which has a Si adatom at the h3 site per unit cell (Figure 3.7(c)). We have renamed the $(2\times2)_C$ structure to (2×2)-Si-h3 in the present work, to explicitly state the type and position of the adatom. By examining Figure 3.7(a), the (2×2)-Si-h3 structure does not show up in any of the feasible regions of the phase diagram (delimited by the two black dashed lines) for the lowest energy structure (even after extending the H chemical potential to lower limit, i.e. vacuum). This is consistent with the recent theoretical results,[93] indicating that the 2×2 surface prepared in vacuum is not of thermal equilibrium (kinetically limited).

We have also done a careful comparison between the LEED pattern of our 2×2 surface (prepared in disilane) and that of the $(2\times2)_C$ surface (prepared in vacuum) reported by other research groups, and found that the two 2×2 patterns are very different for spots of corresponding indices. Most notably, the (1/2, 1/2) and its symmetrically equivalent spots are absent in our pattern (Figure 3.4(a)) at the energy shown, whereas they are clearly seen for the $(2\times2)_C$ surface in vacuum.[94,96] In contrast to that result, we also find that, at the same energy, our 2×2 pattern is very *similar* to another 2×2 pattern

reported in Ref. 96. That 2×2 surface in Ref. 96 is prepared at 1150 ℃ under Si-flux, a condition that can be considered similar to ours. In a separate work by the same group,[94] they measured this surface to be significantly more Si-rich than the $(2\times2)_C$ prepared in vacuum. Hence, it is quite possible that the surface they obtained has the same structure as ours, and are both of the (2×2)-5Si structure described above.

We point out that all the first-principles computations in this work are performed at a temperature of 0 K. However, our graphene is typically formed at ~1500 K (Figure 3.3). At such high temperature, additional effects such as entropy may have to be taken into account. In fact, we argue in Section 3.5 that the adatom-on-adlayer structure, (2×2)-5Si / (4×2)-11Si, rather than the (3×3)-5Si or the (3×3)-5Si-H or the (1×1)-H in Figure 3.7, is the lowest-energy structure immediately before graphene formation under our experimental conditions.

3.4.4 LEED I-V Analysis

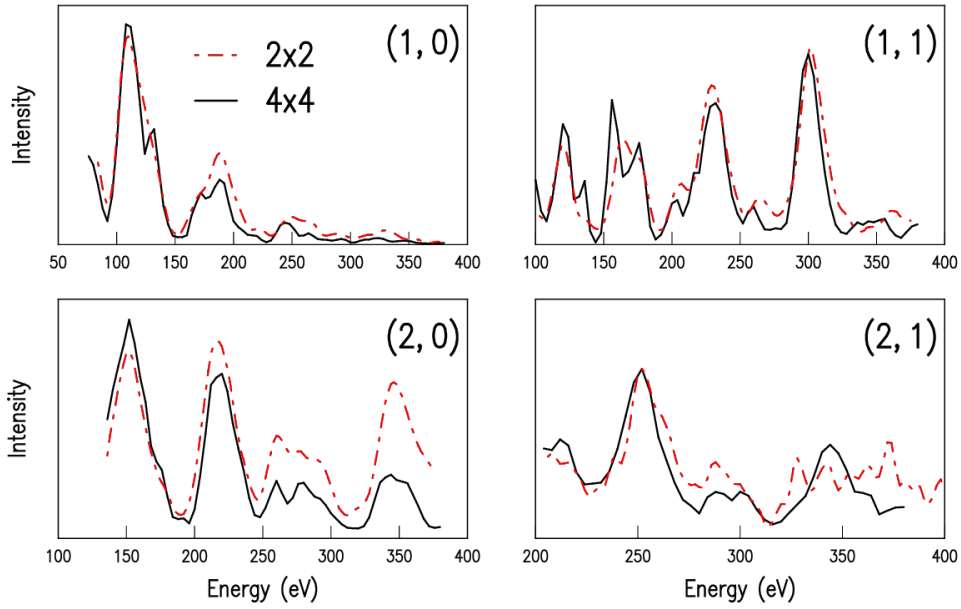

Figure 3.9 LEED I-V for 2×2 and 4×4

LEED I-V spectra of the 4×4 surface compared to that of the 2×2 surface. The two surfaces are prepared under nominally the same conditions, i.e. annealing in 5×10^{-5} Torr of disilane at 1160 ℃ for 5 min.

To gain further insights into the 2×2 and 4×4 surfaces in presence of disilane, we study the LEED I-V spectra of these two surfaces. Figure 3.9 shows the experimental I-V curves of the two surfaces (for integer spots, which they have in common). We note that the I-V curves for the 4×4 surface are very similar to those for the 2×2; hence, the structures of each appear to be nearly the same.

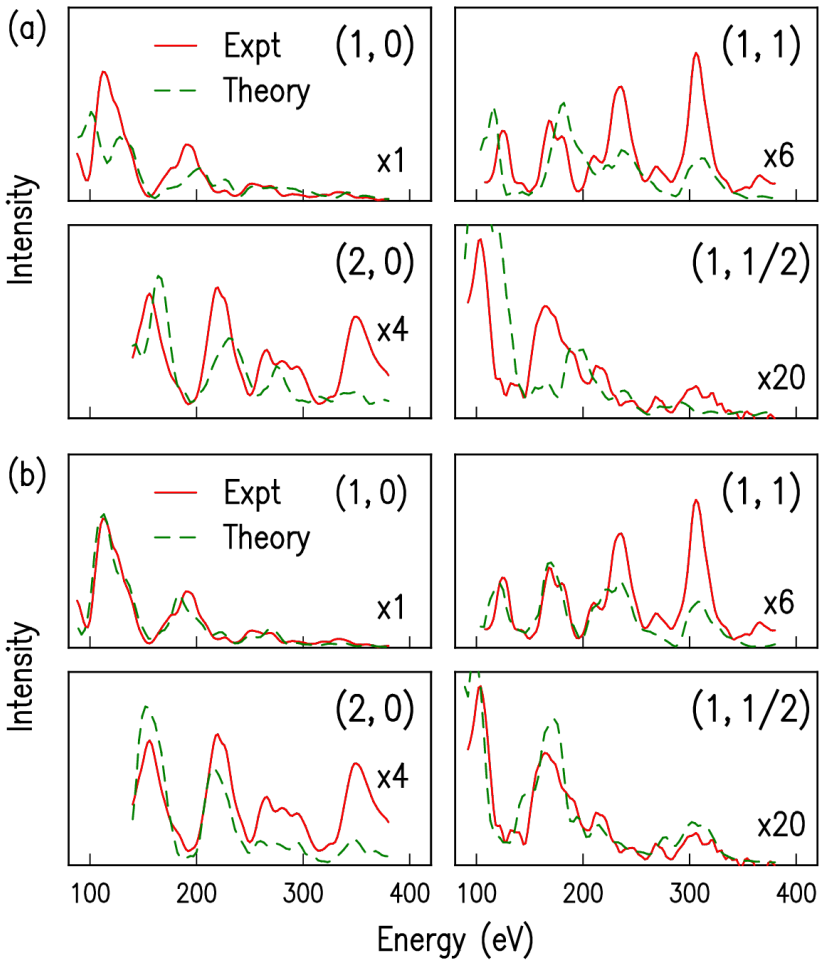

Figure 3.10 Computed LEED I-V compared with experiment

Computed LEED I-V (green dashed line) compared with experimental I-V (red line) for different orders of spots for (a) (2×2)-Si-h3 model, (b) (2×2)-5Si model. The R-factor computed is 0.64 for (a) and 0.34 for (b).

To confirm that the (2×2)-5Si model is the correct model for our 2×2 surface, we perform a quantitative LEED I-V computation. We take the coordinates of atoms computed by the first-principles theory (VASP) and input it into the LEED I-V

simulation package. Unlike what is commonly done with the simulation, we do *not* relax positions of the atoms after the initial I-V spectra are obtained. This is because the structure is already fully relaxed in the first-principles calculation, so that any further relaxation within the LEED I-V simulation package itself (i.e. to achieve a better match the experimental I-V) will just tend to produce unphysical arrangements of the atoms. Figure 3.10 shows that computed I-V compared with experiment, for the (2×2)-5Si model as well as the (2×2)-Si-h3 (commonly known as $(2\times2)_C$ in the literature). By visually inspecting the spectra and comparing the R-factors, we see that the match between the computed I-Vs for (2×2)-Si-h3 and the experimental ones is very poor, effectively excluding the possibility of this model as the correct one for our surface. In comparison, for the (2×2)-5Si model, a much better agreement is achieved; the R-factor decreases from 0.64 for (2×2)-Si-h3 (poor agreement) to 0.34 for (2×2)-5Si (moderately good agreement).

3.4.5 First-principles theory, with graphene coverage

Let us now consider the energetics when a layer of graphene is included on the surface, for which we employ the FHI-aims package that permits computations for relatively large numbers of atoms in a unit cell.

The major conclusions from the studies in this section is that the $\sqrt{43}\times\sqrt{43}$-R$\pm$7.6° LEED pattern observed for graphene formation on C-face SiC under disilane conditions cannot arise from the graphene layer itself. Rather, it must arise from the Si-rich adatom on adlayer structure discussed in the previous section, with possible rearrangement of the adatoms. This conclusion is significantly different from graphene formed on the Si-face of SiC, where the dominant $6\sqrt{3}\times6\sqrt{3}$-R30° LEED pattern is known to arise from the graphene-like buffer layer. As shown in the following, by both first-principles calculation and close examination of the LEED pattern, we conclude the $\sqrt{43}\times\sqrt{43}$-R$\pm$7.6° must arise from the Si-rich adatom on adlayer structure beneath the graphene.

Figure 3.11 shows the computed results for a subset of surface models we considered. For clarity, we adopt a new notation for describing these models, $(n\times n)$–

$(m \times m)$–*xxx*, where $(n \times n)$ is the size of the entire surface unit cell, $(m \times m)$ is the size of the unit cell at the interface, and *xxx* denotes the numbers of Si adatoms and H atoms at the interface along with their bonding environments. Since graphene is formed on the surface, we fix the C chemical potential at that of graphite and look at the surface energy as a function of the H chemical potential.

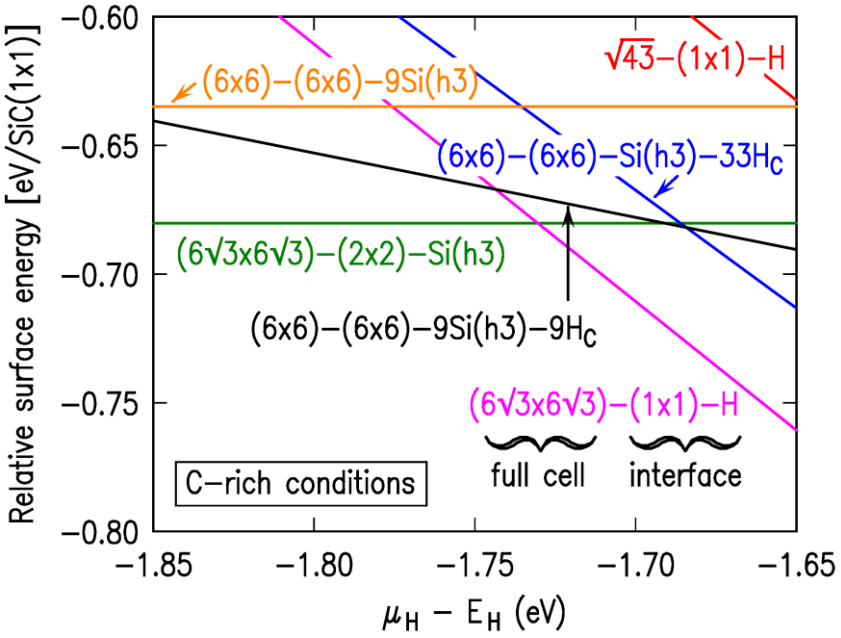

Figure 3.11 Surface energies for various C-face SiC surface models with graphene coverage

Surface energies for various SiC$(000\bar{1})$ surface structures including graphene. Energies relative to the bulk-terminated (1×1) phase are plotted as a function of the H chemical potential, for C-rich conditions (graphite).

To perform the first-principles computation for the graphene-on-SiC surface, a unit cell is specified such that the graphene lattice is commensurate with that of SiC$(000\bar{1})$. For the models displayed in Figure 3.11, the $(6\sqrt{3} \times 6\sqrt{3})$–(1×1)–H model has the well-known13×13 graphene unit cell being commensurate with $6\sqrt{3}\times6\sqrt{3}$-R30° SiC,[18,78] while the $\sqrt{43}$– (1×1)–H model has a 8×8 graphene fit to $\sqrt{43}\times\sqrt{43}$-R7.6° SiC,

as suggested by previous work.[66] The $(6\times 6)-(m\times m)-xxx$ models are for a low-strain commensurate fit between $\sqrt{57}\times\sqrt{57}$-R6.5° graphene and 6×6 SiC.[18]

The computed total energies for the $\sqrt{43}\times\sqrt{43}$-R7.6° models all turn out to be relatively high (most of them, except the $\sqrt{43}-(1\times 1)-$H, are outside the energy scale of Figure 3.11, and thus not shown here). In particular, the total energy of a model that has graphene placed directly on bulk-terminated C-face surface (using 8×8 graphene that have the closest lattice match to the $\sqrt{43}\times\sqrt{43}$-R7.6° cell[66]), is even higher than the bulk-terminated 1×1 surface itself (whose energy is used as reference energy in e.g. Figure 3.11). This is a bit surprising as the bonding between the bulk-terminated surface and the graphene would be expected to produce some energy lowering. The reason for the high energy of this model can be ascertained by comparing the energies of models $\sqrt{43}-(1\times 1)-$H and $(6\sqrt{3}\times 6\sqrt{3})-(1\times 1)-$H (Figure 3.11). For $(6\sqrt{3}\times 6\sqrt{3})-(1\times 1)-$H, there is relatively little strain in the graphene (discussed in more detail below), and the resulting energy is found be quite close (0.04 eV/SiC(1×1) higher) to that of a H-terminated C-face surface. In contrast, model $\sqrt{43}-(1\times 1)-$H has an energy that is 0.13 eV/SiC(1×1) *higher* than that of $(6\sqrt{3}\times 6\sqrt{3})-(1\times 1)-$H. We attribute this difference primarily to strain of the graphene layer in $\sqrt{43}-(1\times 1)-$H. As listed in Table 1, using our theoretical lattice constants (4.364 Å for 3C-SiC and 2.463 Å for graphite, both of which happen to agree well with the experimental values at room temperature),[97,98] the strain in the graphene for the $\sqrt{43}$ model is $\varepsilon = 0.0270$, and employing a graphene elastic constants of $C_{11}+C_{12}=414$ N/m and $2C_{111}/3-C_{222}/3+C_{112}=-1026$ N/m, [99] we obtain a biaxial strain energy change of

$$(C_{11}+C_{12})\varepsilon^2+(2C_{111}/3-C_{222}/3+C_{112})\varepsilon^3=0.145 \text{ eV/SiC}(1\times 1), \qquad (16)$$

which is reasonably close to the energy difference of models $\sqrt{43}-(1\times 1)-$H and $(6\sqrt{3}\times 6\sqrt{3})-(1\times 1)-$H.

This relatively large biaxial strain in a structure with 8×8 graphene unit cells matched to $\sqrt{43}\times\sqrt{43}$ SiC unit cells becomes even worse if we employ lattice constant appropriate to the preparation temperature of ~1500 K, as shown in the lower part of

Table 1 (the lattice parameter of graphite at 1500 K is not well known, but it appears to be little different than the room temperature value and hence we employ our theoretical value in this case).[100, 101] Indeed, re-examining the $\sqrt{43}\times\sqrt{43}$-R$\pm$7.6° experimental LEED patterns (Figure 3.2(b)), it is clear that the graphene does *not* have a 8×8 fit to the graphene, but rather its diffraction spot is a streak located at a wavevector that is 2.0±0.5% larger than that of $8/\sqrt{43}$ times the (1,0) SiC spot, and it is spread over angles of about 5 – 8° relative to the (1,0) SiC spot.

To summarize the discussion above, the graphene lattice cannot form a commensurate fit with $\sqrt{43}\times\sqrt{43}$-R$\pm$7.6° SiC without inducing significant strain in the graphene layer; diffraction spots (streaks, to be precise) are off (albeit by a small amount) from the location expected by a $\sqrt{43}\times\sqrt{43}$-R$\pm$7.6° lattice. We therefore conclude that the observed $\sqrt{43}\times\sqrt{43}$-R$\pm$7.6° LEED pattern must arise from the Si-rich adatom-on-adlayer interface discussed in the previous section, with possible rearrangement of the adatoms.

To understand the graphene streaks in the diffraction pattern, we have examined models with 13×13 graphene cells on a $6\sqrt{3} \times 6\sqrt{3}$-R30° SiC cell, as well as with a $\sqrt{57}\times\sqrt{57}$-R±6.5° graphene cell on a 6×6 SiC cell. Of course, both of these epitaxial fits will yield diffractions spots that are mostly missing in the diffraction pattern (Figure 3.2(b)). Nevertheless, we examine them in an effort to obtain energetically favorable structures. Notably, the $\sqrt{57}\times\sqrt{57}$-R±6.5° graphene on 6×6 SiC yields a very low misfit as seen in Table 1, and additionally this model will yield diffraction spots for graphene that are close to experimental observations in terms of both the angle ($\approx \pm 7°$) relative to the principal SiC directions) and the radius, i.e. magnitude of the wavevector.

Table 1 Lattice misfit for various commensurate fits of graphene on SiC

Lattice misfit f for various commensurate fits of graphene on SiC, as computed for given lattice parameters (Å) of the graphene and the SiC. Surface lattice parameter for SiC is $a_{\mathrm{SiC}}/\sqrt{2}$ where a_{SiC} is the cubic, bulk value. For unit cell side lengths of n_{C} and n_{SiC} for the graphene and SiC, respectively, $f = (n_{\mathrm{SiC}}a_{\mathrm{SiC}}/\sqrt{2} - n_{\mathrm{C}}a_{\mathrm{C}})/n_{\mathrm{C}}a_{\mathrm{C}}$, and this value equals the in-plane strains ε_{xx} and ε_{yy} in the graphene.

a_{C}	$a_{\mathrm{SiC}}/\sqrt{2}$	n_{C}	n_{SiC}	f
2.463[a]	3.086[a]	13	$6\sqrt{3}$	0.0016
		8	$\sqrt{43}$	0.0270
		$\sqrt{57}$	6	-0.0043
2.463[a,b]	3.097[b]	13	$6\sqrt{3}$	0.0052
		8	$\sqrt{43}$	0.0306
		$\sqrt{57}$	6	-0.0007

[a] first-principles theory (this work)

[b] estimated at 1500 K from theory and/or experiment (Refs. 97,98,100,101)

3.5 Discussion

We first note that the first-principles results in Section 3.4.3and 3.4.5 are all computed at a temperature of 0 K. However, our graphene is typically formed at ~1500 K (Figure 3.3). At such high temperature, not only do the values of lattice parameters change (Table 1), but other effects such as entropy may play a significant role. In fact, we argue here that (2×2)-5Si and/or (4×2)-11Si are the true minimal energy surface structures for C rich conditions, immediately before graphene forms. That is to say, we argue that the right-hand boundary of these phases in Figure 3.7 will expand further to the right, all the way to a C chemical potential close to that of graphite (at the applicable graphene formation temperature, ~1500 K).

The most important part of our argument comes from the observation that, in dozens of experiments, we have never observed a 3×3 LEED pattern for our graphene

formation on C-face SiC in disilane, although 3×3 is by far the domain pattern we see for graphene formation in vacuum. Instead, under disilane conditions (>1×10^{-6} Torr) we routinely observe 2×2 and 4×4, as discussed in Section 3.4.1. The larger grain size and better uniformity of graphene formed in disilane compared to that in vacuum[76] indicate that the former is carried out under better equilibrium conditions than the latter. In other words, the 3×3 (and the $(2\times2)_C$ observed by other research groups,[18,65,94] but not us) formed in vacuum are probably kinetically limited. In comparison with graphene formation in vacuum, at least three variables change when introducing the disilane,

(1) additional supply of Si due to disilane (through decomposition),
(2) additional supply of H due to disilane,
(3) higher graphene formation temperature.

The third change is a result of the first, i.e., the additional Si reducing the net sublimation rate of Si (due to conditions closer to equilibrium) and hence slowing the graphene formation rate.[18,71,73] We have shown that the Si-rich adatom on adlayer models, (4×2)-11Si and (2×2)-5Si, are the lowest-energy structures before graphene formation. The Si supply can be critical in achieving these non-kinetically-limited, Si-rich surface structures by offsetting the Si sublimation from the SiC. As the annealing temperature further increases, graphene starts to form. During this process, the adatom-on-adlayer structures are likely to persist as we only slightly increase the temperature ($\Delta T \leq 20$ ℃, Figure 3.3), with possible rearrangement of the adatoms. The relatively thick SiO_x interfacial layer seen in cross-sectional STEM images (Figure 3.5) for graphene covered surface after oxidization also favors this conclusion. The energy difference (0.04 – 0.06 eV/SiC(1×1)) between these structures ((4×2)-11Si and (2×2)-5Si) and the lowest-energy structure (3×3)-5Si (in appropriate range of H chemical potential) may be explained by an entropy argument. At such a high temperature (~1500 K), entropy effect cannot be ignored. Due to abundant Si atoms present on the surface, entropy, both configurational and vibrational entropy is more significant for the adatom-on-adlayer structures, thus leading to a greater reduction in free energy. Additionally, rearrangement of the adatoms (e.g. into a $\sqrt{43}\times\sqrt{43}$-R$\pm$7.6° periodicity), together with possible inclusion of H, may further reduce the energy of the adatom-on-adlayer interface structure. (An example of energy reduction

by including H, albeit for a simple adatom model *without* an adlayer, can be seen by comparing the energy of the (6×6)-(6×6)-9Si(h3)-$9H_C$ with that of the (6×6)-(6×6)-9Si(h3) in Figure 3.11, for the range of H chemical potentials shown in the plot). Finally, one can consider effect of possible bonding between adatoms and the graphene on the energy. However, based on the discussion in Section 3.4.5, such effects are small (10 meV after excluding strains), and hence we do not consider them to be a significant factor for potentially changing the energy of the adatom-on-adlayer structure after graphene coverage.

We now consider the structure of the interface with graphene coverage. To avoid high strain of the graphene, while simultaneously maintaining the $\sqrt{43}\times\sqrt{43}$-R7.6° supercell for the Si adatoms, we consider structures with larger unit cells. Following discussion in Section 3.4.5, the graphene has a supercell of $\sqrt{57}\times\sqrt{57}$ in registry with 6×6 cells of the SiC. It is straightforward to see that $6\sqrt{43}\times6\sqrt{43}$-R7.6° SiC is commensurate with graphene overlayer. The overall symmetry for the entire structures (interface plus graphene) is then $6\sqrt{43}\times6\sqrt{43}$-R7.6°. The interface and graphene each follows a smaller periodicity of their own, i.e. $\sqrt{43}\times\sqrt{43}$-R7.6° SiC for the interface, and $(\sqrt{57}\times\sqrt{57})_G$ for the graphene where the subscript "G" clarifies that the cell is in terms of graphene lattice.

For the $\sqrt{43}\times\sqrt{43}$-R7.6° interface, we propose a model shown in Figure 3.12. In the figure we have shown four $\sqrt{43}$ unit cells, denoted by the green lines. Within each unit cell, we have 42 Si atoms in the adlayer (one less than a full monolayer with the missing one replaced by a H) and 14 Si adatoms on top of the adlayer. All the Si atoms in the adlayer are bonded by the Si adatoms on top through forming tetrahedron-like local structures. Although it is speculative, this model accounts for many features of the surface structure. First, it is consistent with the adatom-on-adlayer structure we have determined for the surface immediately prior to graphene formation. The arrangement of adatoms has been adapted to producing a $\sqrt{43}\times\sqrt{43}$-R7.6° periodicity while keeping some "footprint" of the surface before graphene formation, i.e. close to a 2×2 arrangement. The model also has the advantage that all the dangling bonds of the SiC C-

face and of the adlayer are passivated. Replacing one Si atom in the adlayer with H is in consideration that this arrangement is energetically more favorable than viable options such as keeping the Si atom (i.e. a full monolayer of Si as the adlayer). For instance, for an arrangement like Figure 3.12, if we keep the Si atom in the adlayer (i.e. replace the H in the figure with Si), that Si atom will have three dangling bonds. Even if these dangling bonds may be terminated H atoms, they will still be energetically less favorable than our current arrangement as we find, though our first principles computations, that the C—H bond is always much more stable than a Si—H bond.

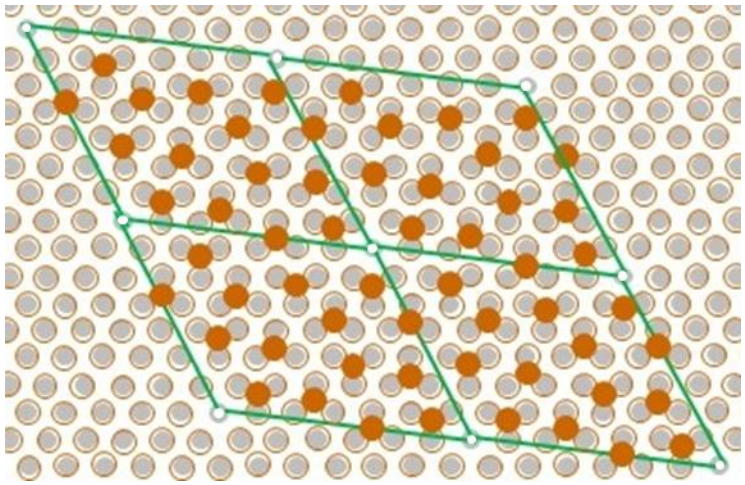

Figure 3.12 Model for the interface after graphene forms on C-face SiC (showing four unit cells)

Proposed model for the interface structure after graphene forms on the C-face of SiC. For clarity, we have shown four unit cells of $\sqrt{43}\times\sqrt{43}$-R7.6°, denoted by the green lines. Gray filled circles represent C atoms of the SiC bulk surface. Open orange circles on top of the gray dots represent Si atoms in the adlayer. There are 42 such atoms in a $\sqrt{43}\times\sqrt{43}$ unit cell. For the one C atom of the SiC bulk surface that is not bonded to a Si atom, it is bonded (terminated) by a H atom (white dots at the corners of the unit cells shown). The orange filled circles are Si adatoms on top of the Si adlayer. There are 14 such adatoms in a unit cell, each bonded to three Si atoms in the underlying adlayer.

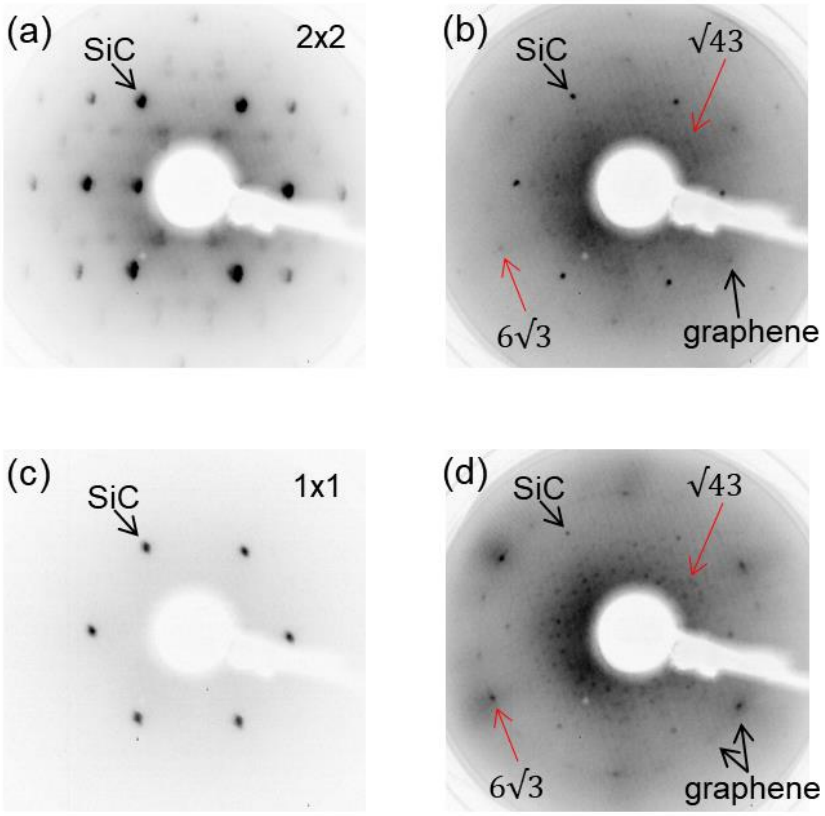

Figure 3.13 Introducing additional hydrogen

LEED patterns of C-face SiC surface when additional hydrogen is introduced (through external hydrogen). All are heated in 5×10^{-5} Torr disilane for 5 min with (a) hydrogen pressure $p(H_2) = 1\times10^{-4}$ Torr, heating temperature T = 1270 ℃, acquired at 146 eV; (b) $p(H_2) = 1\times10^{-4}$ Torr, T = 1295 ℃, acquired at 116 eV; (c) $p(H_2) = 2\times10^{-3}$ Torr, T = 1210 ℃, acquired at 140 eV; (d) $p(H_2) = 2\times10^{-3}$ Torr, T = 1290 ℃, acquired at 100 eV.

The first-principles results in Figure 3.7 and Figure 3.11 indicate that for enough high chemical potential of H, a (1×1)-H interface structure is predicted. To experimentally explore these predictions, we have performed additional work in which we maintain a fixed disilane partial pressure of 5×10^{-5} Torr but we introduce additional H_2 (i.e. through a second leak valve). We do indeed obtain 1×1 LEED patterns from such surfaces: when the partial pressure of the introduced H is less than ~10^{-4} Torr, then at temperatures below that at which graphene forms, 2×2 LEED patterns (identical to those without introducing H_2, i.e. with disilane only) are obtained. However, when we increase

the introduced H_2 partial pressure to 10^{-3} Torr, we predominantly observe 1×1 patterns (Figure 3.13(c)). We believe that this 1×1 pattern arising simply from the (1×1)-H structure, i.e. the H-terminated C-face surface.

Starting from these 1×1 surfaces obtained with the additional H_2, we have heated the samples to higher temperature to form graphene. We again observe $\sqrt{43}$ patterns, i.e. similar to those produced when no external H_2 is introduced. But we note that, as the H2 pressure increased, intensity of the $6\sqrt{3}$ diffraction spots increased significantly (Figure 3.13(b) and (d)), indicating the lowest-energy structure $(6\sqrt{3}\times 6\sqrt{3})$-(1×1)-H at high H chemical potential (Figure 3.11) has been obtained.

Finally, we discuss the difference between our C-face samples grown in the disilane environment and C-face monolayer graphene samples reported by de Heer and co-workers.[71] Their samples produce LEED patterns with sharp 1×1 graphene spots positioned at $30°$ relative to directions of primary (1,0) SiC spots. Careful inspection of their pattern reveals additional, faint spots at $6\sqrt{3}\times 6\sqrt{3}$-R30° positions, i.e. similar to what occurs for the Si-face. In contrast, LEED for our C-face samples reveal the $\sqrt{43}$ pattern, having diffraction intensity most pronounced at about $\pm 7°$ with respect to the primary (1,0) directions.[66] The differing results surely arise in part from the respective growth methods, since the confinement-controlled sublimation method of de Heer and coworkers[71] is quite different than the disilane exposure (in an open vacuum chamber) employed in our work. However it is also important to note that these nearly 1×1 graphene layers of de Heer et al.,[71] as also observed by Camara et al.,[102] do not occur homogeneously over the surface. Rather, they seem to form near specific step bunches and/or terraces on the surface. Thus, we suggest that these high-quality C-face graphene layers may arise from inhomogeneous nucleation on the surface, which would be quite different than for our work in which the graphene appears to be homogeneously nucleated.

3.6 Summary

In summary, we have studied the graphene formation on the C-face of SiC in a disilane environment. The surface structures prior to graphene formation are found to consist of Si adatoms on a Si adlayer. Specifically, the 2×2 phase contains a Si monolayer with a Si adatom on top (at t4 site). The 4×4 diffraction patterns arise from different domains of (4×4)-11Si, which has three Si adatoms sitting on top of a Si monolayer (one at h3 site, two at t4 sites). For the $\sqrt{43}\times\sqrt{43}$-R7.6° LEED pattern observed after graphene formation, we propose a structure similar to those prior to graphene formation, i.e. Si-rich adatom-on-adlayer structure, but with rearrangement of the adatoms such that they have the $\sqrt{43}$ periodicity. From first-principles theory and strain argument, we find that the 8×8 graphene, previously suggested as a closest match to $\sqrt{43}\times\sqrt{43}$-R$\pm$7.6° SiC, cannot fit the $\sqrt{43}$ cell without inducing significant strain in the graphene. Re-examination of the diffraction pattern reveals that the graphene diffraction spots are not located at a radius (magnitude of wavevector) predicted by a $\sqrt{43}\times\sqrt{43}$-R$\pm$7.6° cell. By looking at other fits between graphene and SiC, we find that $\sqrt{57}\times\sqrt{57}$-R6.5° graphene and 6×6 SiC is a good (low-strain) fit. This fit also explains the observed graphene diffraction spots in the LEED pattern. The overall symmetry of the entire surface (interface plus graphene) is then $6\sqrt{43}\times6\sqrt{43}-R7.6°$, with the interface and graphene each follows a smaller periodicity of their own.

4 Characterization of Two-dimensional Materials with LEED and LEEM

In this chapter, we present experimental results of characterizing two-dimensional (2D) materials using the methods of LEED and LEEM, as introduced in the Experimental Methods section. The samples we have worked on cover a broad range of 2D materials, from graphene formed under various conditions to diverse kinds of transition metal dichalcogenides (TMDs). Some of these samples are ones that we prepared (mostly graphene), while others were grown by our collaborators (mostly TMDs). The LEED is employed as a routine, *in-situ* apparatus for checking crystallinity of as-grown samples. The LEEM is used to obtain the morphological information of the surface, check crystallinity and orientation on the micrometer scale, determine the number of atomic 2D layers, and to extract work function differences between different domains on the surface. In the rest of this chapter, we present and discuss results for some representative samples.

4.1 Growth and Characterization of Quasi Freestanding Epitaxial Graphene

Epitaxial graphene formed on the Si-face of SiC has a well-known $6\sqrt{3}\times6\sqrt{3}$-R30° interface structure.[59] This interface is found to be a corrugated graphene-like layer (also known as the "buffer layer") that is partially bonded to the Si atoms of the substrate,[59] in contrast with a pristine graphene. The buffer layer is a poor conductor (with band gap of ~0.1 eV) because of its covalent bonding to the substrate. The term "epitaxial graphene" refers to carbon layers *on top* of the buffer layer, forming a true hexagonal arrangement with only van der Waals bonding to the buffer layer below. Because of charge transfer from the interface density of states associated with the buffer layer and the SiC surface,[114] the carrier concentration is epitaxial graphene is quite high. Due to the high carrier

concentration, the carrier mobility of the epitaxial graphene is much lower than that of suspended graphene produced from mechanical exfoliation (3000 vs 200000 $cm^2V^{-1}s^{-1}$).[103,104,105] One way to address the problem is through hydrogen intercalation.[57] After graphene is formed on the SiC(0001) surface, we can anneal the sample in a hydrogen flux at moderately high temperature (750 – 1000 ℃). The H atoms decouple the buffer layer from the underlying substrate by breaking the Si-C bonds between them. The decoupled buffer layer is known as quasi freestanding epitaxial graphene (QFEG) and becomes highly conducting. Additionally, the H atoms saturate the Si dangling bonds on the surface.[106] As a result, the charge transfer to epitaxial graphene is suppressed; and the carrier mobility of the hydrogenated sample increases drastically, from 3000 to >11000 $cm^2V^{-1}s^{-1}$.[104]

4.1.1 Sample preparation

In this work, we form graphene on the Si face of SiC using our graphene preparation chamber and then hydrogenate the sample to obtain the QFEG within the same chamber. Figure 4.1 is a schematic showing steps in our experiment. In detail, a chemically cleaned (by acetone and methanol) Si-face SiC sample is introduced to the preparation chamber (Figure 2.1), after which it is hydrogen etched at 1600 ℃ for 3 min under a hydrogen flux of 105 lpm. The hydrogen etching removes polishing damage from the SiC surface. After pumping out the hydrogen, the sample is heated in 1 atm Ar at 1350 ℃ for 15 min to form epitaxial graphene. The sample is then cooled down to room temperature and studied by the connected *in-situ* LEED, after which it is transferred back to the preparation chamber and heated at 950 ℃ for 30 min.

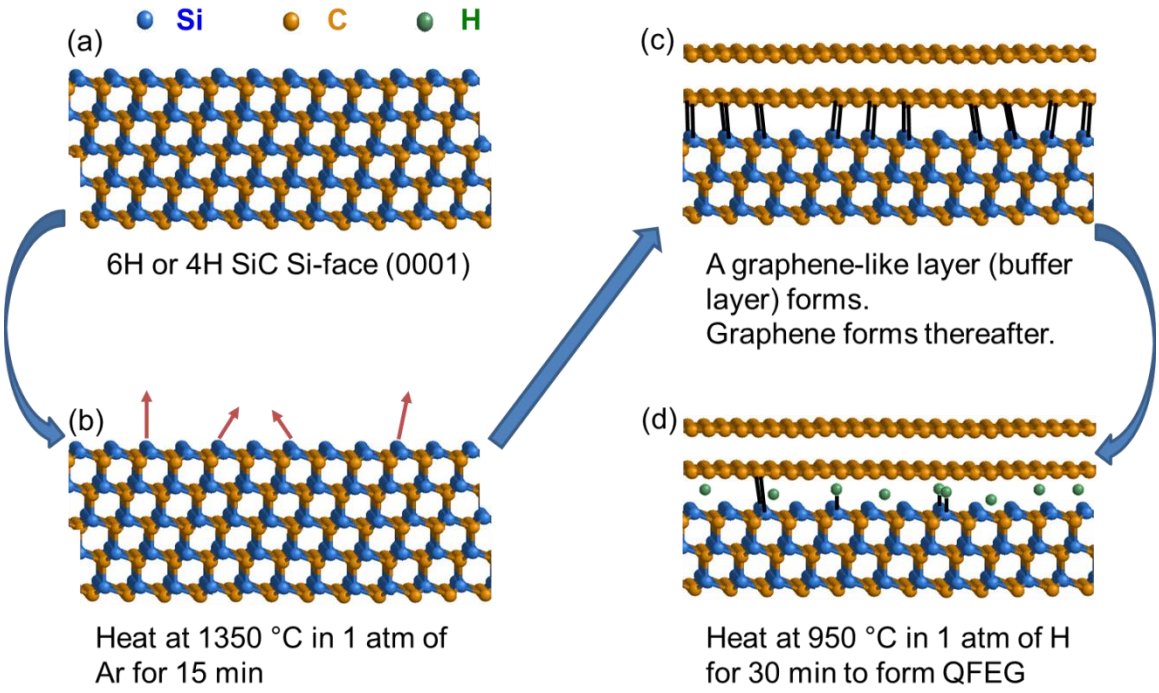

Figure 4.1 Schematic of QFEG formation process

Schematic showing steps and experimental conditions for forming the quasi freestanding epitaxial graphene (QFEG). (a) A chemically cleaned (by acetone and methanol) piece of Si-face SiC sample is introduced into the preparation chamber. (b) The sample is heated in 1 atm of Ar for 15 min at 1350 ℃. (c) The buffer layer forms and graphene forms thereafter on top during the heating. (d) After the heating, the sample is left to cool down to room temperature and Ar is pumped out of the preparation chamber. The sample is then heated in 1 atm of H for 30 min at 950 ℃ to form the QFEG.

4.1.2 LEED/LEEM measurements

Through *in-situ* LEED and *ex-situ* LEEM measurements, we characterize the surface before and after hydrogenation. Results from both the LEED and LEEM measurements are in full agreement with that reported in Refs 57,107. Figure 4.2 shows LEED patterns obtained for the sample before and after hydrogenation. From the figure, it is clear that most satellite diffraction spots that are characteristic of the $6\sqrt{3}\times6\sqrt{3}$-R30° interface structure are gone after hydrogenation. This is because, as already mentioned above, the buffer layer is decoupled from the underlying substrate by H atoms. It also confirms the

$6\sqrt{3}\times6\sqrt{3}$-R30° LEED pattern is a result of diffraction from the buffer layer (which is more complicated for the case of graphene formed on C-face of SiC, as discussed in detail in the previous chapter). The increased brightness of graphene diffraction spots is a result of an additional graphene layer, indicating the buffer layer has converted to (quasi freestanding) graphene.

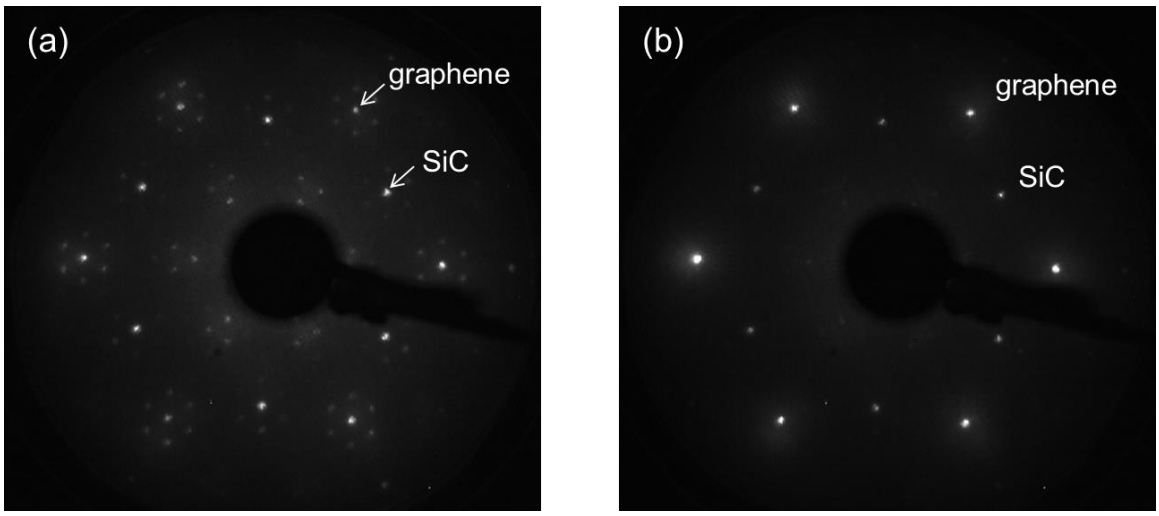

Figure 4.2 LEED patterns for a graphene sample before and after H intercalation.

LEED patterns for an epitaxial graphene sample before and after H intercalations, both acquired at 100 eV. (a) Before H intercalation, the diffraction pattern shows the characteristic satellite spots around the primary SiC spots and graphene spots, which corresponds to the $6\sqrt{3}\times6\sqrt{3}$-R30° buffer layer. (b) After H intercalation, most of the satellite diffraction spots are gone. The intensity of graphene spots relative to that of SiC has become much stronger. Both of these observations indicate that the buffer layer has been decoupled from the substrate and converts to quasi freestanding epitaxial graphene (QFEG).

We have also looked at the formed QFEG in the LEEM. Figure 4.3 shows the results for a typical area of the surface. The LEEM image in Figure 4.3(a) shows different domains on the surfaces, with typical domain size >5 μm. There domains corresponds to varying numbers of graphene layers formed, as indicated by the reflectivity spectra in Figure 4.3(b). Reflectivity minima close to the onset in the spectra (indicated by arrows)

are due to additional interlayer states introduced when the buffer layer is decoupled from the substrate, a signature of formation of the QFEG.[57,107]

From the reflectivity spectra, we can extract work function difference between different domains on the surface. We see that two layers (including the decoupled buffer layer) and three layers of graphene have similar work functions (difference in work function between sample surface and electron emitter in the LEEM of $\Delta W = 0.03$ eV). In contrast, the bare (decoupled) buffer layer has a very different work function ($\Delta W \approx 1.0$ eV). This indicates that the buffer layer, although decoupled from the substrate, is still quite different from the epitaxial graphene on top in terms of carrier concentrations.

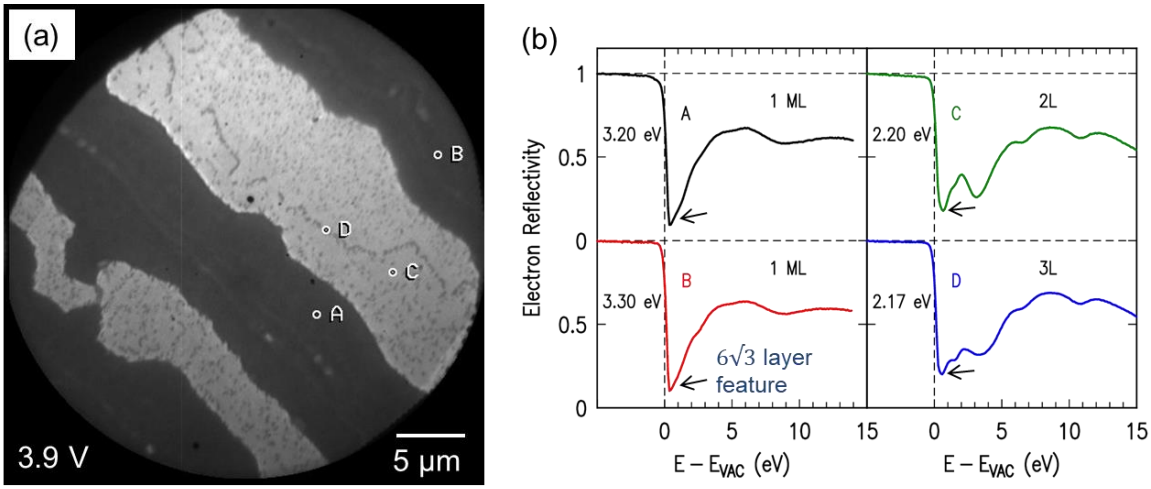

Figure 4.3 LEEM results for QFEG

LEEM results for a typical area of the QFEG sample surface. (a) LEEM image acquired at sample voltage of 3.9 V with 25 µm field of view. The image clearly shows different domains with sizes >5 µm. (b) Reflectivity spectra and extracted work function differences for points labeled in (a). The points are selected to be representative of different domains. The minimum close to the onset of the reflectivity spectra (indicated by arrows) is due to additional interlayer states between the buffer layer and the substrate, a signature that the buffer layer has been decoupled form the substrate and become QFEG.

4.1.3 Summary

In this experiment, we studied formation of QFEG by H intercalation of the SiC−C-buffer layer interface. LEED patterns acquired for the sample surface before and after H intercalation reveal that the buffer layer is decoupled from the substrate, converting to a new graphene layer (QFEG) after H passivates the SiC surface. LEEM/LEER measurements show reflectivity spectra characteristic of decoupled buffer layer. It is found that domains covered only by the buffer layer have a relatively large work function difference from those covered by additional graphene layers, indicating that the buffer layer, even after H intercalation, still differs from other graphene layers in carrier concentrations.

The formed QFEG is useful not only because of improved carrier mobility as mentioned, but also can be used as a good contact to other 2D materials such as tungsten diselenide (WSe_2), which we will discuss in the next section.

4.2 Tuning Electronic Transport in Tungsten Diselenide – Graphene heterostructures

This work is a collaborative work between the Robinson group at Penn State, our group here at CMU, and the Cho group at UT Dallas, published in *Nanoscale* (2016).[11] For the results presented in this section, Yu-Chuan Lin and Sara Eichfeld prepared the samples. Yu-Chuan Lin carried out AFM and electrical measurements. Sergio de la Barrera and Patrick Mende performed LEEM/LEER. The author (JL) proposed the band alignment models and computed the charge transfer and carrier densities, by combining LEEM and electrical measurement data.

In this work, we demonstrate that the carrier type of the graphene is a critical parameter in controlling the charge transport at the TMD/graphene interface. By controlling the doping type and concentration of epitaxial graphene (EG) from n- to p- via *in situ* hydrogen intercalation[57,107] during the tungsten diselenide (WSe_2) synthesis, we demonstrate the origins of ohmic behavior (i.e. close to linear response of current to the voltage applied) in TMD/graphene structures, and obtain low resistance ohmic

transport between a WSe_2 and graphene heterostructures. Two samples, monolayer WSe_2 on partially hydrogenated EG (WSe_2-EG_{PH}) and monolayer WSe_2 on fully hydrogenated EG (WSe_2-EG_{FH}), are studied in this work. Measurements by LEEM, LEER, and conductive atomic force microscopy (CAFM) show that EG_{FH} (p-type) is a better contact to WSe_2 in that ohmic behavior is observed for the WSe_2-EG_{FH} diode.

4.2.1 Sample Preparation

WSe_2 is synthesized on epitaxial graphene by metal-organic chemical vapor deposition (MOCVD), at different temperatures for the two samples, WSe_2-EG_{PH} and WSe_2-EG_{FH}. Figure 4.4(a) shows a schematic of the WSe_2-EG growth. In detail, epitaxial graphene is first formed on the Si face of 6H SiC at 1625 ℃ in 200 Torr Ar inside a confined heating chamber made of pure graphite. The SiC substrate is pre-etched by 700 Torr H2/Ar mixtures (500 sccm) to remove polishing damage on the surface. The precursors chosen for MOCVD synthesis of WSe_2 are tungsten hexacarbonyl ($W(CO)_6$) and dimethylselenium ($(CH_3)_2Se$), which provide the W and Se, respectively. In order to eliminate carbon contamination from the precursor, a 100% H_2 environment is utilized during the WSe_2 synthesis.[108] This necessity of 100% H_2 significantly modulates the chemical environment of graphene, in comparison with a dilute H_2 environment for WSe_2 growth. X-ray photoemission spectroscopy (XPS) performed for a WSe_2-EG sample prepared by this process (MOCVD, 100% H_2, 800 ℃) and for a WSe_2-EG sample grown via power vaporization (PV) using 5% H_2 at 900 ℃ shows that, the C 1s core level of the sample via MOCVD shifts towards a lower binding energy by 0.4 eV compared to that of the sample via PV. This shift of C 1s core level in EG has been associated with hydrogen intercalation.[61,109] Evident from the XPS, the 100% H_2 environment leads to complete hydrogen interaction at the EG/SiC interface, fully decoupling the C-rich buffer layer at 900 ℃.

The growth of WSe_2 on EG proceeds by vdW epitaxy, mediating the lattice mismatch between WSe_2 and graphene.[110] WSe_2 atomic layers are grown via MOCVD on EG-SiC substrates employing H_2 as carrier gas[108] at 800 ℃ and 930 ℃ to study how hydrogen intercalation impacts the electrical transport between graphene and WSe_2, for different growth temperatures (Figure 4.4(b)). After 30 min growth, the as-grown atomic

layers are confirmed to be monolayer, 1 μm wide and 0.7 nm thick with atomic force microscopy (AFM) (Figure 4.4(c)).

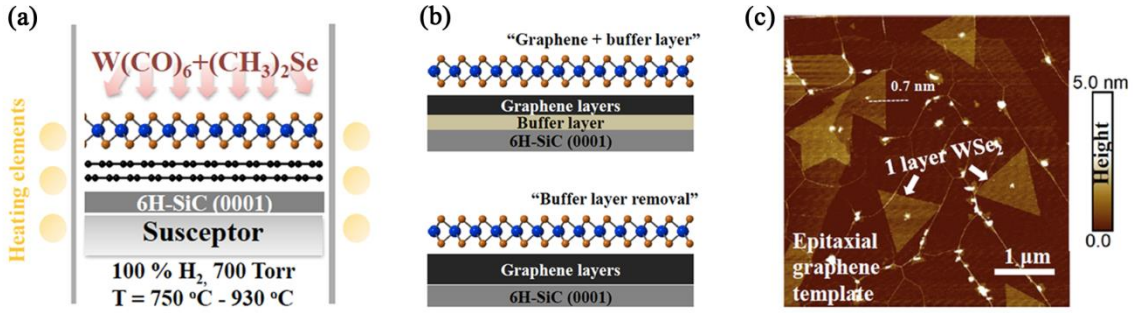

Figure 4.4 WSe_2-EG synthesized via MOCVD

WSe_2-EG synthesized via metal-organic chemical vapor deposition (MOCVD). (a) Illustration of MOCVD process of monolayer WSe_2 on EG-SiC, showing precursors for W ($W(CO)_6$) and Se ($(CH_3)_2Se$), and growth conditions (100% H_2, 700 Torr, heating temperature 750 – 930 ℃). (b) When the process of WSe_2 synthesis is carried out at a lower temperature the buffer layer decoupling is incomplete (top). A higher synthesis temperature can effectively convert the buffer layer into graphene via hydrogen intercalation (bottom). (c) AFM image of grown WSe_2-EG heterostructures. Triangular domains are mostly monolayer WSe_2, indicated by height measurements (0.7 nm).

4.2.2 LEEM/LEER Measurements and Analysis

In order to locally study the surface and electronic structure of the WSe_2-EG samples, LEEM with electron energies of 0 – 20 eV is employed. In addition, low-energy electron reflectivity (LEER) spectra provides an accurate means of determining the number of graphene layers, identifying WSe_2 and graphene domains, and extracting the work function differences between domains.[12,49,51] The LEEM images of WSe_2-EG_{PH} from 800 ℃ WSe_2 growth show triangular islands of WSe_2 with a characteristic size of 1 μm, nucleating preferentially near SiC step edge on the EG surface (Figure 4.5(a)). The graphene is found predominantly in monolayer + buffer layer form, but small bi- and tri-layer graphene domain are also found on the surface. This indicates that the buffer layer

is nearly intact as as-grown EG, or only a negligible portion of it has been decoupled during the 800 ℃ WSe_2 growth.

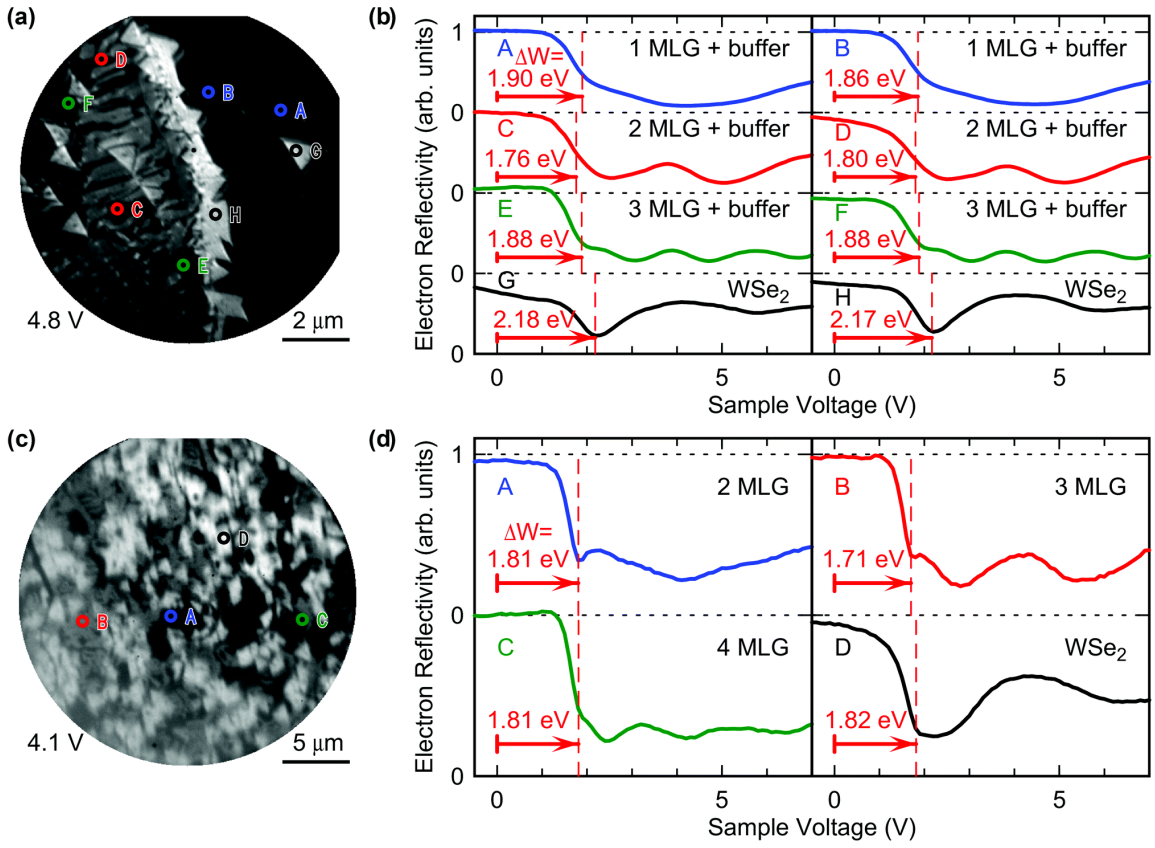

Figure 4.5 LEEM/LEER measurements of WSe_2-EG_{PH} and WSe_2-EG_{FH}

LEEM/LEER measurements of WSe_2-EG_{PH} (WSe_2 grown at 800 ℃) and WSe_2-EG_{FH} (WSe_2 grown at 930 ℃). (a) LEEM image of WSe_2-EG_{PH} acquired at sample voltage of 4.8 V. Labeled points indicate locations of reflectivity spectra in (b), which are used to identify the materials in the image. Bright triangles are WSe_2 islands, dark regions are mono- to multi-layer graphene on carbon-rich buffer layer. The values specified to the left of each spectrum quantify the electrostatic potential and hence the vacuum level variation of the surface. (c) LEEM image of WSe_2-EG_{FH} at 4.1 V. (d) Reflectivity spectra of the points labeled in (c); characteristic of a decoupled buffer layer.

The LEER spectra show characteristic oscillations for graphene and WSe_2 for the respective regions of the surface and allow material identification in the LEEM images, as shown in Figure 4.5(b) for the WSe_2-EG_{PH} sample.[111] Such LEER curves also permit determination of the work function differences between varying domains on the surface, as discussed in the Section 2.3.4 of the Experimental Methods chapter. A difference of $\Delta W \approx 0.31 \pm 0.03$ eV is found between the work functions of monolayer graphene and WSe_2 (uncertainty from a combination of uncertainties in the measurement, analysis, and variations of the sample surface). It should be noted that this observed work function difference between WSe_2 in contact with underlying graphene (G in Figure 4.5(a)) and a bare graphene region without WSe_2 covering the top (A or B in Figure 4.5(a)). The presence of interface dipoles and a change in local work function implies charge transfer between the WSe_2 and the graphene below. Consistent with this interpretation, it is noted that the LEER curves measured on the WSe_2 islands from WSe_2-EG_{PH} (Figure 4.5(b)) display a broad, sloping feature for low voltages (in the range of "mirror mode" discussed in Section 2.3.4). This feature also indicates the presence of charge, or more specifically, electric dipoles on the edges of the triangular crystals which displace the incident and reflected electron beam during measurement, thus reducing the reflected intensity.[12]

The WSe_2-EG_{FH} from the 930 ℃ WSe_2 growth shows similar 1 μm triangle islands of WSe_2 on an EG surface in LEEM (Figure 4.5(c)). However, the sloping features in reflectivity associated with charge accumulations are much smaller than in WSe_2-EG_{PH}. In addition, the extracted work function differences between uncovered bilayer graphene and WSe_2 (in contact) in the WSe_2-EG_{FH} are negligible (0.03 ± 0.03 eV) compared to the WSe_2-EG_{PH} sample, suggesting limited charge transfer between WSe_2 and EG (Figure 4.5(d)). These observations, along with the presence of an additional, small minimum valley near 0 eV in the reflectivity spectra, are attributed to full hydrogenation of the SiC surface, which passivates bonds between the carbon-rich buffer layer and the underlying SiC. This has the effect of releasing the buffer layer and increasing the count of graphene layers in the hydrogenated regions by 1.[57] Together with the Raman spectroscopy measurements (not shown), we conclude the WSe_2 growth at high temperatures (>900 ℃) leads to fully hydrogenated EG (EG_{FH}) compared to those partially hydrogenated EG (EG_{PH}) formed at lower temperatures (750 – 800 ℃).

Concurrently, the electrical properties of the WSe_2-EG interface appear to have changed significantly.

4.2.3 Conductive AFM I–V characteristics and band alignment model

The hydrogenation process is known to have a significant impact on the electrical properties of graphene on SiC. EG residing on top of the buffer layer on 6H-SiC (0001) is n-type doped[109,112,113] due to the combination of bulk and interface donor states[114,115] and has a Fermi energy ≈0.45 eV above the Dirac point.[114] In contrast, QFEG is known to be p-type doped.[57,114] This change has been explained by the presence of the spontaneous polarization of the hexagonal 6H-SiC substrate, which lowers the Fermi energy to a position 0.28 – 0.30 eV below the Dirac point for complete hydrogenation.[114,116] This modification in the doping of graphene can thereby influence the electrical transport properties across the WSe_2–graphene interface on SiC. In order to elucidate the transport properties, vertical current versus voltage (I–V) measurements were performed on the 800 ℃ and 930 ℃ WSe_2 growth (labeled as WSe_2–EG_{PH} and WSe_2–EG_{FH}, respectively) in Conductive AFM (CAFM).

A CAFM tip with PtIr coating, and the graphene, serves as source and drain, respectively. While the WSe_2–EG_{PH} diode exhibits an I–V with turn-on current at bias of $\geq$ 1 V; however, the WSe_2–EG_{FH} diode turns on near zero bias (Figure 4.6(a)). The main component of the CAFM current near zero bias for WSe_2–EG_{PH} is due to tunneling from the CAFM tip to graphene through the WSe_2 gap. On the other hand, For WSe_2–EG_{FH}, the WSe_2 layer acts as a short between the CAFM tip and the EG_{FH} (Figure 4.6(b)).

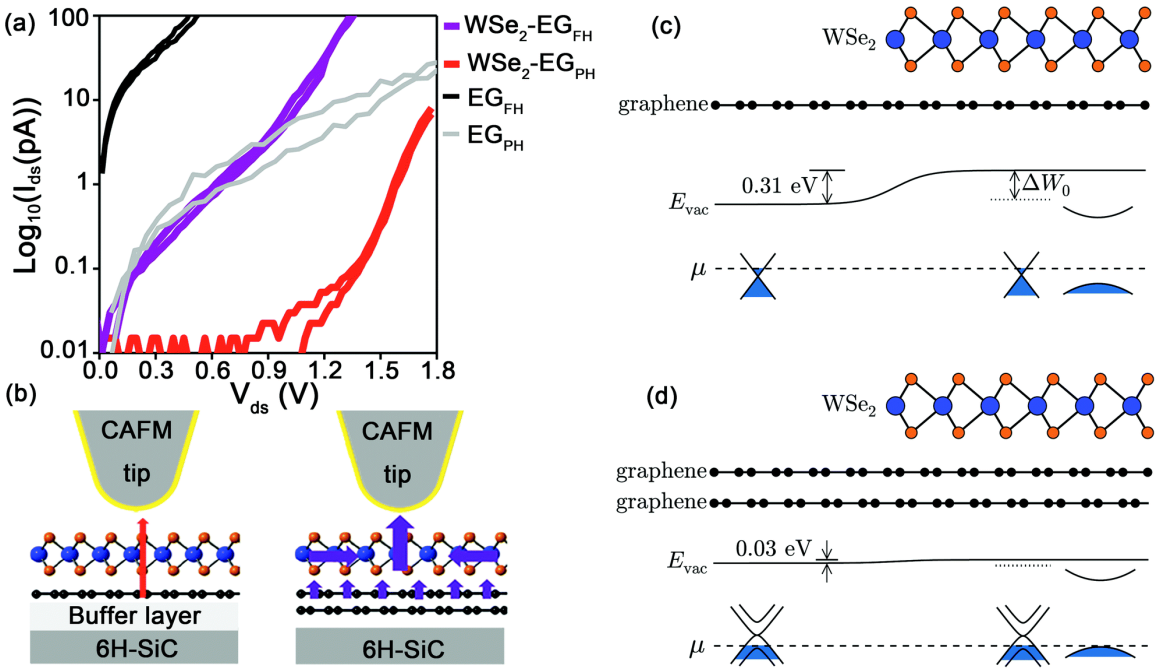

Figure 4.6 CAFM I-V measurements and Band alignments

(a) Conductive AFM (CAFM) I-V measurements of WSe_2-EG_{PH} and WSe_2-EG_{FH}, with additional results for EG_{PH} and EG_{FH} for reference. Band alignment and vacuum energy diagrams for the two heterostructures, WSe_2–EG_{PH} (c) and WSe_2–EG_{FH} (d), at zero bias, showing variations of vacuum energy of the surface due to partial WSe_2 coverage. The band alignment diagram for WSe_2-EG_{PH} (c) shows that the Fermi level in equilibrium is inside the bandgap, leading to a relatively high Schottky barrier, while for WSe_2–EG_{FH} it shows that the Fermi level of the heterostructure is close to valence band maximum of WSe_2, resulting in an ohmic contact. The values indicated (0.31 eV and 0.03 eV) are work function differences measurement from LEEM (Figure 4.5). (b) Illustration of electronic transport in WSe_2-EG_{PH} and WSe_2-EG_{FH} close to zero bias. In the former case, transport is limited by the high Schottky barrier in WSe_2–EG_{PH} while this is not the case for WSe_2–EG_{FH}.

Our LEEM measurements and analysis above indicate a work function difference of 0.31 eV between the WSe_2 (in contact with EG_{PH}) and the uncovered monolayer EG_{PH}, while the work function difference between the WSe_2 (in contact with EG_{FH}) and the uncovered bilayer EG_{FH} is near zero. The measured work function difference is a combination effect of intrinsic interface dipole and extrinsic interface dipole. The

extrinsic dipole is due to doping caused by charge transfer between WSe_2 and graphene. The intrinsic dipole results from redistribution of charge within the WSe_2 or graphene itself upon contact. In other words, it is the difference between vacuum level of undoped WSe_2 and that of undoped graphene when they are put in contact. Density functional theory (DFT) calculations of this intrinsic dipole are performed using the Vienna ab initio simulation package (VASP)[81] with the projector-augmented wave (PAW) method.[117] The local density approximation (LDA)[118] is used to describe the exchange–correlation functional with the partial core correction included. More DFT calculation details can be found in the Supplementary Information of Ref. 11. The computed vacuum energy level above WSe_2 is 0.17 eV higher than that above graphene, indicating an (intrinsic) dipole from graphene towards the WSe_2.

Using this intrinsic dipole, along with the measured work function differences, we propose a model in which the WSe_2 has some unintentional p-type doping, and transfer of charge between the EG_{PH} or EG_{FH} and the WSe_2 (combined with the intrinsic dipole) produces the observed variation in work function. With knowledge of the doping density of EG_{PH} and EG_{FH} ($(4 \pm 1) \times 10^{12}$ cm^{-2} n-type and $(1.5 \pm 0.2) \times 10^{13}$ cm^{-2} p-type, respectively, from our previous electrical studies on EG_{PH} and EG_{FH}),[109,119] and using reported values of electron affinities of monolayer graphene (4.57 eV) and bilayer graphene (4.71 eV),[120] we compute the transfer of charge between the WSe_2 and the EG_{PH} or EG_{FH}. This charge transfer, for a given (unintentional) doping density of the WSe_2, yields theoretical values for the work function differences; the doping density is determined by matching these differences to experiment. Our model is illustrated in Figure 4.6(c) and (d). The dependence of the results on the electron affinities of graphene is discussed in the Appendix at the end of this section.

For the charge transfer computation, we employ the standard linear band structure around the K point for the monolayer graphene from EG_{PH}, and hyperbolic bands near the band extrema for bilayer graphene from EG_{FH} and for WSe_2 around K points, based on tight-binding models.[121,122] The method to compute the electrostatics is similar to that described by Li et al.[126] Figure 4.6(c) and (d) show band diagrams of the WSe_2–EG_{PH} and WSe_2–EG_{FH} surfaces, which are graphene partially covered by WSe_2. Both the intrinsic

interface dipole and the charge transfer are taken into account and equilibrium is reached when the Fermi levels are aligned. The difference between the vacuum energy of WSe_2 (in contact with graphene) and the underlying graphene (e.g. ΔW_0 in Figure 4.6(c)) is thus a sum of the intrinsic interface dipole effect and the charge transfer effect.

In order to match the theoretical work function difference between the WSe_2 (in contact) and the uncovered graphene with the experimental values (0.31 eV and 0.03 eV for WSe_2–EG_{PH} and WSe_2–EG_{FH} respectively), we employ an unintentional p-type doping of 1.3×10^{12} cm^{-2} for the WSe_2 before charge transfer between the WSe_2 and the underlying graphene. When the WSe_2 is put in contact with EG_{PH} (n-type), electrons transfer from the EG_{PH} to the WSe_2, leading to nearly complete compensation of the p-type doping in the WSe_2 and a negligible carrier density in the WSe_2. The Fermi level ends up well inside the bandgap of the WSe_2 and near the charge neutrality point in the graphene (Figure 4.6(c)). For the case of the WSe_2 in contact with the EG_{FH} (p-type), electrons transfer from the WSe_2 to the EG_{FH}, making the WSe_2 more p-type (carrier density 2.9×10^{12} cm^{-2}). The resulting Fermi level of the WSe_2–EG_{FH} remains near the top of the valence band of its WSe_2. In other words, the WSe_2 on the EG_{PH} forms a Schottky barrier (i.e. relatively low conductivity), whereas the WSe_2 on the EG_{FH} forms as ohmic contact (i.e. high conductivity), and leading to a $\sim 10^3\times$ increase in current drive (Figure 4.6(a)).

An additional output of our charge transfer computations is the sum of the bandgap plus electron affinity of the WSe_2, $X_{WSe_2} + E_g$ (only the sum enters, since the electron density in the WSe_2 conduction band is negligible). In order to match the observed work function variations, we deduce an unintentional doping density in the WSe_2 of 1.3×10^{12} cm^{-2}, and the value of $X_{WSe_2} + E_g$ is determined to be 5.1 eV. This value is consistent with a recently reported electron affinity of ~3.1 eV for WSe_2 using first-principles GW calculation,[123] together with a bandgap of ~2 eV, which is in agreement with several recently reported experimental values.[124,125] Variation of our deduced values due to uncertainty in the other parameters in the problem is discussed in the Appendix.

4.2.4 Summary

By varying the temperatures for growth of WSe_2 on EG in a pure H_2 environment, the transport across WSe_2-graphene heterostructures is controllable. The investigation combing LEEM/LEER, Raman spectroscopy, and electrical measurements on the heterostructures confirmed the transport across the interface is controlled by the doping the EG, which in turn is tuned by hydrogenation of the SiC-buffer layer interface. The band alignment diagrams of two different heterostructures, WSe_2-EG_{PH} and WSe_2-EG_{FH} were constructed with the measured work function differences between the WSe_2 and the graphene from LEER. Taking into account their intrinsic interface dipoles and charge transfer, the diagrams show the presence of the Schottky barrier in WSe_2-EG_{PH} and a reduced barrier in WSe_2-EG_{FH}, which are in agreement with measured I-V characteristics.

The work described here is foundational for understanding vertical transport in graphene-based 2D heterostructures, demonstrating that doping of the graphene plays a critical role in these novel structures. Epitaxial graphene is unique because it can be made n- or p-type based on the TMD growth conditions, allowing one to readily engineer the transport between graphene and n- or p-type TMDs with a truly pristine interface.

Appendix

Computation of WSe_2 doping density and charge densities, and dependence on parameters

For the computation of charge transfer and band alignment, we take the doping densities of EG_{PH} and EG_{FH} from our experimental values, as discussed in the main text. Parameters in the computation are the electron affinities for monolayer and bilayer graphene, with nominal values of 4.57 eV and 4.71 eV, respectively, as known from prior experiments.[10] We take the sum of the electron affinity plus band gap of the WSe_2, $X_{WSe_2} + E_g$, to be an unknown in the computation, since a value for this sum is not accurately known from prior work (only the sum is considered here since the electron occupation in the conduction band of the WSe_2 is negligible). A second unknown is the unintentional doping density of WSe_2. Then, using the two measured work function differences for WSe_2 on both EG_{PH} and EG_{FH} compared to the bare EG_{PH} and EG_{FH}, we

can determine values for the two unknown parameters. The carrier densities for the WSe_2 on both EG_{PH} and EG_{FH} after charge transfer are then a byproduct of the computation. Table 2 shows dependence of these quantities on the input parameter values. In all cases, the carrier densities of WSe_2 in WSe_2-EG_{PH} are very much greater than those of WSe_2 in WSe_2–EG_{FH}, consistent with the observed differences in the CAFM I-V results.

Table 2 Computed dependence of valence band maximum and carrier densities on electron affinities of graphene

Computed dependence of electron affinity plus bandgap of WSe_2 ($X_{WSe_2} + E_g$), unintentional doping of WSe_2 (N_A), carrier density of WSe_2 after charge transfer between WSe_2 and EG_{PH} ($N_{C,WSe_2-EG_{PH}}$), and carrier density of WSe_2 after charge transfer between WSe_2 and EG_{FH} ($N_{C,WSe_2-EG_{FH}}$) on electron affinities of EG_{PH} ($X_{EG_{PH}}$) and EG_{FH} ($X_{EG_{FH}}$), respectively. An error range of ± 0.1eV for the input parameters is considered.

$X_{EG_{PH}}$	$X_{EG_{FH}}$	$X_{WSe_2} + E_g$	N_A	$N_{C,WSe_2-EG_{PH}}$	$N_{C,WSe_2-EG_{FH}}$
4.57	4.71	5.09	1.3×10^{12}	4.1×10^{5}	2.9×10^{12}
4.47	4.71	5.09	1.3×10^{12}	0.9×10^{4}	2.9×10^{12}
4.67	4.71	5.09	1.3×10^{12}	2.0×10^{7}	2.9×10^{12}
4.57	4.61	4.99	1.3×10^{12}	2.0×10^{7}	2.9×10^{12}
4.57	4.81	5.19	1.3×10^{12}	0.9×10^{4}	2.9×10^{12}

We note that the doping density values in Table 2 are all the same, reflecting a tight constraint on this value. This constraint arises from charge transfer between the WSe_2 and the EG_{PH}. As pictured in Figure 4.7(a) and (b), since the Fermi energies of the EG_{PH} and WSe_2 are relatively far apart prior to charge transfer, and hence the Fermi energy of the WSe_2 ends up well within its band gap after the transfer, then the p-type doping density in the WSe_2 is directly determined by the doping density of the EG together with the difference between the electron affinity of the EG_{PH} and the $X_{WSe_2} + E_g$ value of the WSe_2. The resulting carrier densities for the WSe_2 on EG_{PH} are negligible, again since the resulting WSe_2 Fermi energy is well within the gap. On the other hand, for the WSe_2 on EG_{FH}, their Fermi energies are relatively close prior to charge transfer, as

pictured in Figure 4.7(c) and (d). The resulting Fermi energy for the WSe_2 on EG_{FH} ends up near or within the valence band even after the charge transfer, with concomitant large carrier density, and the value of the WSe_2 doping density is not so tightly constrained in this part of the problem.

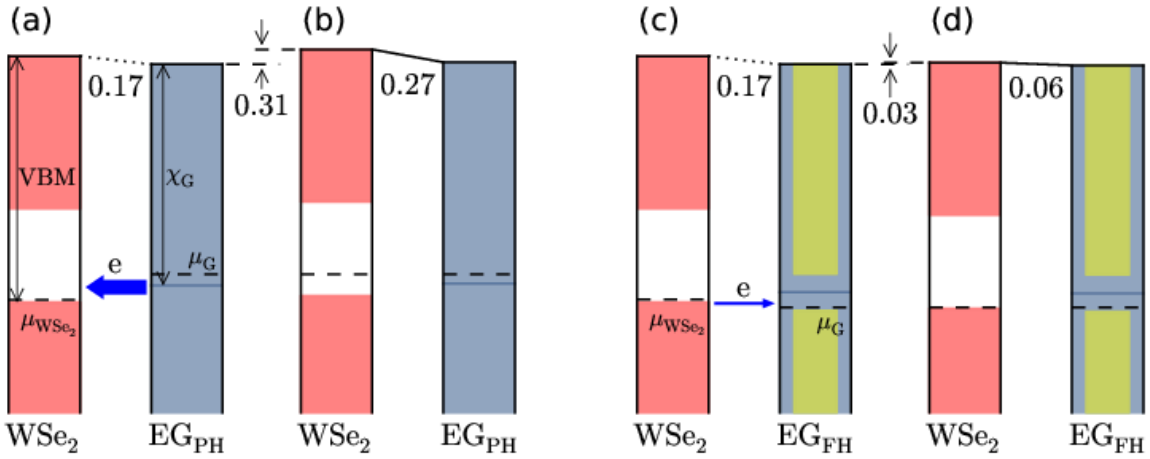

Figure 4.7 Band alignment of WSe_2–EG before and after contact

Band alignment of WSe_2 and EG_{PH} (a) before charge transfer (including computed intrinsic dipole 0.17 eV), and (b) after charge transfer. Band alignment of WSe_2 and EG_{FH} (c) before charge transfer (including the intrinsic dipole), and (d) after charge transfer. Monolayer and bilayer graphene models are employed for EG_{PH} and EG_{FH} respectively, based on LEEM observations. Green shades in (c) and (d) represent conduction/valence subbands of bilayer graphene. The numerical values show various vacuum level differences, in units of eV.

We have also considered the effect on the computed carrier densities of variation in the EG_{PH} and EG_{FH} doping density values, as well as variation of the measured work functions differences within their experimental error ranges. Doping densities of $(4 \pm 1) \times 10^{12}$ cm^{-2} for EG_{PH} and $(1.5 \pm 0.2) \times 10^{13}$ cm^{-2} for EG_{FH} are typical measured in our samples. Considering the variations of these doping densities, the carrier density of WSe_2 on EG_{FH} after charge transfer is computed to range from $2.5 - 3.0 \times 10^{12}$ cm^{-2} while the carrier density of WSe_2 on EG_{PH} after transfer is always less than 10^7 cm^{-2}, i.e. its Fermi is well within the bandgap. For the measured error ranges (±0.03 eV) on the work function differences, performing computations at the bounds of these values produces

carrier densities in the WSe_2 on EG_{FH} compared to WSe_2 on EG_{PH} that continue to differ by more than a factor of 10^4, for all cases.

4.3 Properties of synthetic epitaxial graphene/molybdenum disulfide lateral heterostructures

The samples we study in this section are synthesized molybdenum disulfide (MoS_2) films that may or may not be contacted by epitaxial graphene (EG) on the sides. This is a collaborative work between the Robinson group at Penn State, the Fullerton group at University of Pittsburgh, and our group here at CMU. The main conclusion is that when epitaxial graphene is used to as a contact to MoS_2 (forming a MoS_2–EG heterostructure), both the contact resistance and sheet resistance is reduced significantly compared to MoS_2 contacted directly by conventional titanium/gold (Ti/Au). Part of the results presented here is published in *Carbon* (2017).[10] For the results presented in this section, Shruti Subramanian prepared the samples and did the cross-sectional TEM measurements. The author (JL) carried out the LEEM/LEER measurements and band alignment analysis.

In this section, we focus on LEEM measurements on these samples, with a brief introduction to the sample preparation process. The LEEM results reveal crystallinity and grain size information of grown MoS_2. From the reflectivity spectra (LEER), work function variations between different domains on the surface are extracted, from which band alignments may be deduced. The band alignments results are in agreement with electrical transport measurements done by the Fullerton group at Univ. Pittsburgh.

4.3.1 Sample preparation

The samples are prepared by the Robinson group at Penn State. Here we describe the process briefly. The EG is formed via Si sublimation from the Si-face of 6H SiC in a confined furnace made of graphite. The SiC is first cleaned using acetone and isopropyl alcohol, and subsequently annealed in 10% hydrogen (balance argon) at 1500 ℃ for 30 min to remove polishing damage. The hydrogen is then pumped out of the system, and the temperature is increased to 1800 ℃ for 10 min at 500 Torr to form graphene.

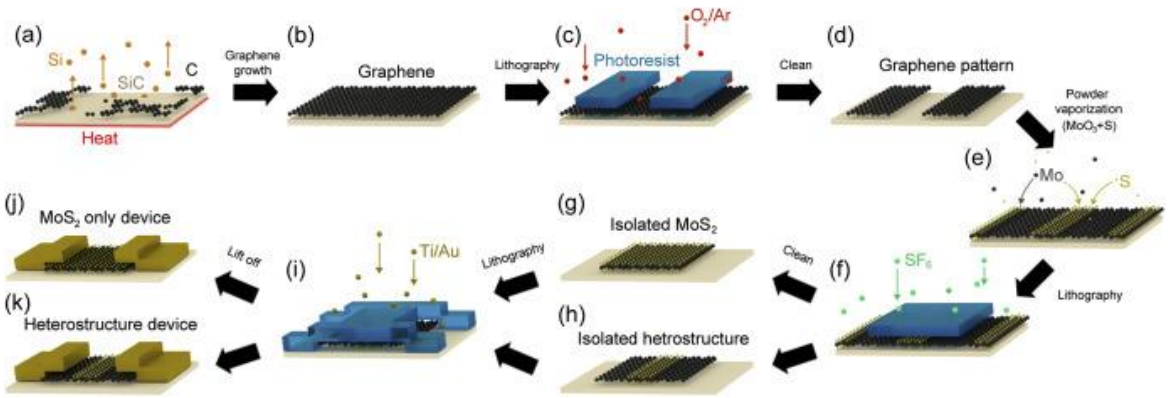

Figure 4.8 MoS_2 device fabrication process

Illustration of fabrication process for MoS_2 devices with a MoS_2-only channel (j) or with a MoS_2-EG channel (k). From Ref. 10.

The formed graphene is then patterned on the substrate using standard ultraviolet (UV) photolithography. A pattern consisting of varied channel spacing is produced using a photoresist. A subsequent mixture of oxygen and argon is used for react ion etch to remove the EG outside of the patterns, leaving behind a series of periodically spaced graphene rectangles of fixed width, that ultimately constitute the contacts to the MoS_2 channel. In addition to removing EG, this etch recipe also oxides the SiC substrate based on TEM and x-ray photoelectron spectroscopy (XPS). The lithographic mask is designed so that EG is completely removed in specific regions on the SiC substrate to provide areas where MoS_2-only (without the graphene contacts) is grown.

Following graphene growth and patterning, MoS_2 is synthesized using powder vaporization. The patterned graphene substrate is placed on top of a rectangular crucible containing 2-3 mg of molybdenum trioxide (MoO_3) powder and into the hot zone of a quartz tube furnace. Subsequently, 300 mg of sulfur (S) powder was placed approximately 27 cm upstream from the hot zone. The system is purged with argon prior to growth, and sulfur is independently heated to 130 ℃ once the hot zone reaches 500 ℃ to provide a continuous sulfur flow during the MoS_2 growth, which occurs at 800 ℃ for 20 min.

After formation of the MoS_2, the heterostructures are lithographically patterned into isolated channels. Then contact regions are lithographically patterned and Ti/Au is deposited via electron-beam evaporations, followed by lift off of the photoresist. Two structures are produced: 1) a traditional MoS_2-based structure that is directly contacted by the Ti/Au, and 2) an EG/MoS_2/EG lateral heterostructure with the Ti/Au contacting the EG. Additionally, we have formed a HEG/MoS_2/HEG lateral heterostructure with Ti/Au contacts, where HEG stands for hydrogenated EG. The procedure is identical to that in Figure 4.8, except after formation of EG (between (b) and (c)), the EG sample is annealed in hydrogen to release the buffer layer.[57] This is intended to study the effect of doping (as hydrogenation converts n-type EG to p-type HEG) on the transport properties of graphene/MoS_2 heterostructures.

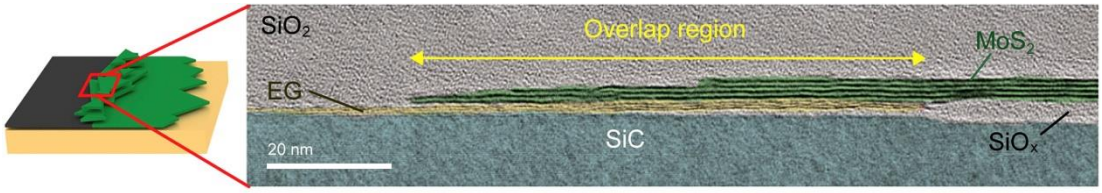

Figure 4.9 Cross-sectional TEM of the MoS_2/EG interface

Cross-sectional transmission electron micrograph (TEM) of the MoS_2/EG interface and schematic of the heterostructure. MoS_2 grows on silicon oxide as well as on edges of the graphene.

A cross-sectional transmission electron micrograph (TEM) of a MoS_2/EG sample is shown in Figure 4.9, focusing on the interface area. The result shows that MoS_2 grows on silicon oxide as well as on edges of the graphene.

4.3.2 LEEM/LEER measurements and band alignments

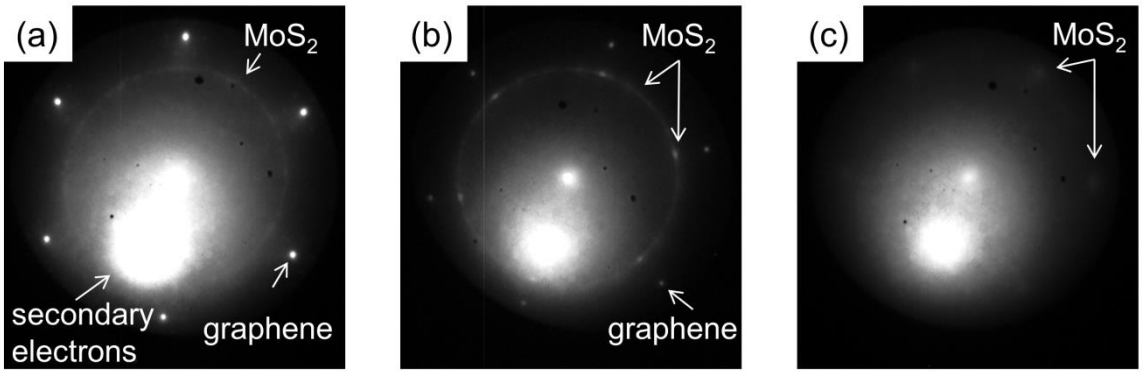

Figure 4.10 Selected-area LEED for the three MoS_2 samples.

Selected-area LEED for (a) the overlap region of MoS_2/EG sample (Figure 4.9); (b) overlap region of MoS_2/HEG; (c) MoS_2 only, i.e. MoS_2 on silicon oxide. All patterns are acquired at 45 eV, using a 5 μm aperture.

Figure 4.10 shows the selected-area LEED patterns obtained for samples EG/MoS_2/EG, HEG/MoS_2/HEG, and MoS_2 (on silicon oxide), respectively. For the first two samples, the aperture is centered on a MoS_2-graphene overlap area. It is clear from the diffraction patterns that crystallinity of the grown MoS_2 is dependent on the substrate. For MoS_2 on EG, the ring of diffraction from the MoS_2 demonstrates random orientations of MoS_2 grains, with sizes considerably smaller than the area illuminated by the electron beam (5 μm). For MoS_2 on HEG, while its diffraction pattern still demonstrates a ring of diffraction, it also shows MoS_2 diffraction spots that are oriented in the same direction as the graphene spots, indicating improved epitaxy. The diffused MoS_2 spots in Figure 4.10(c) suggest the polycrystalline nature of MoS_2 grown on silicon oxide, with grain sizes much smaller than 5 μm.

We have also performed LEER measurements for these samples and extracted the work function differences between varying domains on the surface.[12] Figure 4.11 shows results of such measurements for the EG/MoS_2/EG sample. From the LEEM image Figure 4.11(a), we see clear strips corresponding to MoS_2 and EG repseticvely. From the LEER spectra shown in Figure 4.11(b), we extract a work function difference of 0.47 eV between EG and MoS_2, using the method introduced in Section 2.3.4. We have done

similar measurements and analyses for the other two samples, and obtained a work function difference of 0.05 eV between HEG and MoS_2, and a work function difference of 0.13 eV between MoS_2 and Ti/Au (contact).

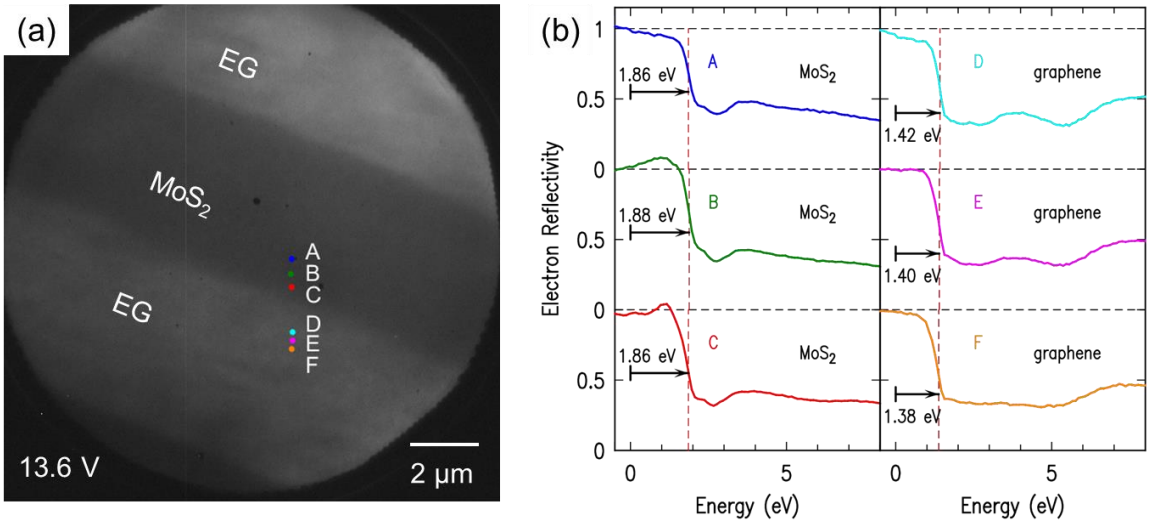

Figure 4.11 LEEM/LEER measurements of EG/MoS_2/EG

LEEM/LEER measurements of the EG/MoS_2/EG sample. (a) LEEM image acquired at a sample voltage of 13.6 V, showing clear strips corresponding to EG and MoS_2 respectively. The points from which LEER spectra are extracted are labeled. (b) The LEER spectra corresponding to the locations labeled in (a). The value specified on the left of each spectrum quantifies the electrostatic surface potential and hence the variation of vacuum level.

Using these extracted work function differences, together with reported values of work functions for EG and HEG, electron affinity of MoS_2 and work function of Ti and Au, we can derive the band alignments for these junctions, shown in Figure 4.12.

Based on the band alignments, we deduce the Schottky barrier for each of the junctions (denoted in red in Figure 4.12). We find that the Schottky barrier of EG/MoS_2/EG is smaller than that of HEG/MoS_2/EG which in turn is smaller than that between MoS_2 and Ti/Au contact. This relationship is consistent with the transport measurements done on the same samples by the Fullerton group at Univ. Pittsburgh.

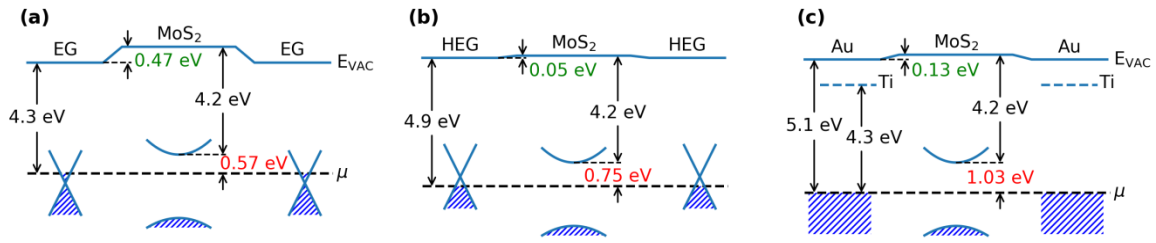

Figure 4.12 Band alignments for different junctions

Derived band alignments based on the vacuum level differences measured via LEEM, for different junctions: (a) EG/MoS_2/EG; (b) HEG/MoS_2/HEG; (c) MoS_2 with Ti/Au contacts on the sides. The values in green signify the measured vacuum level differences, and the values in red denote values of estimated Schottky barrier. Since Au is on top of Ti in the Ti/Au contact, the measured vacuum level variation on the surface is between Au and MoS_2, as shown in (c).

4.3.3 Conclusions

The results for the work in this section show that the Schottky barrier is reduced when epitaxial graphene is introduced to form the MoS_2/EG heterostructure, compared to MoS_2 contacted directly by metal contacts. In addition, it is found that EG is a better contact to the MoS_2 than HEG (this latter conclusion is in contrast to the case of WSe_2 synthesized on graphene as discussed in Section 4.2, where fully hydrogenated epitaxial graphene (HEG) forms a better contact to the WSe_2 than does EG).

4.4 Summary

Through the examples in this section it should be clear that LEEM is a very useful tool for characterizing various 2D materials, or generally surfaces. The imaging mode allows straightforward visualization of different domains on the surface. The selected-area LEED can be routinely used to check crystallinity, grain size, and orientation of grown materials. The LEER provides an unambiguous way to characterize the material and to count the number of atomic layers in the case of 2D materials. The capability to extract work function differences between varying domains provides valuable information

regarding contact and interface of heterostructures, as we have demonstrated in our works above[11,10] , as well as in our more recent LEEM measurements[9].

5 Computation of Current Characteristics in Interlayer TFETs

In this chapter, we discuss theory for computing tunneling currents in two-dimensional (2D) heterostructures. We will focus on vertical transport in such heterostructures. Previous theoretical work for graphene-based device such as graphene-insulator-graphene has made predictions that agree well with the experiment in terms of shape and position of the current peak in I-V characteristics. However, the magnitude of the current predicted by the theory is about 10^4 times larger than that of experiment. The goal of this work is two-fold: to explore limitations in the current theory and propose improvements that allow more accurate, reliable computations of the current magnitude; to extend the theory to be applicable to tunneling in general 2D heterostructures. A large portion of the results presented here is published in *J. Electron. Mater.* (2017).[6] For this work, Prof. Randall Feenstra conceived the idea. Prof. Feenstra and the author (JL) worked together to develop the theory to compute the tunneling current. Yifan Nie from the Cho group at University of Texas, Dallas performed density-functional-theory (DFT) calculations for the various 2D materials. The author computed current characteristics for devices constructed with different 2D materials.

5.1 Introduction

Owing to their very low off-state currents, and steep subthreshold swing when approaching the on state, tunneling field-effect transistors (TFETs) are very attractive devices for low-power electronic applications.[29] In recent years, two-dimensional (2D) layered materials have been studied both theoretically and experimentally for such devices.[126-131] We focus in this work on vertical, interlayer devices in which the tunneling occurs between 2D layers (rather than within a layer). Such devices consist of two electrodes (source and drain), surrounded by one or two gates, as pictured in Figure 5.1(a). The source and drain may be separated by one or more layers of insulating

material forming the tunnel barrier (such as hexagonal boron nitride, h-BN), or in principle the tunneling can occur simply between the van der Waals (vdW) gap that separates the source and drain. Following Li et al.,[126,127] we refer to such devices as two-dimensional heterojunction interlayer tunneling field-effect transistors (Thin-TFETs).

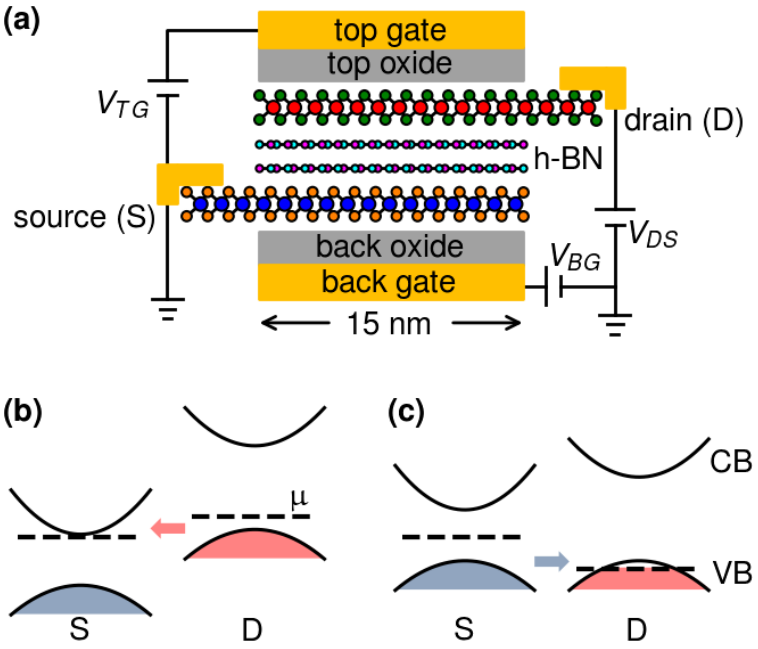

Figure 5.1 Schematic and tunneling modes of Thin-TFET.

(a) Schematic view of Thin-TFET. Source and drain electrodes are typically made of transition metal dichalcogenide monolayers, with zero, one or more layers of h-BN as the tunneling barrier. (b) and (c) Unlike-band and like-band tunneling, respectively, showing the valence band (VB) and conduction band (CB) of the source (S) and drain (D) electrodes. Dashed lines represent the Fermi levels of the electrodes. A source/drain overlap length of 15 nm is assumed, as indicated.

There are two fundamentally different modes of operation for a Thin-TFET: tunneling between unlike bands, or tunneling between like bands, as schematically illustrated in Figure 5.1(b) and (c).[6] For unlike-band tunneling, electrons flow from the valence band (VB) of one electrode to the conduction band (CB) of the other. This is the usual mode for TFETs, providing a steep turn-on of the current when the bands overlap (this mode is also known as band-to-band, Zener, or reverse-bias tunneling). In contrast,

for like-band tunneling, the electrons flow from VB to VB or CB to CB, i.e. depending on the Fermi-level positions in the source and drain. For the case of 2D materials in particular, this mode yields negative differential resistance (NDR) due to the phenomenon of "lateral momentum conservation" during the tunneling (hence, this mode is sometimes referred to as 2D-2D tunneling).[132-138]

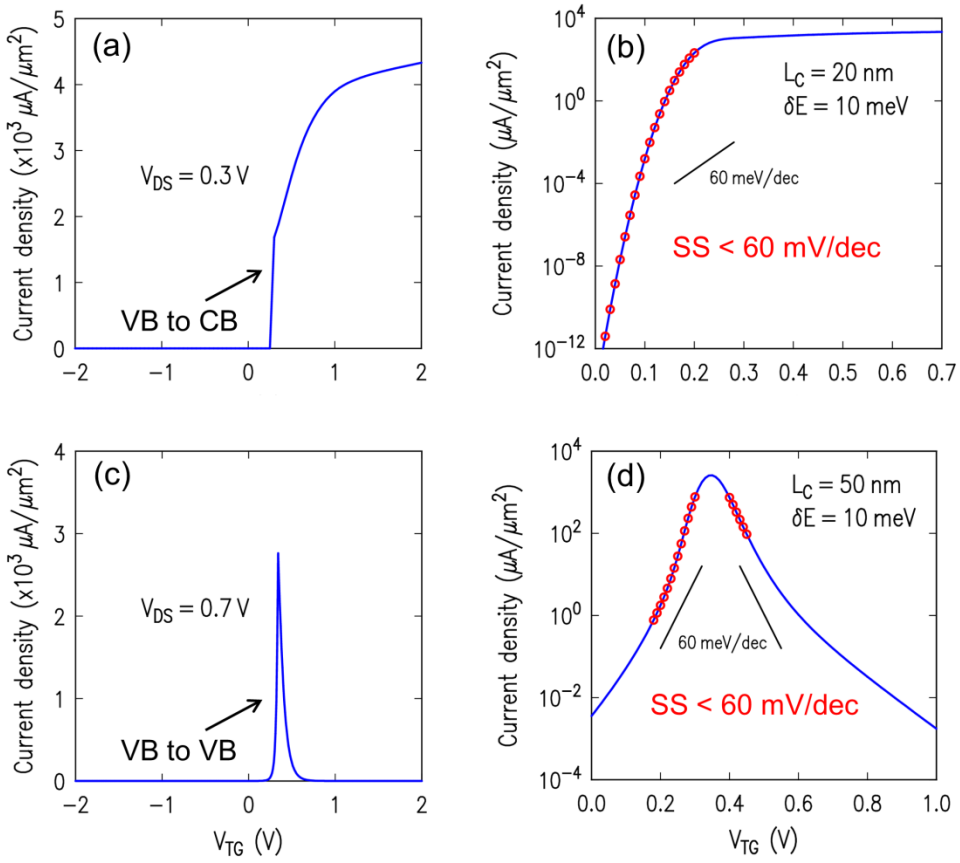

Figure 5.2 Examples of two tunneling modes of interlayer TFETs

Examples of computed current characteristics of unlike-band tunneling on linear scale (a) and log scale (b), and like-band tunneling on linear scale (c) and log scale (d). The red circles in (b) and (d) show voltage ranges where the subthreshold swing (SS) is lower than 60 mV/dec.

In Figure 5.2 we show examples of computed current characteristics of the two tunneling modes. Figure 5.2(c) shows characteristic NDR for like-band tunneling. By comparing Figure 5.2(c) and (d) (note that their y-scales are different), we see that the subthreshold slope for unlike-band tunneling is much steeper than that for like-band

tunneling. This is due to the aforementioned different tunneling mechanisms: sharp turn on when the bands start to overlap for unlike band tunneling, and NDR due to conservation of the lateral momentum for like band tunneling.

5.2 Electrostatics

We deal with electrostatics for the Thin-TFET (Figure 5.1) by solving one dimensional Poisson's equation. Assuming the capacitances of the top oxide, back oxide, and the insulating h-BN layer are C_{TOX}, C_{BOX} and C_{IOX} are respectively. Then by the Gauss law, we have[126]

$$\begin{aligned} -C_{TOX}V_{TOX} + C_{IOX}V_{IOX} &= e(p_T - n_T + N_D) \\ -C_{BOX}V_{BOX} - C_{IOX}V_{IOX} &= e(p_B - n_B - N_A) \end{aligned} \tag{17}$$

where V_{TOX}, V_{BOX}, and V_{IOX} are the voltage drops across the top oxide, back oxide, and the insulating h-BN layer. N_D and N_A are n-doping of top electrode and p-doping of bottom electrode respectively.

$$\begin{aligned} n &= \int_{E_C}^{\infty} dos(E)\, f(E, E_F)\, dE \\ p &= \int_{-\infty}^{E_V} dos(E)(1 - f(E, E_F))\, dE \end{aligned} \tag{18}$$

are carrier densities of electrons and holes respectively. The density of states $dos(E)$ can be computed analytically assuming a parabolic effective mass approximation[126,132] or numerically using the density functional theory (DFT) calculated density of states[6]. $f(E, E_F) = 1/(1 + \exp\{(E - E_F)/kT\})$ is the Fermi-Dirac distribution for the occupation factor of electrons.

The voltage drops in (17) can be related to external voltages applied and electron affinities of the electrodes,

$$\begin{aligned} eV_{TOX} &= eV_{TG} + e\phi_{n,T} - eV_{DS} + \chi_{2D,T} - \Phi_{M,T} \\ eV_{BOX} &= eV_{BG} - e\phi_{p,B} + E_{GB} + \chi_{2D,B} - \Phi_{M,B} \\ eV_{TOX} &= eV_{DS} - e\phi_{p,B} - e\phi_{n,T} + E_{GB} + \chi_{2D,B} - \chi_{2D,T} \end{aligned} \tag{19}$$

where V_{TG}, V_{BG} and V_{DS} are applied top gate voltage, bottom gate voltage and source drain bias as shown in Figure 5.1. $\Phi_{M,T}$ and $\Phi_{M,B}$ are work functions of top and bottom gates. $\chi_{2D,T}$ and $\chi_{2D,B}$ are electron affinities of top and bottom (2D) electrodes. E_{GB} is band gap of bottom electrode. $e\phi_{n,T}$ is energy difference between Fermi level and conduction band minimum of the top electrode and $e\phi_{p,B}$ difference between valence band maximum and Fermi level of the bottom electrode.

5.3 Single Plane Wave Treatment

Before touching on the details of the methodology, we take a look at why the Bardeen approach is more desirable compared to some other methods for our problem. Essentially we have the following 2D tunneling problem (Figure 5.3(a)). Electrons flow from the left of source electrode towards right, as they approach the overlap region of the source and drain, the wavefunction spreads out. Part of it transmits through the gap into the drain electrode while the rest is reflected back. It is difficult to solve this problem exactly using the first-principles method because one needs to consider a supercell that is not only large on the *z* direction (tunneling direction), but also macroscopically large on the *x* direction due to in-plane heterogeneity, let alone other difficulties such as lattice mismatch when the source and the drain are made of different 2D materials.

One way to solve the problem approximately is to use the tight-binding model, although few such results exist in the literature. One major difficulty of using the tight-binding for this problem is obtaining reliable, accurate estimates of the hopping parameters. The Bardeen approach avoids all these problems at the price of reduced (but still reasonable, detailed in section 5.4.5) accuracy. It assumes that we have the wavefunctions of the source and the drain in absence of the other, i.e. for source and drain separately. Once we have the wavefunctions, the Bardeen formalism involves evaluation of the overlap integral of the wavefunctions from the two electrodes.[132,139] For the wavefunctions of the 2D electrodes, researchers have either assumed some simple analytic form, like the single plane wave treatment discussed below,[126,127] or have computed them using the first-principles density functional theory.[6]

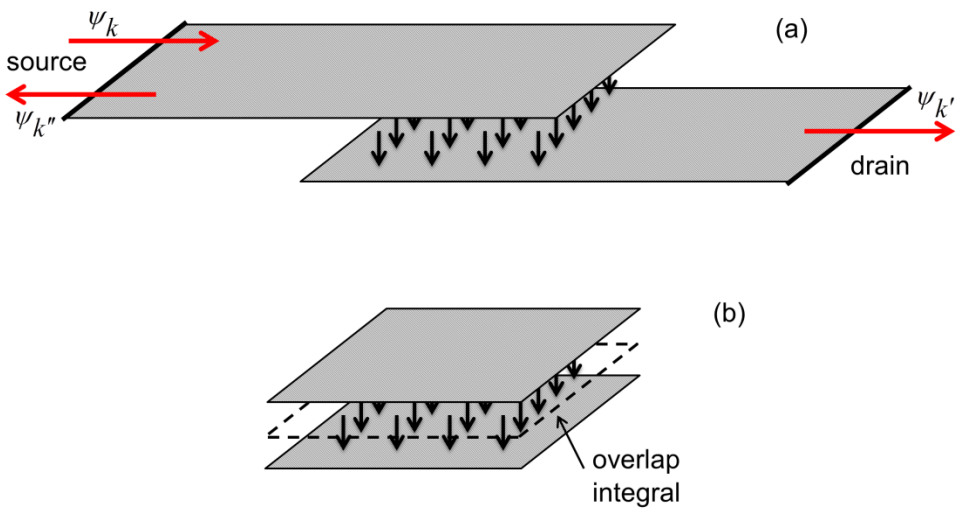

Figure 5.3 Schematic of 2D tunneling and Bardeen approach

(a) Schematic of 2D tunneling, showing incoming wavefunction ψ_k, transmitted wavefunction $\psi_{k'}$ and reflected wavefunction $\psi_{k''}$. (b) Schematic of the Bardeen approach to the problem, which involves evaluation of the integral of the overlap of source and drain wavefunctions.

Earlier works that apply the Bardeen formalism to the interlayer tunneling of 2D materials have employed a "single plane wave" treatment.[126,127,132,135] In that treatment, the conduction (or valence) band of a 2D material is approximated by a single effective-mass band (Figure 5.4(a)). This approximation allows derivation of an analytic form for the density of states to be used in the electrostatics.[126,127] Additionally, the wavefunctions are assumed to decay exponentially into the barrier (or vacuum) between the two 2D materials and be plane-wave characteristic in the lateral direction in the overlap region (Figure 5.4(b)). Under these assumptions, the prior theory has made predictions about the current characteristics in graphene tunneling device that agree with the experiment in terms of shape and position of the NDR peaks.[132,133,135] However, despite that agreement, there was a large discrepancy between the magnitude of the computed current compared to experiment. This motivates our work in the next section, using wavefunctions computed from first-principles density-functional theory and with currents computed using the Bardeen formalism.

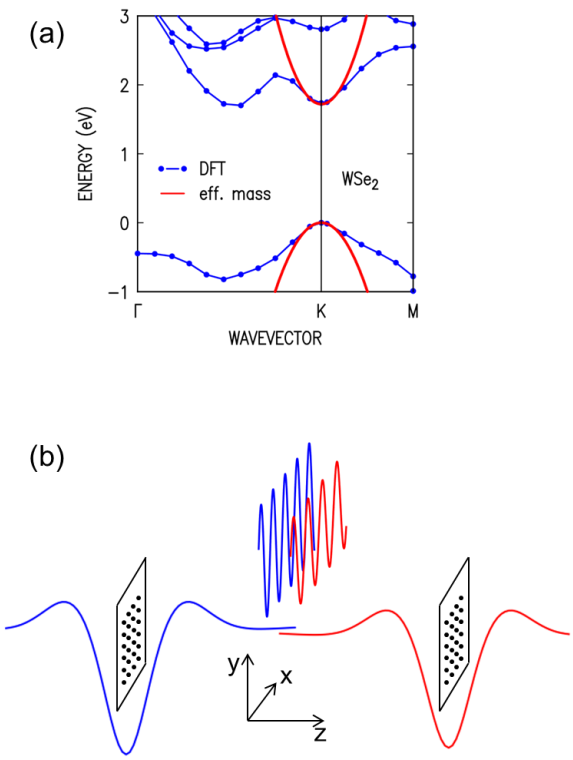

Figure 5.4 Single plane wave treatment of 2D Bardeen tunneling

(a) Single effective mass band approximation to the conduction and valence band of monolayer WSe_2. (b) Plane wave characteristics assumed for the lateral part of wavefunctions of the two 2D materials in the overlap region (e.g. middle of the barrier). The atomic planes are pictured as grids of dots, in the *xy* plane. Plane wave character in the *xy* direction for the wavefunctions exists both on the atomic planes and extending out into the space between the planes, as pictured.

5.4 DFT-Bardeen Method

In this section we consider unlike-band tunneling in Thin-TFETs, focusing on the magnitudes of the currents that are attainable in such devices. We employ the Bardeen tunneling approach,[139,140] with wavefunctions from density-functional theory (DFT). The tunneling currents that we obtain differ, by as much as an order of magnitude, from those obtained in some prior theoretical approaches to this problem.[126,127,131-135,137,138] The main goal of this work is to obtain reliable estimates of the magnitude of the tunnel current, for comparison with benchmark values that are needed for low-power digital applications.

We discuss the differences between the details of the various theoretical approaches, and argue that our present method provides reasonably reliable estimates for the magnitude of the current (while at the same time recognizing that certain aspects of the problem are not well treated in the present computations).

5.4.1 Theoretical Method

We employ the Bardeen method for tunneling,[139-141] as described in detail in our previous work which dealt with graphene-based devices.[132] This method is a first-order perturbative approach, which does not permit inclusion of interactions between the electrodes (other than those that produce tunneling). Rather, it treats the electronic structure each electrode *in the absence* of the other, and hence electrodes of differing materials can be easily handled (i.e. without explicitly considering the large unit cells that constitute an epitaxial match between the two materials). However, when the tunneling barrier consists simply of a vdW gap between source and drain (i.e. with no h-BN or other insulator in the barrier) then certainly the interactions between electrodes will not be negligible. Nevertheless, the goal of our work is to evaluate how the magnitude of the tunnel current will vary depending on the material used for the source and drain electrodes, i.e. depending on the overlap of the wavefunctions between the two electrodes. In this regard our computations employing the Bardeen method provide useful information, since we find orders-of-magnitude variations in the tunneling current depending on the materials. We also note that even though the tunnel barriers formed in the vdW gap between 2D electrodes are relatively small, we find that the Bardeen method still works fairly well (accuracy of a factor of 2 – 3, with the currents being *underestimated* by this amount) for the cases we consider, as demonstrated in the Appendix.

In contrast to prior work which employed only a very approximate form of the wavefunction (i.e. just a single plane-wave, SPW),[132,133] in the present work we employ the full form of the wavefunctions as given by the Vienna Ab Initio Simulation Package (VASP),[81] with the projector-augmented wave method. The Perdew-Burke-Ernzerhof form of the generalized-gradient approximation (GGA) for the density functional is used.[142] The wavefunctions are expanded in plane waves with a kinetic energy cutoff of

500 eV, and the convergence criterion for the electronic relaxation is 10^{-4} eV. The computation of states over the Brillouin zone (BZ) needed to compute the tunnel current is performed typically with a 32×32×1 or 40×40×1 Monkhorst-Pack k-point mesh.[143] The structure of the transition metal dichalcogenide (TMD) monolayers follows a prior theoretical study.[144] The TFET electrodes are modeled simply as single monolayers (MLs) of the 2D materials (e.g. adjacent planes of Se-W-Se for the case of WSe_2, where we refer to that assembly as a ML). Each supercell includes a vacuum region with width of about 20 Å, to minimize the interaction between adjacent supercells.

Energy bands for monolayer (ML) WSe_2 and ML $SnSe_2$ are pictured in Figure 5.5(a) and (b), respectively, using their hexagonal Brillouin zones (BZs). WSe_2 has its VB maximum at the K-point, and it has two CB minima, one at the K-point and the other at a slightly lower energy located at a Q-point between Γ and K. $SnSe_2$ has its VB maximum located between Γ and M, and its CB minimum at the M-point. Energy bands for phosphorene are pictured in Figure 5.5(c).[145] The BZ is rectangular in this case, with CB minimum at the Γ-point and a VB maximum that is relatively broad and extends from the Γ-point to a point between Γ and X.

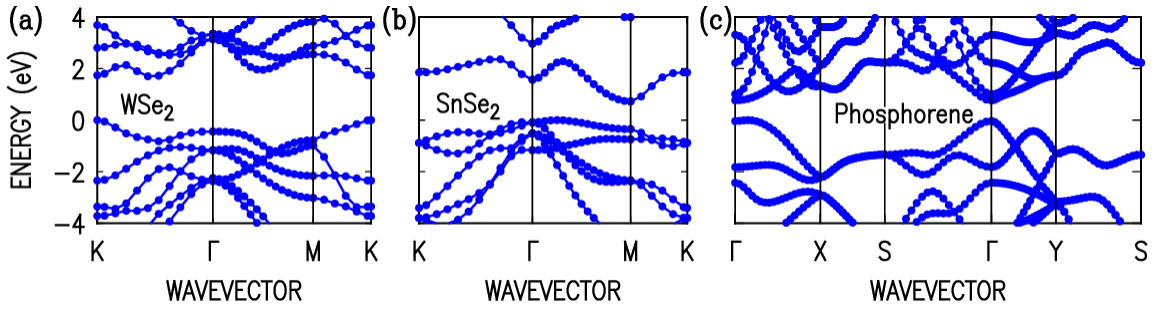

Figure 5.5 Energy bands for 2D materials computed by DFT.

Energy bands for (a) ML WSe_2, (b) ML $SnSe_2$, and (c) Phosphorene from DFT computations. For the plots, the zero energy level has been taken to be that of VB maximum for each of the materials.

The wavefunctions that we employ from VASP take the form of plane-wave expansions,

$$\psi_{\nu,\mathbf{k}}(\mathbf{r}) = \sum_{\mathbf{G}} \frac{C_{\nu,\mathbf{k},\mathbf{G}}}{\sqrt{V_C}} e^{i(\mathbf{k}+\mathbf{G})\cdot\mathbf{r}} \tag{20}$$

where $C_{\nu,\mathbf{k},\mathbf{G}}$ are the expansion coefficients for band ν, wavevector $\mathbf{k} \equiv (k_x, k_y, k_z)$, and reciprocal lattice vector of the simulation cell $\mathbf{G} = (G_x, G_y, G_z)$. V_C is the volume of the cell, to which the VASP wavefunctions are normalized. We find it more convenient to employ an area $A = L^2$ for the lateral part of the wavefunction, rather than the area of the unit cell A_C, and hence we multiply the wavefunctions by a factor of $\sqrt{A_C / A}$. Including a factor of 2 for spin degeneracy, tunnel currents are obtained from[139,140]

$$I = \frac{4\pi e}{\hbar} \sum_{\alpha,\beta} \left|M_{\alpha\beta}\right|^2 \left[f_L(E_\alpha) - f_R(E_\beta) \right] \delta(E_\alpha - E_\beta) \tag{21}$$

with matrix element given by

$$M_{\alpha\beta} = \frac{\hbar^2}{2m} \int dS \left(\psi_\alpha^* \frac{d\psi_\beta}{dz} - \psi_\beta \frac{d\psi_\alpha^*}{dz} \right) \tag{22}$$

where $\alpha \equiv (\mathbf{k}_\alpha, \nu_\alpha)$ and $\beta \equiv (\mathbf{k}_\beta, \nu_\beta)$ label the states of the two electrodes, having energies E_α and E_β, respectively, and where *m* is the free electron mass. We choose the normalization length in the *z* direction to be the supercell period, in which case we need only include the standing wave states with $k_z = 0$ in this computation of the current; thus we henceforth take $\mathbf{k} \equiv (k_x, k_y)$ for both electrodes. In Eq. (2), f_α and f_β are Fermi occupation factor for the electrodes, $f_\alpha(E) = \left\{1 + \exp\left[(E - \mu_\alpha)/k_B T\right]\right\}^{-1}$ and $f_\beta(E) = \left\{1 + \exp\left[(E - \mu_\beta)/k_B T\right]\right\}^{-1}$, where μ_α and μ_β are the chemical potentials in the two electrodes, $\mu_\alpha - \mu_\beta = -eV$, where *V* is the applied bias on the α-electrode relative to the β-electrode.

Utilizing Eq. (20) for the wavefunctions, we evaluate the integrand of Eq. (22) to be

$$\frac{i}{A}\sqrt{\frac{A_{C,\alpha}A_{C,\beta}}{V_{C,\alpha}V_{C,\beta}}}\sum_{\mathbf{G}_\alpha,\mathbf{G}_\beta}(G_{z,\beta}+G_{z,\alpha})C^{*}_{\mathbf{G}_\alpha,\mathbf{k}_\alpha,\nu_\alpha} \\ C_{\mathbf{G}_\beta,\mathbf{k}_\beta,\nu_\beta}e^{i(G_{z,\beta}-G_{z,\alpha})z}e^{i(\mathbf{k}_\beta+\mathbf{G}_{\beta,\rho}-\mathbf{k}_\alpha-\mathbf{G}_{\alpha,\rho})\cdot\boldsymbol{\rho}} \tag{23}$$

with $\boldsymbol{\rho}\equiv(x,y)$ and where $\mathbf{G}_\rho\equiv(G_x,G_y)$ for both electrodes. The integrand is evaluated at the point *z*, which is half of the barrier width from the atomic planes of the 2D layers of each electrode. The barrier width is determined by the experimental separation between the electrode materials, if known, or if not then by the average of the layer-separations of the individual electrode materials in bulk form. Considering now the surface integral over the plane separating the electrodes, the only term in Eq. (23) that has any (*x*,*y*) dependence is the final exponential term. We have argued previously that a useful model for evaluating the surface integral is to consider a phase coherent area for the wavefunctions in the respective electrodes, given by $A=L^2$ where *L* is denoted as the coherence length (we have utilized the same *L* above for the wavefunction normalization). The surface integral of the final exponential in Eq. (23) is then easily evaluated, yielding

$$L^2\,\mathrm{sinc}\left(\frac{L\,q_x}{2}\right)\mathrm{sinc}\left(\frac{L\,q_y}{2}\right) \tag{24}$$

where $q_x\equiv k_{\beta,x}+G_{\beta,x}-k_{\alpha,x}-G_{\alpha,x}$, $q_y\equiv k_{\beta,y}+G_{\beta,y}-k_{\alpha,y}-G_{\alpha,y}$, and $\mathrm{sinc}(u)\equiv\sin(u)/u$. As previously discussed,[135] a somewhat better model is to utilize a *distribution* of phase coherence lengths, in which case the expression of Eq. (24) can be replaced by

$$\frac{L^2}{[1+(q/q_c)^2]^{3/2}} \tag{25}$$

with $q_c\equiv 2\pi/L$, $q=|\mathbf{q}|=\sqrt{q_x^2+q_y^2}$.

Combining Eqs. (21), (22), (23) and (25), a formal expression for the tunnel current is easily obtained. However, this expression still contains the energy δ-functions of Eq. (21). One could simply broaden those δ-function (e.g. as done in Ref. 131), but since we are interested in evaluating the steepness of the turn-on for unlike band tunneling, we wish to avoid such broadening. Hence we convert the sum in Eq. (21) for

one of the electrodes, say the β-electrode, into an integral over $\mathbf{k}_\beta$ (two-dimensional wavevector), and then into an integral over energy according to

$$\sum_{\mathbf{k}} = \frac{A}{(2\pi)^2}\int\int d^2k = \frac{A}{(2\pi)^2}\int dE \int \frac{d\ell_k}{|\nabla_k E|}, \tag{26}$$

where $\int d\ell_k$ is a line integral in **k**-space along a constant-energy contour. In this way the energy δ-function can be used to evaluate the energy integral, with the line integral and the gradient term evaluated at the specific energy of the state of the α-electrode. Hence, the expression for the tunnel current becomes

$$I = \frac{e}{\pi\hbar}\frac{A_{C,\alpha}\,A_{C,\beta}\,A}{V_{C,\alpha}\,V_{C,\beta}} \sum_{\mathbf{k}_\alpha,\nu_\alpha,\nu_\beta} \left[f_\alpha(E_{\mathbf{k}_\alpha,\nu_\alpha}) - f_\beta(E_{\mathbf{k}_\alpha,\nu_\alpha}) \right] \int \frac{d\ell_{k_\beta}}{|\nabla_k E_\beta|} \left|M_{\alpha\beta}\right|^2 \tag{27}$$

where

$$M_{\alpha\beta} = \frac{\hbar^2}{2m} \sum_{\mathbf{G}_\alpha,\mathbf{G}_\beta} \frac{(G_{z,\beta}+G_{z,\alpha})\,C^*_{\mathbf{G}_\alpha,\mathbf{k}_\alpha,\nu_\alpha} C_{\mathbf{G}_\beta,\mathbf{k}_\beta,\nu_\beta} e^{i(G_{z,\beta}+G_{z,\alpha})z}}{[1+(q/q_c)^2]^{3/2}} \tag{28}$$

with f_α and f_β defined following Eq. (22), q and q_c defined following Eq. (25), and where, again, the line integral along the constant-energy contour in the β-electrode is evaluated at the specific energy of each state of the α-electrode. Equation (27) as written provides the current over an $L\times L$ area, so that current density is given by I/A. For our results in the following section, we consider an overlap length between source and drain of 15 nm, so the current per unit electrode width is I/A times 15 nm.

To evaluate the β-electrode line integrals, a small area around each k-point that is exclusive to that point is defined (i.e. a "mini BZ", with same shape as the BZ but smaller in area by a factor of n^2 for a $n\times n$ mesh). This area is split up into a series of triangles utilizing the lines joining the particular k-point with its neighbors. Using linear interpolation of the energies between neighboring k-points, the constant-energy contour is defined within each triangle and hence in a piecewise linear fashion across the entire BZ, and similarly the magnitude of the gradient $|\nabla_k E|$ is evaluated along the contour.

The magnitude of $\left|M_{\alpha\beta}\right|^2$ varies along the line integral, in accordance with both the q values and the values of the $C_{\mathbf{G}_\beta,\mathbf{k}_\beta,\nu_\beta}$ coefficients; the former are accurately known, and the latter are evaluated depending on which particular k-point is nearest the specific point on the contour. We perform linear interpolation of the $\left|M_{\alpha\beta}\right|^2$ values from neighboring k-points when we evaluate the line integral.

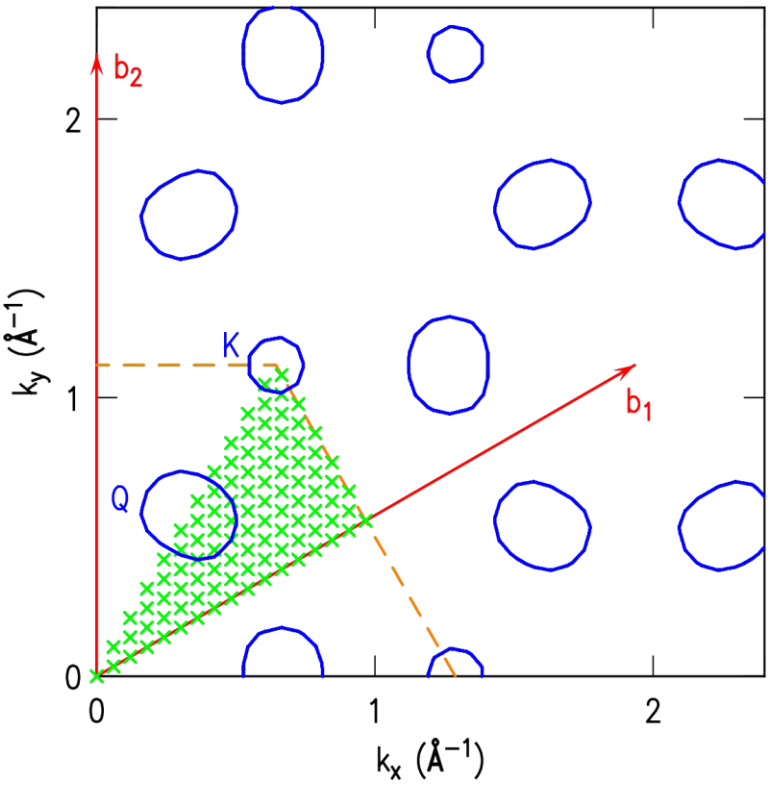

Figure 5.6 Section of reciprocal space for ML WSe_2

Section of reciprocal space for ML WSe_2, showing the k-points (x-marks) in the irreducible wedge of a 32×32 Monkhorst-Pack mesh in the BZ. Orange dashed lines show the edge of the BZ, with reciprocal vectors $\mathbf{b}_1$ and $\mathbf{b}_2$ indicated. Constant-energy contours are represented by blue ovals, for an energy of 0.06 eV above the conduction band minimum at the K-point; contours around the K-points and Q-points are apparent.

For these evaluations, in the β-electrode, all states must be fully defined across the entire BZ (i.e. not just the irreducible wedge of the BZ). For this purpose, we transform both the energies (as scalar quantities) and the plane-wave coefficients (as vector quantities) from the irreducible wedge to all other parts of the BZ. For the coefficients, transformation to negative **k** values is accomplished by time reversal, in which the complex conjugates of the wavefunctions are computed, since the real-space unit cells of the materials lack inversion symmetry in some cases. As an example of intermediate quantities in our computation, we display in Figure 5.6 the constant-energy contours of the WSe_2 conduction band, evaluated at an energy of 0.06 eV above the conduction band minimum at the K-point. The contours are shown in a repeated-zone scheme, with each zone representing one of the $\mathbf{G}_\beta$ terms from the summation of Eq. (28). (Note that for the particular 32×32 mesh used here, there is not a k-point directly at the K corner of the BZ; nevertheless in our computations we add that point from a separate VASP run, e.g. using a 12×12 mesh, to permit a reasonably good description of the contours even very near the K-point).

Concerning the states of the α-electrode, in principle we should also extend those over the entire BZ in a similar manner as for the β-electrode. However, in many cases (e.g. for the same symmetry of both electrodes and no angular misorientation between them) it suffices to simply multiply the current obtained from a particular state associated with a k-point within the irreducible wedge of the BZ by a suitable factor (e.g. multiplier of 12 for a general point in the irreducible wedge of a hexagonal BZ). Additionally, it is important to realize that since we have normalized the wavefunctions to the volume AV_C / A_C then we have, formally speaking, A/A_C k-points in the sum over $\mathbf{k}_\alpha$ in Eq. (27). Hence, for the $n \times n$ mesh of k-points that we actually use in the computation, the total current must be multiplied by $A/(A_{C,\alpha}\, n^2)$. As just described, it is clear that the treatment of the two electrodes is quite different in our methodology. Of course, it is possible to swap the sense of the electrodes (together with changing the sign of the applied bias voltage), so that we can choose which electrode to be the α- or the β-one.

Generally, it is advantageous to place the electrode with the flattest band as the α-one, so that the spacing of the constant-energy contours in the β-electrode is as small as possible.

To model the electrostatics of the Thin-TFET, we employ the method described in Ref. 126, which solves a one-dimensional (1D) Poisson equation in the z direction. In this model, the difference of Fermi levels of source and drain is determined by the applied source-drain voltage. The source-drain band alignment is determined by that voltage together with the electron affinities and band gaps of the electrodes and the detailed parameters associated with the gates (dielectric constants, work functions, gates voltages). One gate is held at a fixed potential, and a voltage applied to the other gate then acts to tune the band alignment. In this 1D model, the current density is uniform over the 15 nm overlap area of the electrodes (this assumption of uniform current density over the overlap region is consistent with results from other reports,[146,147,148] discussed in more detail below, which include the possibility of in-plane variation in the potentials and current densities over the electrodes). We also mention that our electrostatic computation uses the DFT-generated density of states, which includes multiple bands (important e.g. for the CB of WSe_2), whereas the model of Ref. [126] employs only a single-band effective-mass treatment.

5.4.2 Results

We focus on results for 2D materials that have band gaps, for which unlike-band tunneling will produce a steep slope at the onset of the current. In particular, we consider chalcogenide materials (i.e. containing S, Se or Te) as well as phosphorene (Phos). For heterojunction devices, an important criterion in choosing the respective materials of the source and drain is the energy offset between the CB edge of one material (material 2) relative to the VB edge of the other (material 1), i.e. $\Delta E_{CV} = E_C^{(2)} - E_V^{(1)}$. Ideally this energy difference will be relatively small, so that the appropriate band edges are approximately aligned (relative to the vacuum level) without application of large gate voltages. One such heterojunction that has been previously proposed in this regard is WSe_2-$SnSe_2$, with $\Delta E_{CV} = 0.2$ eV.[127] We examine this case in detail here, and compare it to a Phos-Phos TFET (which does not have a small ΔE_{CV} value, but nonetheless is interesting for comparison purposes since the resulting tunnel currents are larger).

For all computed current results presented in this work, we consider a coherence length of 10 nm, a source/drain overlap length of 15 nm, equivalent oxide thickness (EOT) in the gate dielectrics of 1 nm for both gates, and drain source bias (V_{DS}) of − 0.2 V. A vdW gap, i.e. zero layers of h-BN in the tunnel barrier, is assumed. We also choose different gate work functions (within realistic range) for different devices in order to better align the bands of the source and drain electrodes and thusly maximize the current.

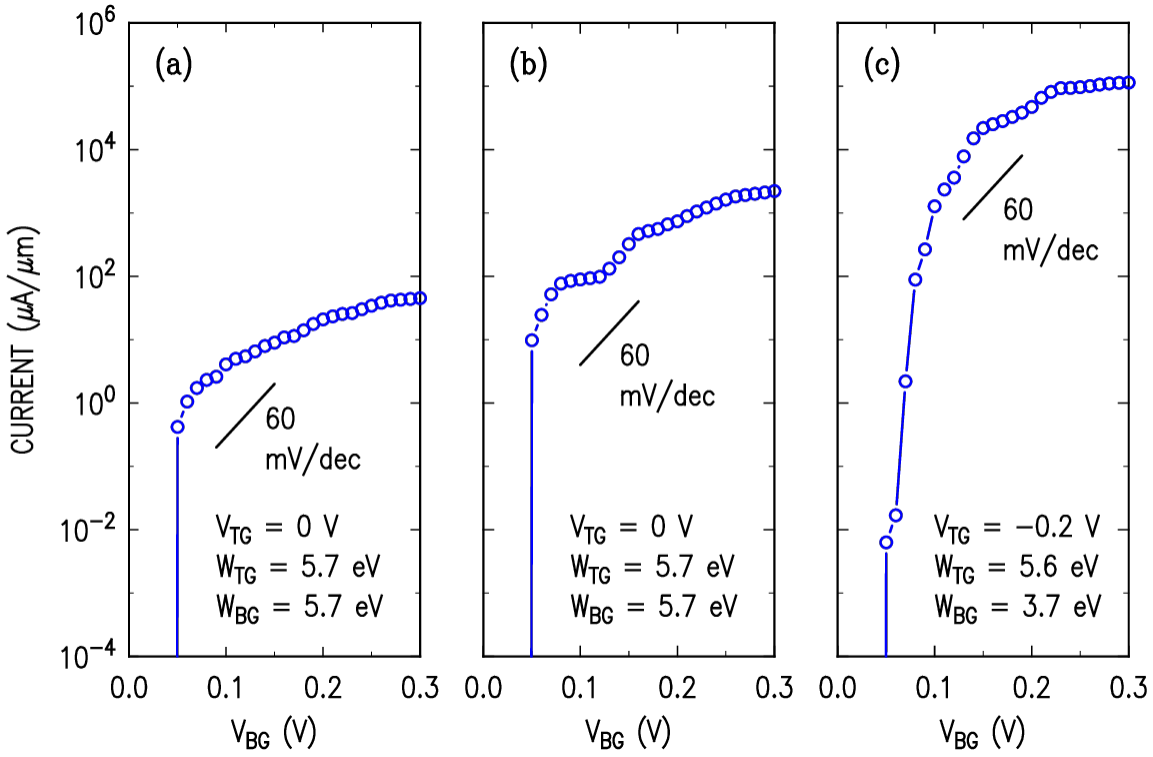

Figure 5.7 Tunneling current characteristics computed for Thin-TFET

Current flowing from source to drain, I_D, as a function of bottom gate voltage, V_{BG}, for (a) a WSe_2-$SnSe_2$ device with their lattice being aligned (b) a WSe_2-$SnSe_2$ device with 30 °rotational misalignment between their lattices and (c) a Phos-Phos device with their lattices aligned. Values are listed for top gate voltage (V_{TG}) and work functions of top gate (W_{TG}) and bottom gate (W_{BG}).

Figure 5.7(a) shows the computed I_D vs. V_{BG} characteristic for a WSe_2-$SnSe_2$ TFET, with the lattices of WSe_2 and $SnSe_2$ being aligned. The current is caused by tunneling of electrons from the VB maximum of WSe_2 to the CB minimum of $SnSe_2$. Note that there is a wavevector mismatch between the tunneling states. Figure 5.7(b)

shows the result still for a WSe_2-$SnSe_2$ TEFT, but with 30 ° rotation between their lattices in order to better align the wavevectors of the $SnSe_2$ CB minimum with those of the WSe_2 VB maximum. An obvious increase in the magnitude of the current is observed. Figure 5.7(c) shows the result for the Phos-Phos device, where we see that the tunneling currents are much larger than those of the WSe_2-$SnSe_2$ (either 0 ° or 30 °) device. This difference originates from the overlap matrix elements of the two cases, i.e. Eq. (1), which for WSe_2-$SnSe_2$ are relatively small due to the detailed nature (symmetry) of the wavefunctions, whereas for Phos-Phos the values are much larger.

From the I_D-V_{TG} characteristic shown in Figure 5.7, we can extract values that are useful for benchmarking of the device performance. Specifically, the current at which the subthreshold swing (SS) changes from <60 mV/dec to >60 mV/dec is denoted by I_{60}. In addition, an ON current for the device, I_{ON}, can be characterized by taking the current at a gate voltage that is +0.2 V greater than the onset voltage of the characteristic. We multiply the current densities from the computations by the overlap length in order to obtain currents per unit width of the device, μA/μm. In Figure 5.8 we display these two quantities, I_{60} and I_{ON}, for the WSe_2-$SnSe_2$ (0 ° and 30 °) and Phos-Phos devices jut discussed as well as for a variety of other Thin-TFETs. Structures of most of the materials in Figure 5.8 follow a prior theoretical study.[144] Additionally we considered other 2D materials such as GaSe.[149] Again, we only consider cases where the energy difference $\Delta E_{CV} = E_C^{(2)} - E_V^{(1)}$ is relatively small, with ΔE_{CV} deduced from the DFT computations (We note that DFT is well known to underestimate experimental band gap values.[150] An approximate correction to the band gaps will cause a right-shift of our results in Figure 5.8 by a quarter of the sum of the DFT band gap values of the source and drain electrodes.[144]). On this plot we also include typical desired values for these quantities for low-power digital applications, I_{60} = 1 μA/μm and I_{ON} = 200 μA/μm.[151,152,153] We see that the WSe_2-$SnSe_2$ (30 °) device satisfies these benchmark values, while the WSe_2-$SnSe_2$ (0 °) TFET falls below the desired values.

The Phos-Phos device shows a relatively large current, with $I_{60} = 1.50\times10^4$ μA/μm and $I_{ON} = 9.39\times10^4$ μA/μm. We emphasize that our theory ignores any modifications to the band structure of such a device due to interactions between the

electrodes, and indeed these have been shown to be large for the case of Phos-Phos tunneling devices by Constantinescu et al.[131] Those authors argued that a tunnel barrier consisting of one or few layers of h-BN is desirable in order to reduce the interactions between the Phos electrodes. To roughly estimate the inclusion of h-BN in the barrier, we can reduce our current by a factor of 50 for each layer of h-BN added (this factor of 50 arises from explicit computations for graphene/h-BN/graphene tunnel junctions, discussed elsewhere,[8] and is in very good agreement with experimental measurements for this system[154]). For the Phos-Phos TFET, including a single layer of h-BN then yields an ON current $I_{ON} = 1.9 \times 10^3$ μA/μm, still well above the desired values.

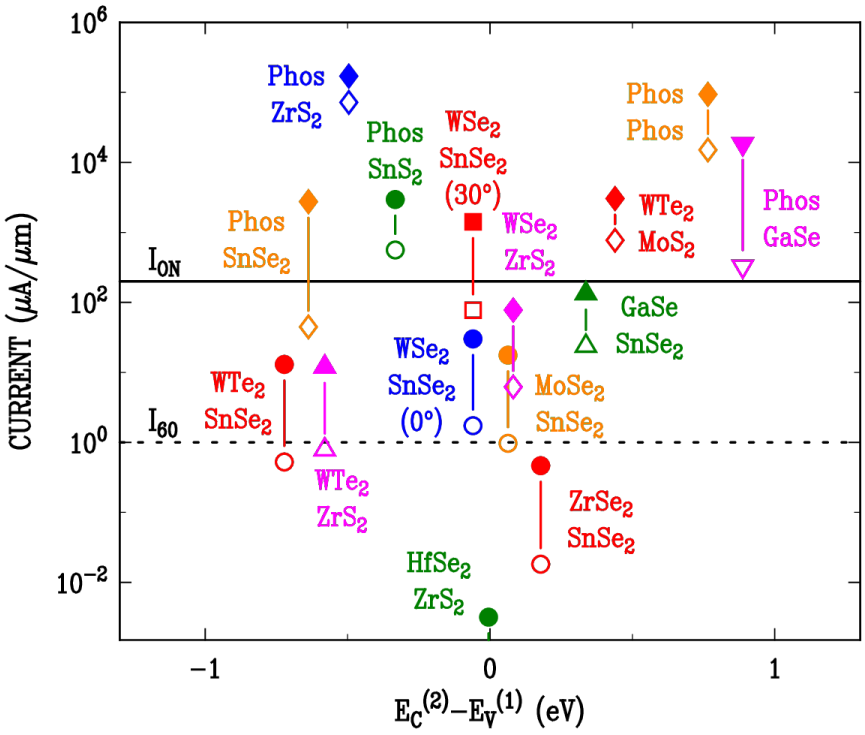

Figure 5.8 I_{ON} and I_{60} computed for diverse Thin-TFETs

Results for I_{60} (open symbols) and I_{ON} (closed symbols), for Thin-TFET devices made from the materials shown. Electrons flow from the VB of the upper material (denoted 1) to the CB of the lower material (denoted 2), with the difference between these band edges given by $\Delta E_{CV} = E_C^{(2)} - E_V^{(1)}$. The difference ΔE_{CV} is deduced from the DFT computation. Desired values for I_{ON} and I_{60} are indicated by solid and dashed lines, respectively.

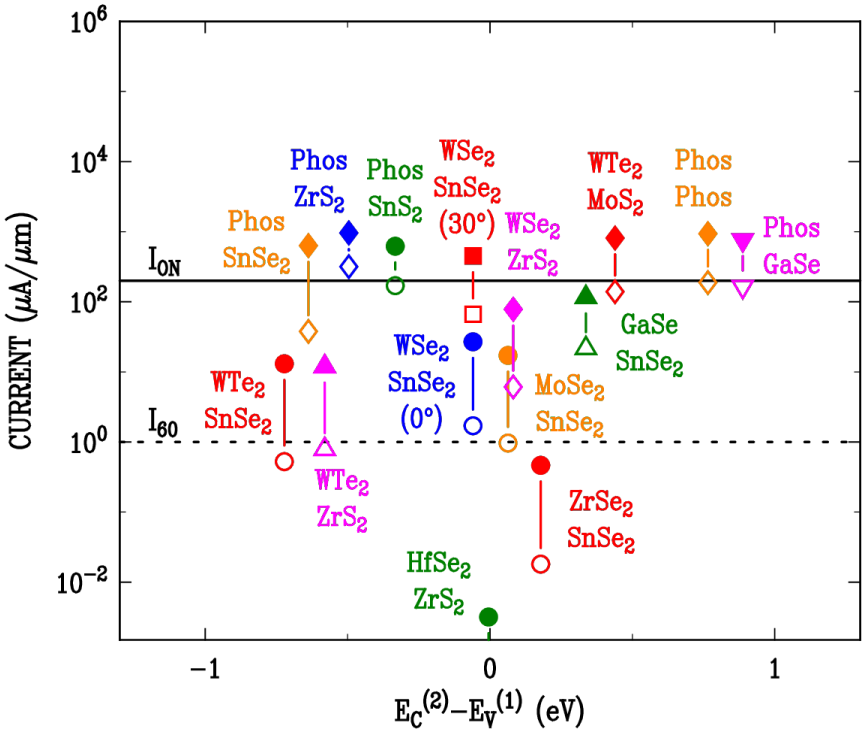

Figure 5.9 Tunneling current of Thin-TFETs with contact resistance

Same caption as for Figure 5.8, but now with contact resistance of 80 Ω•μm to both source and drain.

Thus far we have not included any contact resistance in the simulation. To investigate the effect of the contact resistance on tunneling currents, we add contact resistance of 80 Ω·μm to both source and drain based on the recommendation of the 2011 edition of the International Technology Roadmap for Semiconductors (ITRS) and its 2018 node.[155,31] Computations of the tunnel current then proceed iteratively, adjusting the voltage drop across the device based on the current from the prior iteration. The resulting I_{ON} and I_{60} are plotted in Figure 5.9. Compared with Figure 5.8, it is clear that the tunneling currents with larger magnitude are more affected by the contact resistance, since the maximum possible I_{ON} is now 1250 μA/μm = (0.2 V)/(160 Ω·μm). The ON currents for TFETs such as Phos-Phos, Phos-ZrS_2, and WTe_2-MoS_2 closely approach this limit. For the case of a Phos-Phos device with one layer of h-BN as the tunnel barrier, as discussed in the previous paragraph, we have estimated the ON current to be 1.9×10^3 μA/μm which is considerably greater than the limiting value of 1250 μA/μm. Hence we

expect the ON current of such a device to also exceed the desired value of 200 μA/μm even in presence of the contact resistance.

5.4.3 Discussion

Generally, Figure 5.7 predicts that Thin-TFETs using different 2D materials as electrodes produce I_{ON} and I_{60} values that vary across several orders of magnitude. In particular, devices using Phos as one or both electrodes have currents that are much larger than for devices using TMD as both of the electrodes. There are two reasons for this difference. First, as shown in Figure 5.5(c), the VB maximum of Phos is at the Γ-point. States at the Γ point experience a lower tunneling barrier in the vdW gap than do states with finite parallel wavevector $\mathbf{k}$, such as the K-point band-edge states in WSe_2.

To illustrate this dependence, let us consider tunneling between two electrodes of ML WSe_2, as shown in Figure 5.10. Figure 5.10(a) shows the potential (ionic plus Hartree plus exchange-correlation) for both 1 ML and 2 ML WSe_2. Within the Bardeen approximation we can consider the two electrodes independently, i.e. using the potential and wavefunctions for the 1ML case and taking the product of the tails of the wavefunctions for the two electrodes at the midpoint of the barrier that separates them. Hence, to understand the magnitude of the tunnel currents it suffices to examine the states of the individual ML electrodes, and in Figure 5.10(b) we show two states of ML WSe_2, one from the VB maximum at the K point of the BZ and the other from the highest lying VB band at the Γ point (energy of -0.44 eV relative to the VB maximum). These wavefunctions are evaluated at a general (*x,y*) point (i.e. without special symmetry) in the unit cell. As seen in Figure 5.10(b), the K-point state has a significantly faster decay in the vacuum than the Γ-point state, due to the nonzero lateral momentum, $|\mathbf{k}| = 1.289$ Å^{-1}, of the former state. In general, a state with energy *E* and nonzero value of $|\mathbf{k}|$ will have a decay constant in the vacuum given by $\kappa = \sqrt{2m(E_{VAC} - E)/\hbar^2 + |\mathbf{k}|^2}$, where E_{VAC} is the vacuum level and *m* is the free-electron mass.[156,157] Such states decay in the vacuum as if they experience an effective barrier that is *larger* than the nominal one by an amount $\hbar^2|\mathbf{k}|^2/2m$. For the lateral wavevector of 1.289 Å^{-1} we have $\hbar^2|\mathbf{k}|^2/2m = 6.33$ eV, a

substantial increase in the effective barrier, and indeed the decay constants deduced from the slopes of the wavefunction tails in Figure 5.10(b) are in good agreement with values obtained from this formula for κ. Thus, states with nonzero lateral momentum experience a much faster decay in the barrier (even for the case of only a van der Waals barrier), and hence the tunnel current that occurs between K-point states will be much less than that which occurs between Γ-point states.

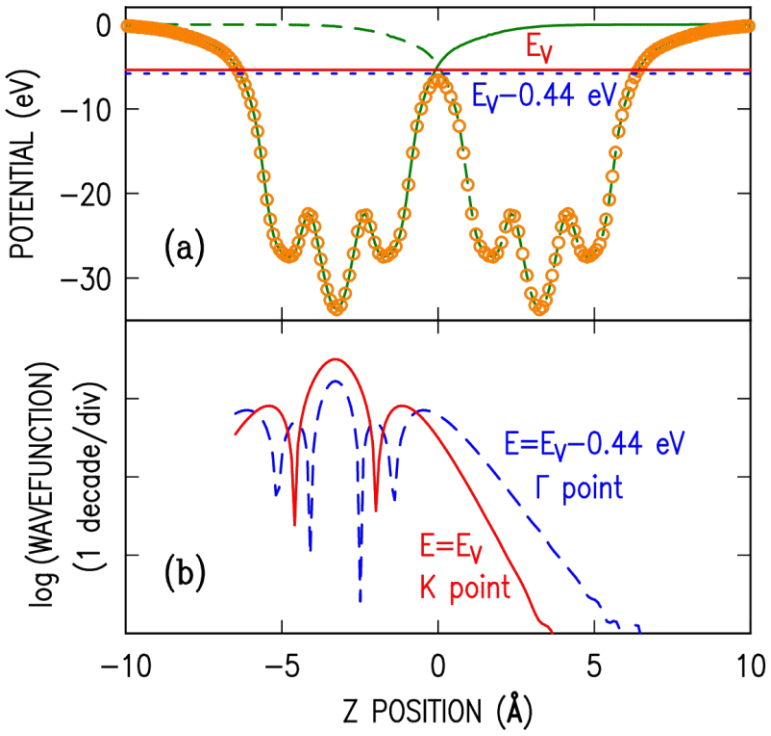

Figure 5.10 Potential and wavefunction of WSe_2

(a) Potential, averaged over (x,y), for 2 ML WSe_2 (orange circles) and 1 ML WSe_2 (solid and green dashed lines, for two separate MLs). The energy of the VB maximum is indicated, E_V (solid red horizontal line, at 5.38 eV below the vacuum level, which is at 0 eV on the plot), along with energy of a state at $E_V - 0.44$ eV (dashed blue horizontal line). (b) Wavefunctions for 1 ML WSe_2 for a K-point state at the VB maximum (solid red line) and a Γ-point state at $E_V - 0.44$ eV (dashed blue line).

The second effect that gives rise to the variation in tunnel current depending on the electrode material, as seen in Figure 5.8, has to do with the specific form of the wavefunction that occurs at zone-edge states, producing in certain cases orthogonality (in the overlap matrix element of Eq. (28)) between the states of the source and drain electrodes. This effect can be explained by reference to a two-band nearly free electron model, in which states of the two bands are mixed. According to this model, wavefunctions for states at the BZ edge are very different from those elsewhere in the BZ. An energy gap opens at the BZ edge, with states on either side of the gap having standing wave type wavefunctions of the form $f(z)\cos(\mathbf{k}\bullet\boldsymbol{\rho})$ and $g(z)\sin(\mathbf{k}\bullet\boldsymbol{\rho})$, respectively, where $f(z)$ and $g(z)$ are general functions describing the *z* part of the wavefunctions. Many TMD monolayers have their VB maximum and/or CB minimum at the K point, which is at the BZ edge. When we consider unlike-band tunneling and compute the overlap matrix element, then because of the orthogonality between the $\cos(\mathbf{k}\bullet\boldsymbol{\rho})$ and $\sin(\mathbf{k}\bullet\boldsymbol{\rho})$ parts of the wavefunctions (i.e. even with the two states being centered at different *z* values), we find in certain cases a result of zero.

Comparing our results with those of prior theories, we find that there are significant discrepancies between the various treatments. One of these arises from the use of a different form from Eq. (22) for evaluating the matrix element:[131,133]

$$M_{\alpha\beta} = \int d\mathbf{r}\, \psi_\alpha^* V(\mathbf{r}) \psi_\beta \,, \tag{29}$$

where $V(\mathbf{r})$ is a "scattering potential" of the tunnel barrier, and ψ_α , ψ_β are wavefunctions of the source and drain electrodes respectively as in Eq. (22). The integral is evaluated over the entire tunnel barrier volume. Equations (22) and (29) will, in general, yield quite different results. There is however some similarity between them, since both equations depend on the difference, **q**, between the lateral wavevectors for the states in the two electrodes. All authors dealing with 2D tunneling devices evaluate this part of Eqs. (3) or (10) in a similar way, yielding some sort of Gaussian or Lorentzian form that falls off for $|\mathbf{q}|$ values above some critical value (which is inversely proportional to the coherence length *L*). This is the "wavevector conserving" part of the overlap matrix

element, and there is general agreement on this part. However, aside from that wavevector-conserving part, the remainder of the matrix element depends on the detailed nature of the wavefunctions as well on the different forms of Eqs. (22) and (29). These portions of the matrix elements from Eq. (22) compared to (29) will, in general, yield quite different results.

For example, a recent report considering a Phos-Phos TFET with one layer of h-BN as the tunnel barrier has employed Eq. (29) for their current computations.[131] In Section III, we have estimated an ON current (with no contact resistance) for such a device to be 1.9×10^{3} μA/μm. This current is about an order of magnitude smaller than that in Ref. 131. We believe that this discrepancy arises from the use in that work of Eq. (29) for the tunneling matrix element (with the potential V taken to be the full potential of the h-BN barrier), whereas we have employed Eq. (22). We emphasize that we are in full agreement with nearly all of the results of Ref. 131, including their voltage-dependence of the current for both like-band and unlike-band tunneling. We have disagreement only on the issue of the absolute magnitude of the tunnel current. (We also note that Ref. 131 explicitly includes the h-BN barrier layer in the wavefunction evaluation, whereas we have only estimated the influence of the h-BN, but it seems unlikely that this difference will lead to a significant *increase* in the current).

Apart from the discrepancy resulting from which form to use for evaluating the tunneling matrix element, a second discrepancy arises from the use of wavefunctions that consist of a single plane-wave (SPW), rather than the full form as in Eq. (20). The SPW wavefunctions lead to a matrix element that, aside from the "wavevector conserving" part discussed above, is essentially independent of the particular states involved in the tunneling. As discussed above in connection with the two-band nearly free electron model, we find in the VASP wavefunctions a large dependence of the matrix elements on the particular states; for all states the magnitude of the matrix element is much different than that obtained from the SPW theory. Theories using essentially the SPW wavefunctions for TMD devices have been employed in several recent works,[126,127,138] employing a constant matrix element value of 0.02 eV (for $|\mathbf{q}| = 0$), obtained by matching to experiment employing an argument involving interlayer charge transfer time.[127] From

our DFT results, we find the value of the matrix element for the WSe_2-$SnSe_2$ (30 °) device to be 0.06 eV, i.e. 3× larger than that in Ref. 127. Our current (which is proportional to the square of the matrix element) is therefore about an order of magnitude larger, as shown in Figure 5.7(b). As revealed by our results of Figure 5.7, 5.8 and 5.9, the matrix element (and hence the tunnel current) is very dependent on what 2D materials being used for the Thin-TFETs.

Finally, we note that several computations using a theory other than the Bardeen formalism for interlayer TFETs have been reported.[146,147,148] In these works, detailed device simulations are performed using the non-equilibrium Green's function (NEGF) formalism. In Ref. 146, the authors consider a MoS_2-WTe_2 TFET with 1 nm thick h-BN as the tunnel barrier, with a coupling term between electrodes set by reference to experimental results for graphene/h-BN.[158] To compare with their results, we perform computations using their choice of parameters (V_{DS} = 0.3 V, overlap length of 20 nm, etc.), except with a vdW gap (zero layers of h-BN, corresponding to separation between chalcogen planes of opposing TMD electrodes of about 0.33 nm). We then roughly estimate the current with the h-BN included by dividing the result by 2500, corresponding to two layers of h-BN (0.66 nm) plus our vdW interlayer thickness of 0.33 nm. In this way, we obtain an ON current of 4.0 μA/μm for a coherence length of 5 nm or 10 nm, or of 5.4 μA/μm for the coherence length of 20 nm. These values are in good agreement with those reported in Ref. 146.

In both Refs. 147 and 148, the authors consider a Thin-TFET with only a vdW gap (i.e. no hBN). The first of these reports studies a $MoTe_2$-SnS_2 TFET and assumes equal and opposite voltages applied to the two gates. As a result, relatively low tunnel currents are obtained, since the overlap of their VB of $MoTe_2$ with the CB of SnS_2 is not maximized (in order to maximize the current at ON state, the overlap of the VB of one electrode with the CB of the other should be maximized subject to constraints by their Fermi levels, i.e. the overlap of tunneling bands should be made close to the difference between Fermi levels of the two electrodes). In Ref. 148, a MoS_2-WTe_2 TFET is considered and a better electrostatic arrangement was used (with one gate held at fixed potential and a varying voltage applied to the other, i.e. the same as what we employ in

the present study). Currents as high as 1000 μA/μm is obtained, for a gate voltage of $V_{TG} = -0.3$ V. We have applied our method to their arrangement ($V_{DS} = -0.3$ V, overlap length of 30 nm, EOT = 0.5 nm and $V_{BG} = 0.5$ V), and we find an ON current that is about 6× larger than their result. This difference might arise from the tight-binding approximation used in Ref. 148, or the Bardeen approximation of our work. However, since the electrostatics model used in Ref. 148 is considerably more sophisticated than our 1D model, we feel that further investigation of this aspect of the problem is warranted, in order to better compare the theories.

It is important to remark that the results presented here should be viewed as only approximate estimates of the tunnel currents. The Bardeen method is based on the first-order perturbation theory (hence only requiring knowledge of only the eigenstates of each electrode in the absence of the other), and as such it is a convenient method for obtaining estimates of the tunneling current. However, modifications to the band structure of total system due to interaction between the electrodes are ignored, which is expected to be quite a significant approximation for the case of zero layers of h-BN between the electrodes. Additionally, our computations do not include effects of h-BN interlayers, except for graphene/h-BN/graphene devices where we have included the h-BN.[8] We find in that case the presence of the h-BN (aligned with the graphene) produces about a 50× reduction in the current for each layer of h-BN. However, misalignment of the h-BN and graphene could well produce additional reductions in the current. Similarly, for electrode materials other than graphene, it is possible that reductions to the current (beyond 50× per layer) due to lattice mismatch between the h-BN and the electrodes could well occur.

5.4.4 Conclusions

The goal of our work is to provide reliable estimates of the magnitude of the tunneling current in Thin-TFETs, which can be benchmarked against values that are appropriate for low-power digital applications. We find a considerable spread in the results depending on the materials used for the electrodes (due to the overlap matrix elements, i.e. considering effects that go beyond those due to wavevector conservation alone). As such, we feel that this work will be useful in choosing among the various materials with which to fabricate Thin-TFETs. The considerations described here regarding the detailed form of the

wavefunctions, i.e. their symmetry and momentum-dependent decay constant, would also apply to TFETs made from three-dimensional (3D) materials.[29] However, the Thin-TFETs have the potential advantage that the tunneling can occur across a thin insulating layer (e.g. an h-BN layer, or in principle just a vdW gap), as opposed to the tunneling across the bandgap of a semiconductor depletion layer that is generally utilized in a 3D TFET. This depletion layer requires substantial doping and/or electrostatic gating, such that the distance across it is sufficiently small to enable large current. For the Thin-TFETS considered here, the predicted ON currents are found to be relatively large, resulting from the very thin tunnel barrier (i.e. the vdW gap) that is assumed in the simulations.

5.4.5 Appendix

In the main body of this work we consider interlayer tunneling between two 2D electrodes, i.e. with electrodes extending in the (*x*,*y*) directions and tunneling in the *z* direction through a barrier. An exact solution for this problem using DFT wavefunctions does not exist, and we have employed the Bardeen method to solve this problem. In order to gain some insight into the accuracy of the Bardeen method, we considered a model problem in one dimension (1D), for which both the exact and the Bardeen solutions are readily available.

Our model problem is constructed by employing the plane-averaged potential for WSe_2 (as shown in Figure 5.10), using the 2-ML potential for our "exact solution" and the 1-ML potentials of two opposing electrodes for the "Bardeen solution". For both situations we truncate the potentials such that they are a constant within the electrodes; specifically, we take the value of the potential at its local minimum that occurs near the Se atoms, and use that for all locations deeper into the electrode. The resulting model potentials are shown in Figure 5.11. By taking the potentials to be a constant within the electrodes, we are able to easily obtain both the exact and the Bardeen solutions. (For ease of language we are referring to the locations where the potential is a constant as the "electrode" and elsewhere as the "barrier", although in reality no such division between these two regions is made in our solutions since we employ a completely general solution of the Schrödinger equation in 1D). We consider electrodes of thickness *D* for both

problems, as indicated in Figure 5.11. We solve the problem for a general *D* value, and then consider small *D* values of 3 – 5 Å, as applicable to actual ML TMD or phosphorene electrodes.

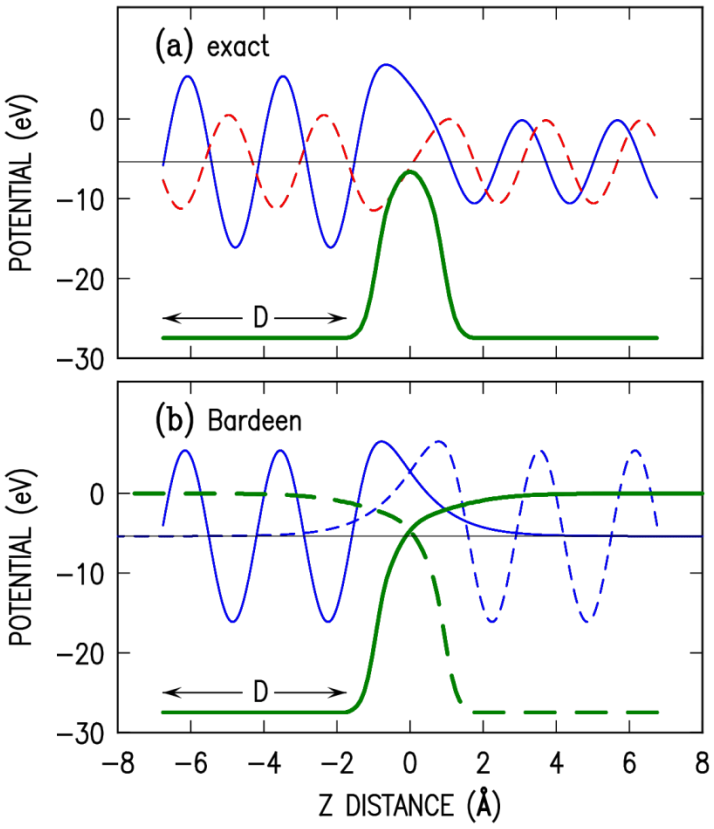

Figure 5.11 Model potentials to investigate accuracy of Bardeen method

Model potentials (thick green solid and dashed lines) for two one-dimensional problems that are solved in order to investigate the accuracy of the Bardeen method. Wavefunctions (solid blue and dashed red lines) are shown for a state with energy 5.38 eV below the vacuum level (shown at 0 eV in the plots). (a) Potential from 2-ML WSe_2, truncated in the electrodes. The wavefunction is shown, with real part as solid blue line and imaginary part as dashed red line. (b) Potential from 1-ML WSe_2, truncated in the electrodes and shown for two separate electrodes on the left- and right-hand sides. Wavefunctions (purely real) for each electrode are shown.

First we consider the exact solution to this one-dimensional problem. For a state with some energy *E* relative to the potential within the electrode, starting with an

outgoing plane wave in the right-hand electrode of the form Ce^{ikz} with $k = \sqrt{2mE/\hbar^2}$, we integrate Schrödinger's equation back through the barrier region and into the left-hand electrode.[159] We then normalize the wavefunction over the entire space of the two electrodes plus the barrier, and hence we determine $|C|^2$. The tunneling current associated with this state is then given by $j_z^{\text{exact}} = \hbar e k |C|^2 / m$.

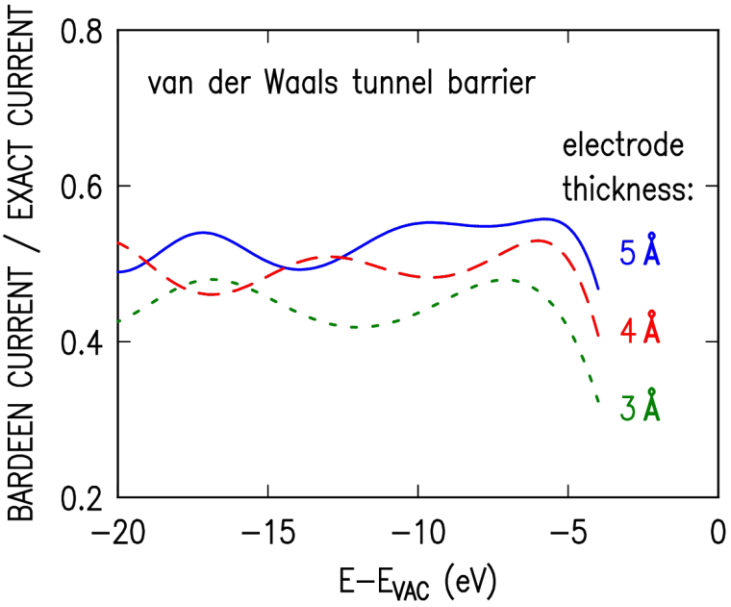

Figure 5.12 Ratio of Bardeen solution to exact solution

Ratio of tunnel current from a Bardeen solution to that from an exact solution, for the model potentials shown in Figure 5.11, as a function of the energy of the one-dimensional state relative to the vacuum level. Results are shown for three electrode thicknesses, *D*.

Now we turn to a Bardeen solution for the problem, employing two electrodes each with potential obtained from the truncated 1-ML WSe_2 potentials. For a state of energy E in each electrode, starting with a decaying exponential in the vacuum region with decay constant $\kappa = \sqrt{2m(E_{VAC} - E)/\hbar^2}$ for each electrode, the full wavefunctions are obtained by integrating Schrödinger's equation back through the barrier and into the

electrode, and normalizing. The current for this state in one electrode is obtained by summing over a continuum of free-electron type states in the opposing electrode,

$$\begin{aligned} j_z^{\text{Bardeen}} &= \frac{2\pi e}{\hbar}\sum_{k_j}|M|^2\,\delta(E-E_j) \\ &= \frac{2\pi e}{\hbar}\frac{D}{2\pi}\int dE_j\,\frac{\sqrt{2m}}{\hbar\sqrt{E_j}}|M|^2\,\delta(E-E_j) \\ &= \frac{2meD}{\hbar^3 k}|M|^2 \end{aligned} \tag{30}$$

with

$$M = \frac{\hbar^2}{2m}\left(\psi^*\frac{d\psi'}{dz} - \frac{d\psi^*}{dz}\psi'\right) \tag{31}$$

where ψ denotes the wavefunction from one electrode and ψ' is the wavefunction from the other, and the matrix-element M is evaluated at the midpoint of the barrier. In the second line of Eq. (30) we have inserted into the integrand the density-of-states for the continuum of free-electron type states, having wavevectors k_j and energies E_j.

Figure 5.12 shows the ratio of the Bardeen to the exact solution, as a function of the energy of the state and for electrode thickness values of 3 – 5 Å. This thickness enters both the exact and the Bardeen solutions through the normalization of the wavefunctions. We emphasize that we have not applied any specific boundary conditions on the far left of the left-hand electrode nor the far right of the right-hand one. Rather, our goal here is simply to compare the Bardeen to exact solutions as they pertain to the relatively small tunneling barriers that occur between the WSe_2 layers, i.e. arising from the potential within the van der Waals gap separating the electrodes. We find that for *D* values of 3 – 5 Å, the current obtained from Bardeen solution is typically a factor of 2 – 3 times *smaller* than that from the exact current. The energies displayed in Figure 5.12 cover the full range of values applicable to computations in the main body of this work: These energies within our one-dimensional model correspond to the *perpendicular component* of the energy, $E_\perp \equiv E_{3D} - \hbar^2|\mathbf{k}|^2/2m$, for an energy E_{3D} of a state in a three-dimensional computation. Typical VB edges for the TMD materials lie at about -5 eV below the

vacuum level, which for tunneling from Γ-point states then have the same values for $E_\perp$. However, for tunneling through a zone-edge (e.g. K-point state), we have $E_\perp \approx E_{3D} - 6\,\text{eV}$, as discussed above in connection with Figure 5.10. For CB edge states at the Γ-point, they will lie as high as about $-4\,\text{eV}$ below the vacuum level, i.e. at the upper end of the plotted curves of Figure 5.12, and zone-edge CB states will lie about 6 eV below that. Certain special states can lie even lower on this energy scale, e.g. if the amplitude of their Fourier component within the first BZ is zero, so that their **k** value to be used in computing $E_\perp$ lies outside the first BZ (such states then decay correspondingly faster in the vacuum).

6 Conclusions

In this work, centering on the idea of employing epitaxial 2D materials for scalable device fabrication over large areas, we studied growth, characterization, and simulation of some representative 2D materials. Specifically, we studied the surface structure of graphene formation on C-face of SiC, both experimentally and theoretically. In experiment, we investigated the sample surface phase as a function of annealing temperature and disilane pressure. LEED and STEM measurements were performed to study the sample surfaces. In theory, we carried out first-principles computations for an extensive set of surface structures and looked at surface energies as a function of C chemical potential and H chemical potential. Through these studies, we determine that with zero or low hydrogen coverage, the lowest energy surface/interface structures in C-rich conditions contain > 1 monolayer of Si, forming adatom-on-adlayer structures. We also conclude that the observed $\sqrt{43}\times\sqrt{43}$-R7.6° LEED pattern arises from the arrangement of Si adatoms on the adlayer, whereas the $\pm$7° LEED streaks of graphene likely arise from a low-strain fit between 6×6 SiC and $\sqrt{57}\times\sqrt{57}$-R6.5° unit cell of graphene.

We also studied band alignment and charge transfer in grown 2D heterostructures such as WSe_2–graphene and MoS_2–graphene using LEEM. The reflectivity spectra obtained from LEEM measurements allows extraction of work function differences between different domains on the sample surface and hence determination of band alignment and Schottky barrier at the interface of the heterostructures. In this way, the nature of electrical contact at the interface is revealed; the results are found to agree with those obtained from transport measurements.

Finally, we developed a DFT-Bardeen method to compute current-voltage characteristics of interlayer tunnel field effect transistors (interlayer TFETs). 2D materials are employed as the drain and source of this vertical tunneling device.

Compared with a previous method that employs a single plane wave in the Bardeen formalism, the DFT-Bardeen uses the full wavefunction computed from first-principles. This method was shown to take into account effects that are beyond simple lateral-momentum-conservation, including the detailed symmetry and form of the wavefunctions. Our recent work of a comprehensive comparison between our theoretical results using the DFT-Bardeen method and the experimental results by the Manchester group demonstrates that the current magnitude obtained by the DFT-Bardeen is reliable. This is important because, as mentioned in the Introduction of this thesis, one major challenge of using TFETs for mainstream applications is to achieve sufficiently high ON current. Hence, only a reliable estimate of the current magnitude can provide useful instructions regarding what 2D materials to choose from to make the TFETs. In this work, we have computed the current characteristics for interlayer TFETs using a variety of 2D materials as the source and drain electrodes and find a considerable spread in the resulting currents depending on the 2D materials being used. As such, we feel that the work will be useful in choosing appropriate 2D materials with which to fabricate interlayer TFETs.

References

[1] K. S. Novoselov, A. K. Geim, S. V. Morozov, D. Jiang, Y. Zhang, S. V. Dubonos, I. V. Grigorieva, and A. A. Firsov, *Science* **306**, 666 (2004).

[2] R. Peierls, *Ann. Inst. Henri Poincaré* **5**, 177 (1935).

[3] L. D. Landau, *Phys. Z. Sowjet.* **11**, 26 (1937).

[4] N. D. Mermin, *Phys. Rev.* **176**, 250 (1968).

[5] A. K. Geim and I. V. Grigorieva, *Nature* **499**, 419 (2013).

[6] J. Li, Y. Nie, K. Cho, and R. M. Feenstra, *J. Electron. Mater.* 46, 1378 (2017).

[7] J. Li, G. He, M. Widom, L. Nemec, Q. Wang, P. Rinke, M. Scheffler, V. Blum, M. J. Kim, and R. M. Feenstra. To be published.

[8] R. M. Feenstra, S. C. de la Barrera, J. Li, Y. Nie, K. Cho, submitted to *J. Phys. Condens. Matter* (Accepted).

[9] K. Zhang, B. Jariwala, J. Li, N. C. Briggs, B. Wang, D. Ruzmetov, R. A. Burke, J. O. Lerach, T. G. Ivanov, M. Hague, R. M. Feenstra, and J. A. Robinson, *Nanoscale* **10**, 336 (2018).

[10] S. Subramanian, D. D. Deng, K. Xu, N. Simonson, K. Wang, K. Zhang, J. Li, R. M. Feenstra, S. K. Fullerton, J. A. Robinson, *Carbon* **125**, 551 (2017).

[11] Y.-C. Lin, J. Li, S. C. de la Barrera, S. M. Eichfeld, Y. Nie, R. Addou, P. C. Mende, R. M. Wallace, K. Cho, R. M. Feenstra, and J. A. Robinson, *Nanoscale*, **8**, 8947 (2016).

[12] D. P. Gopalan, P. C. Mende, S. C. de la Barrera, S. Dhingra, J. Li, K. Zhang, N. A. Simonson, J. A. Robinson, N. Lu, Q. Wang, M. J. Kim, B. D'Urso, and R. M. Feenstra, *J. Mater. Res.* **31**, 945 (2016).

[13] P. C. Mende, J. Li, and R. M. Feenstra. To be published.

[14] P. R. Wallace, *Phys. Rev.* **71**, 622 (1947).

[15] A. H. Castro Neto, F. Guinea, N. M. R. Peres, K. S. Novoselov, and A. K. Geim, *Rev. Mod. Phys.* **81**, 109 (2009).

[16] W. Choi, and J.-W. Lee, *Graphene: Synthesis and Applications*. (CRC press, 2011).

[17] A. K. Geim and K. S. Novoselov, *Nat. Mater.* **6**, 183 (2007).

[18] J. Hass, W. A. de Heer, and E. H. Conrad, *J. Phys.: Condens. Matter* **20**, 323202 (2008).

[19] C. R. Dean, A. F. Young, I. Meric, C. Lee, L. Wang, S. Sorgenfrei, K. Watanabe, T. Taniguchi, P. Kim, K. L. Shepard, and J. Hone, *Nat. Nanotechnol.* **5**, 722 (2010).

[20] J. Xue, J. Sanchez-Yamagishi, D. Bulmash, P. Jacquod, A. Deshpande, K. Wantanabe, T. Taniguchi, P. Jarillo-Herrero, and B. J. LeRoy, *Nat. Mater.* **10**, 282 (2011).

[21] Q. H. Wang, K. Kalantar-Zadeh, A. Kis, J. N. Coleman, and M. S. Strano, *Nat. Nanotechnol.* **7**, 699 (2012).

[22] *Gmelin Handbook of Inorganic and Organometallic Chemistry*, 8th ed., Vol. B7. (Springer-Verlag, Berlin, 1995).

[23] C. Lee, H. Yan, L. E. Brus, T. F. Heinz, J. Hone, and S. Ryu, *ACS Nano*, **4**, 2695 (2010).

[24] A. Kuc, N. Zibouche, and T. Heine, *Phys. Rev. B* **83**, 245213 (2011).

[25] J.-P. Colinge, *Solid-State Electron.* **48**, 897 (2004).

[26] C. Auth *et al.*, *2012 Symposium on VLSI Technology (VLSIT)*, Honolulu, HI, pp. 131-132 (2012). doi: 10.1109/VLSIT.2012.6242496

[27] Y. Guo and J. Robertson, *Appl. Phys. Lett.* **108**, 233104 (2016).

[28] L. L. Chang and L. Esaki, *Appl. Phys. Lett.* **31**, 687 (1977).

[29] A. C. Seabaugh and Q. Zhang, *Proc. IEEE.* **98**, 2095 (2010).

[30] A. M. Ionescu and H. Riel, *Nature* **479**, 329 (2011).

[31] D. E. Nikonov and I. A. Young, *Proc. IEEE* **101**, 2498 (2013).

[32] G. Fiori, F. Bonaccorso, G. Iannaccone, T. Palacios, D. Neumaier, A. Seabaugh, S. K. Banerjee, and L. Colombo, *Nat. Nanotechnol.* **9**, 768 (2014).

[33] T. Roy, M. Tosun, X. Cao, H. Fang, D.-H. Lien, P. Zhao, Y.-Z. Chen, Y.-L. Chueh, J. Guo, and A. Javey, *ACS Nano* **9**, 2071 (2015).

[34] S. M. Sze, *Physics of Semiconductor Devices.* John Wiley (1969).

[35] M. S. Lundstrom, *International SOI Conference, 2006 IEEE*, pp. 1-3. IEEE (2006).

[36] G. DeMicheli, Y. Leblebici, M. Gijs, and J. Voros, *Nanosystems design and technology.* (Springer, 2009).

[37] C. Berger, Z. Song, T. Li, X. Li, A. Y. Ogbazghi, R. Feng, Z. Dai, A. N. Marchenkov, E. H. Conrad, P. N. First, and W. A. de Heer, *J. Phys. Chem. B* **108**, 19912 (2004).

[38] Y.-M. Lin, A. Valdes-Garcia, S.-J. Han, D. B. Fermer, I. Meric, Y. Sun, Y. Wu, C. Dimitrakopoulos, A. Grill, P. Avouris, and K. A. Jenkins, *Science* **332**, 1294 (2011).

[39] V. Ramachandran, M. F. Brady, A. R. Smith, R. M. Feenstra, and D. W. Greve, *J. Electron. Mater.* **27**, 308 (1998).

[40] K. Oura, M. Katayama, A. V. Zotov, V. G. Lifshits, and A. A. Saranin, *Surface science: an introduction.* (Springer-Verlag Berlin Heidelberg 2003).

[41] M. A. Van Hove, W. H. Weinberg, and C.-M. Chan, *Low-energy Electron Diffraction – Experiment, Theory and surface structure determination.* (Springer-Verlag, Berlin Heidelberg, 1986).

[42] Hans Lüth, *Solid Surfaces, Interfaces and Thin Films.* (Springer-Verlag, Berlin Heidelberg, 2001).

[43] G. He, N. Srivastava, and R. M. Feenstra, *J. Electron. Mater.* **43**, 819 (2014).

[44] V. Blum and K. Heinz, *Comput. Phys. Commun.* **134**, 392 (2001).

[45] J. B. Pendry, *J. Phys. C: Solid State Phys.* **13**, 937 (1980).

[46] P. J. Rous, J. B. Pendry, D. K. Saldin, K. Heinz, K. Müller, and N. Bickel, *Phys. Rev. Lett.* **57**, 2951 (1986).

[47] P. J. Rous, J. B. Pendry, *Surf. Sci.* **219**, 355 (1989).

[48] P. J. Rous, *Prog. Surf. Sci.* **39**, 3 (1992).

[49] S. C. de la Barrera, Y.-C. Lin, S. M. Eichfeld, J. A. Robinson, Q. Gao, M. Widom, and R. M. Feenstra, *J. Vac. Sci. Technol. B* **34**, 04J106 (2016).

[50] H. Hibino, H. Kageshima, F. Maeda, M. Nagase, Y. Kobayashi, and H. Yamaguchi, *Phys. Rev. B* **77**, 075413 (2008).

[51] R. M. Feenstra, N. Srivastava, Q. Gao, M. Widom, B. Diaconescu, T. Ohta, G. L. Kellogg, J. T. Robinson, and I. V. Vlassiouk, *Phys. Rev. B* **87**, 041406(R) (2013).

[52] E. Bauer, *Rep. Prog. Phys.* **57**, 895 (1994).

[53] W. Święch, B. Rausenberger, W. Engel, A. M. Bradshaw, and E. Zeitler, *Sur. Sci.* **294**, 297 (1993).

[54] L. Reimer: *Transmission Electron Microscopy, Springer Series in Optical Sciences,* 4th ed. Vol. **36**. (Springer, Berlin, 1997).

[55] S. C. de la Barrera, Doctoral Thesis, 2016.

[56] K. Emtsev, A. Bostwick, K. Horn, J. Jobst, G. L. Kellogg, L. Ley, J. L. McChesney, T. Ohta, S. A. Reshanov, J. Röhrl, E. Rotenberg, A. K. Schimid, D. Waldmann, H. B. Weber, and T. Seyller, *Nat. Mat.* **8**, 203 (2009).

[57] C. Riedl, C. Coletti, T. Iwasaki, A. A. Zakharov, and U. Starke, *Phys. Rev. Lett.* **103**, 246804 (2009).

[58] Luxmi, N. Srivastava, and R. M. Feenstra, *J. Vac. Sci. Technol. B* **28**, C5C1 (2010).

[59] J. D. Emery, B. Detlefs, H. J. Karmel, L. O. Nyakiti, D. K. Gaskill, M. C. Hersam, J. Zegenhagen, and M. J. Bedzy, *Phys. Rev. Lett.* **111**, 215501 (2013), and references therein.

[60] F. Varchon, R. Feng, J. Hass, X. Li, B. N. Nguyen, C. Naud, P. Mallet, J.-Y. Veuillen, C. Berger, E. H. Conrad, and L. Magaud, *Phys. Rev. Lett.* **99**, 126805 (2007).

[61] C. Riedl, U. Starke, J. Bernhardt, M. Franke, and K. Heinz, *Phys. Rev. B* **76**, 245406 (2007).

[62] K. V. Emtsev, F. Speck, Th. Seyller, L. Ley, and J. D. Riley, *Phys. Rev. B* **77**, 155303 (2008).

[63] S. Oida, F. R. McFeely, J. B. Hannon, R. M. Tromp, M. Copel, Z. Chen, Y. Sun, D. B. Farmer, and J. Yurkas, *Phys. Rev. B* **82**, 041411 (R) (2010).

[64] C. Virojanadara, S. Watcharinyanon, A. A. Zakharov, and L. I. Johansson, *Phys. Rev. B* **82**, 205402 (2010).

[65] F. Hiebel, P. Mallet, F. Varchon, L. Magaud, and J.-Y. Veuillen, *Phys. Rev. B* **78**, 153412 (2008).

[66] N. Srivastava, G. He, Luxmi, and R. M. Feenstra, *Phys. Rev. B* **85,** 041404(R) (2012).

[67] Luxmi, N. Srivastava, G. He, and R. M. Feenstra, *Phys. Rev. B* **82**, 235406 (2010).

[68] C. Virojanadara, M. Syväjarvi, R. Yakimova, L. I. Johansson, A. A. Zakharov, and T. Balasubramanian, *Phys. Rev. B* **78**, 245403 (2008).

[69] R. M. Tromp and J. B. Hannon, *Phys. Rev. Lett.* **102**, 106104 (2009).

[70] U. Starke, J. Schardt, J. Bernhardt, and K. Heinz, *J. Vac. Sci. Technol. A* **17**, 1688 (1999).

[71] W. A. de Heer, C. Berger, M. Ruan, M. Sprinkle, X. Li, Y. Hu, B. Zhang, J. Hankinson, and E. Conrad, *Proc. Natl. Acad. Sci.* **108**, 16900 (2011).

[72] N. Camara, B. Jouault, A. Caboni, B. Jabakhaniji, W. Desrat, E. Pausas, C. Consejo, N. Mestres, P. Godignon, and J. Camassel, *Appl. Phys. Lett.* **97**, 093107 (2010).

[73] C. Çelebi, C. Yanık, A. G. Demirkol, I. I. Kaya, *Carbon* **50**, 3026 (2012).

[74] C. Çelebi, C. Yanık, A. G. Demirkol, I. I. Kaya, *Appl. Surf. Sci.* **264**, 55 (2013).

[75] F. Varchon, P. Mallet, L. Magaud, and J.-Y. Veuillen, *Phys. Rev. B* **77**, 165415 (2008).

[76] N. Srivastava, G. He, Luxmi, P. C. Mende, R. M. Feenstra, and Y. Sun, *J. Phys. D: Appl. Phys.* **45**, 154001 (2012).

[77] A. R. Smith, V. Ramachandran, and R. M. Feenstra, *J. Vac. Sci. Technol. A* **16**, 1641 (1998).

[78] L. Nemec, V. Blum, P. Rinke, and M. Scheffler, *Phys. Rev. Lett.* **111**, 065502 (2013).

[79] Luxmi, S. Nie, P. J. Fisher, R. M. Feenstra, G. Gu, and Y. Sun, *J. Electron. Mater.* **38**, 718 (2009).

[80] G. Kresse and J.hafner, *Phys. Rev. B* **47**, RC558 (1993).

[81] G. Kresse and J. Furthmüller, *Phys. Rev. B* **54**, 11169 (1996).

[82] V. Blum, R. Gehrke, F. Hanke, P. Havu, V. Havu, X. Ren, K. Reuter, and M. Scheffler, *Comput. Phys. Commun.* **180**, 2175 (2009).

[83] V. Havu, V. Blum, P. Havu, and M. Scheffler, *J. Comput. Phys.* **228**, 8367 (2009).

[84] L. Nemec, F. Lazarevic, P. Rinke, M. Scheffler, and V. Blum, *Phys. Rev. B* **91,** 161408(R) (2015).

[85] A. Tkatchenko and M. Scheffler, *Phys. Rev. Lett.* **102**, 073005 (2009).

[86] J. P. Perdew, K. Burke, and M. Ernzerhof, *Phys. Rev. Lett.* **77**, 3865 (1996).

[87] J. Neugebauer and M. Scheffler, *Phys. Rev. B* **46**, 16067 (1992).

[88] K. Reuter and M. Scheffler, *Phys. Rev. B* **65**, 035406 (2002).

[89] A. J. Van Bommel, J. E. Crombeen, and A. Van Tooren, *Surf. Sci.* **48**, 463 (1975).

[90] U. Starke and C. Riedl, *J. Phys.: Condens. Matter* **21**, 134016 (2009).

[91] L. Vitali, M. G. Ramsey, and F. P. Netzer, *Phys. Rev. B* **63**, 165320 (2001).

[92] W. Norimatsu and M. Kusunoki, *J. Phys. D: Appl. Phys.* **47**, 094017 (2014).

[93] J. Kloppenburg, L. Nemec, B. Lange, M. Scheffler, and V. Blum. To be published.

[94] J. Bernhardt, M. Nerding, U. Starke, K. Heinz, *Mater. Sci. Eng.: B* **61**, 207 (1999).

[95] A. Seubert, J. Bernhardt, M. Nerding, U. Starke, and K. Heinz, *Surf. Sci.* **454**, 45 (2000).

[96] K. Heinz, J. Bernhardt, J. Schardt, and U. Starke, *J. Phys.: Condens. Matter* **16**, S1705 (2004).

[97] A. Taylor, and R. M. Jones in *Silicon Carbide - A High Temperature Semiconductor*, Eds. J. R. O'Connor, J. Smiltens (Pergamon Press, New York, 1960), p. 147.

[98] P. Trucano and R. Chen, *Nature* **258**, 136 (1975).

[99] E. Cadelano, P. L. Palla, S. Giordano, L. Colombo, *Phys. Rev. B* **82**, 235414 (2010).

[100] K. V. Zakharchenko, M. I. Katsnelson, and A. Fasolino, *Phys. Rev. Lett.* **102**, 046808 (2009).

[101] M. Pozzo, D. Alfè, P. Lacovig, P. Hofmann, S. Lizzit, and A. Baraldi, *Phys. Rev. Lett.* **106**, 135501 (2011).

[102] N. Camara, J.-R. Huntzinger, G. Rius, A. Tiberj, N. Mestres, F. Pérez-Murano, P. Godignon, and J. Camassel, *Phys. Rev. B* **80**, 125410 (2009).

[103] K. I. Bolotin, K. J. Sikes, Z. Jiang, M. Klima, G. Fudenberg, J. Hone, P. Kim, H. L. Stormer, *Solid State Commun.* **146**, 351 (2008).

[104] J. L. Tedesco, B. L. VanMil, R. L. Myers-Ward, J. M. McCrate, S. A. Kitt, P. M. Campbell, G. G. Jernigan, J. C. Culbertson, C. R. Eddy Jr., and D. K. Gaskill, *Appl. Phys. Lett.* **95**, 122102 (2009).

[105] E. Pallecchi, F. Lafont, V. Cavaliere, F. Schopfer, D. Mailly, W. Poirier and A. Ouerghi, *Sci. Rep.* **4**, 4558 (2014).

[106] F. Speck, J. Jobst, F. Fromm, M. Ostler, D. Waldmann, M. Hundhausen, H. B. Weber, and Th. Seyller, *Appl. Phys. Lett.* **99**, 122106 (2011).

[107] C. Riedl, C. Coletti and U. Starke, *J. Phys. D: Appl. Phys.* **43**, 374009 (2010).

[108] S. M. Eichfeld, L. Hossain, Y.-C. Lin, A. F. Piasecki, B. Kupp, A. G. Birdwell, R. A. Burke, N. Lu, X. Peng, J. Li, A. Azcatl, S. McDonnell, R. M. Wallace, M. J. Kim, T. S. Mayer, J. M. Redwing and J. A. Robinson, *ACS Nano* **9**, 2080 (2015).

[109] J. A. Robinson, M. Hollander, M. Labella, K. A. Trumbull, R. Cavalero, and D. W. Snyder, *Nano Lett.* **11**, 3875 (2011).

[110] A. Koma, *Thin Solid Films* **216**, 72 (1992).

[111] S. Vishwanath, X. Liu, S. Rouvimov, P. C. Mende, A. Azcatl, S. McDonnell, R. M. Wallace, R. M. Feenstra, J. K. Furdyna, D. Jena and H. Grace Xing, *2D Mater.* **2**, 024007 (2015).

[112] K. V. Emtsev, A. Bostwick, K. Horn, J. Jobst, G. L. Kellogg, L. Ley, J. L. McChesney, T. Ohta, S. A. Reshanov, J. Röhrl, E. Rotenberg, A. K. Schmid, D. Waldmann, H. B. Weber and T. Seyller, *Nat. Mater.* **8**, 203 (2009).

[113] T. Ohta, A. Bostwick, J. L. McChesney, T. Seyller, K. Horn and E. Rotenberg, *Phys. Rev. Lett.*, **98**, 206802 (2007).

[114] J. Ristein, S. Mammadov, and T. Seyller, *Phys. Rev. Lett.* **108**, 246104 (2012).

[115] S. Kopylov, A. Tzalenchuk, S. Kubatkin, and V. I. Fal'ko, *Appl. Phys. Lett.* **97**, 112109 (2010).

[116] S. Mammadov, J. Ristein, R. J. Koch, M. Ostler, C. Raidel, M. Wanke, R. Vasiliauskas, R. Yakimova, and T. Seyller, *2D Mater.* **1**, 035003 (2014).

[117] G. Kresse, and D. Joubert, *Phys. Rev. B* **59**, 1758 (1999).

[118] D. M. Ceperley and B. J. Alder, *Phys. Rev. Lett.* **45**, 566 (1980).

[119] M. J. Hollander, A. Agrawal, M. S. Bresnehan, M. LaBella, K. A. Trumbull, R. Cavalero, D. W. Snyder, S. Datta, and J. A. Robinson, *Phys. Status Solidi* **210**, 1062 (2013).

[120] Y.-J. Yu, Y. Zhao, S. Ryu, L. E. Brus, K. S. Kim, and P. Kim, *Nano Lett.* **9**, 3430 (2009).

[121] G.-B. Liu, W.-Y. Shan, Y. Yao, W. Yao, and D. Xiao, *Phys. Rev. B* **88**, 085433 (2013).

[122] E. McCann and M. Koshino, *Rep. Prog. Phys.***76**, 056503 (2013).

[123] Y. Liang, S. Huang, R. Soklaski, and L. Yang, *Appl. Phys. Lett.* **103**, 042106 (2013).

[124] K. He, N. Kumar, L. Zhao, Z. Wang, K. F. Mak, H. Zhao, and J. Shan, *Phys. Rev. Lett.* **113**, 026803 (2014).

[125] C. Zhang, Y. Chen, A. Johnson, M.-Y. Li, L.-J. Li, P. C. Mende, R. M. Feenstra, and C.-K. Shih, *Nano Lett.* **15**, 6494 (2015).

[126] M. Li, D. Esseni, G. Snider, D. Jena, and H. G. Xing, *J. Appl. Phys.* **115**, 074508 (2015).

[127] M. Li, D. Esseni, J. J. Nahas, D. Jena, and H. G. Xing, *J. Elec. Dev. Soc.* **3**, 200 (2015).

[128] D. Sarkar, X. Xie, W. Liu, W. Cao, J. Kang, Y. Gong, S. Kraemer, P. M. Ajayan, and K. Banerjee, *Nature* **526**, 91 (2015).

[129] Y.-C. Lin, R. K. Ghosh, R. Addou, N. Lu, S. M. Eichfeld, H. Zhu, M.-Y. Li, X. Peng, M. J. Kim, L.-J. Li, R. M. Wallace, S. Datta, and J. A. Robinson, *Nat. Comm.* **6**, 7311, (2015).

[130] R. Yan, S. Fathipour, Y. Han, B. Song, S. Xiao, M. Li, N. Ma, V. Protasenko, D. A. Muller, D. Jena, and H. G. Xing, *Nano Lett.* **15**, 5791 (2015).

[131] G. C. Constantinescu and N. D. M. Hine, *Nano Lett.* **16**, 2586 (2016).

[132] R. M. Feenstra, D. Jena, and G. Gu, *J. Appl. Phys.* **111**, 043711 (2012).

[133] L. Britnell, R. V. Gorbachev, A. K. Geim, L. A. Ponomarenko, A. Mishchenko, M. T. Greenaway, T. M. Fromhold, K. S. Novoselov, and L. Eaves, *Nat. Comm.* **4**, 1794 (2013).

[134] P. Zhao, R. M. Feenstra, G. Gu, and D. Jena, *IEEE Trans. Elec. Dev.* **60**, 951 (2013).

[135] S. C. de la Barrera, Q. Gao, and R. M. Feenstra, *J. Vac. Sci. Technol. B* **32**, 04E101 (2014).

[136] B. Fallahazad, K. Lee, S. Kang, J. Xue, S. Larentis, C. Corbet, K. Kim, H. C. Movva, T. Taniguchi, K. Watanabe, L. F. Register, S. K. Banerjee, and E. Tutuc, *Nano Lett.* **15**, 428 (2014).

[137] S. C. de la Barrera and R. M. Feenstra, *Appl. Phys. Lett.* **106**, 093115 (2015).

[138] P. M. Campbell, A. Tarasov, C. A. Joiner, W. J. Ready, and E. M. Vogel, *ACS Nano* **9**, 5000 (2015).

[139] J. Bardeen, *Phys. Rev. Lett.* **6**, 57 (1961).

[140] C. B. Duke, *Tunneling in Solids*, Solid State Physics, Suppl. 10 (New York: Academic, 1969).

[141] A. J. Bennett, C. B. Duke, and S. D. Silverstein, *Phys. Rev.* **176**, 969 (1968).

[142] J. P. Perdew, K. Burke and M. Ernzerhof, *Phys. Rev. Lett.* **27**, 3865 (1996).

[143] H. J. Monkhorst and J. D. Pack, *Phys. Rev. B* **13**, 5188 (1976).

[144] C. Gong, H. Zhang, W. Wang, L. Colombo, R. M. Wallace, and K. Cho, *Appl. Phys. Lett.* **103**, 053513 (2013).

[145] H. Liu, A. T. Neal, Z. Zhu, Z. Luo, X. Xu, D. Tománek, and P. D. Ye, *ACS Nano* **8**, 4033 (2014).

[146] J. Cao, M. Pala, A. Cresti, and D. Esseni, In "2015 Joint International EUROSOI Workshop and International Conference on Ultimate Integration on Silicon" (EUROSOI-ULIS), pp. 245-248, IEEE, 2015.

[147] Á. Szabó, S. J. Koester, and M. Luisier, *IEEE Electron Device Lett.* **36**, 514 (2015).

[148] F. Chen, H. Ilatikhameneh, Y. Tan, D. Valencia, G. Klimeck and R. Rahman, *arXiv preprint arXiv: 1608.05057* (2016).

[149] D. T. Do, S. D. Mahanti, and C. W. Lai, *Sci. Rep.* **5**:17044 (2015).

[150] V. Tran, R. Soklaski, Y. Liang, and L. Yang, *Phys. Rev. B* **89**, 235319 (2014).

[151] H. Lu and A. Seabaugh, *IEEE J. Electron Devices Soc.* **2**, 44 (2014).

[152] G. Fiori, F. Bonaccorso, G. Iannaccone, T. Palacios, D. Neumaier, A. Seabaugh, S. K. Banerjee, and L. Colombo, *Nat. Nanotechnol.* **9**, 768 (2014).

[153] R. Perricone, X. S. Hu, J. Nahas, and M. Niemier, In "2016 Design, Automation & Test in Europe Conference & Exhibition" (DATE), pp. 13-18, IEEE, 2016.

[154] L. Britnell, R. V. Gorbachev, R. Jalil, B. D. Belle, F. Schedin, M. I. Katsnelson, L. Eaves, S. V. Morozov, A. S. Mayorov, N. M. Peres, A. H. Castro Neto, J. Leist, A. K. Geim, L. A. Ponomarenko, and K. S. Novoselov, *Nano Lett.* **12**, 1707 (2012).

[155] (2011) International Technology Roadmap for Semiconductors. [Online]. Available: http://www.itrs.net/

[156] J. A. Stroscio, R. M. Feenstra, and A. P. Fein, *Phys. Rev. Lett.* **57**, 2579 (1986).

[157] J. Tersoff and D. R. Hamann, *Phys. Rev. B* **31**, 805 (1985).

[158] L. Britnell, R. V. Gorbachev, R. Jalil, B. D. Belle, F. Schedin, A. Mishchenko, T. Georgiou, M. I. Katsnelson, L. Eaves, S. V. Morozov, N. M. Peres, J. Leist, A. K. Geim, K. S. Novoselov, and L. A. Ponomarenko, *Science* **335**, 947 (2012).

[159] R. M. Feenstra, Y. Dong, M. P. Semtsiv, and W. T. Masselink, *Nanotechnology* **18**, 044015 (2007).